

AFGL-TR-88-0075

High-Voltage Charging of Spacecraft in
Low Polar Orbit: A Study of Physical Effects
Involved

J. G. Laframboise
J. Luo
L. W. Parker

AD-A213 809

York University
4700 Keele Street
North York, Ontario
CANADA

4 April 1988

Final Report
15 July 1983-14 July 1986

APPROVED FOR PUBLIC RELEASE; DISTRIBUTION UNLIMITED

AIR FORCE GEOPHYSICS LABORATORY
AIR FORCE SYSTEMS COMMAND
UNITED STATES AIR FORCE
HANSCOM AIR FORCE BASE, MASSACHUSETTS 01731-5000

DTIC
ELECTE
OCT 30 1989
S E D

"This technical report has been reviewed and is approved for publication"

Allen G. Rubin

(Signature)

ALLEN G. RUBIN
Contract Manager

David A. Hardy

(Signature)

DAVID A. HARDY
Branch Chief

FOR THE COMMANDER

Rita C. Sagalyn
(Signature)

RITA C. SAGALYN
Division Director

This report has been reviewed by the ESD Public Affairs Office (PA) and is releasable to the National Technical Information Service (NTIS).

Qualified requesters may obtain additional copies from the Defence Technical Information Center. All others should apply to the National Technical Information Service.

If your address has changed, or if you no longer wish to be removed from the mailing list, or if the addressee is no longer employed by your organization, please notify GL/IMAC, Hanscom AFB, MA 10731. This will assist us in maintaining a current mailing list.

Do not return copies of this report unless contractual obligations or notices on a specific document requires that it be returned.

Unclassified

SECURITY CLASSIFICATION OF THIS PAGE

REPORT DOCUMENTATION PAGE

1a. REPORT SECURITY CLASSIFICATION Unclassified			1b. RESTRICTIVE MARKINGS		
2a. SECURITY CLASSIFICATION AUTHORITY			3. DISTRIBUTION/AVAILABILITY OF REPORT Approved for public release; Distribution unlimited.		
2b. DECLASSIFICATION/DOWNGRADING SCHEDULE					
4. PERFORMING ORGANIZATION REPORT NUMBER(S)			5. MONITORING ORGANIZATION REPORT NUMBER(S) AFGL-TR-88-0075		
6a. NAME OF PERFORMING ORGANIZATION York University		6b. OFFICE SYMBOL (If applicable)		7a. NAME OF MONITORING ORGANIZATION Air Force Geophysics Laboratory	
6c. ADDRESS (City, State and ZIP Code) 4700 Keele Street North York, Ontario, Canada M3J 1P3				7b. ADDRESS (City, State and ZIP Code) Hanscom AFB Massachusetts 01731	
8a. NAME OF FUNDING/SPONSORING ORGANIZATION Air Force Geophysics Laboratory		8b. OFFICE SYMBOL (If applicable)		9. PROCUREMENT INSTRUMENT IDENTIFICATION NUMBER F19628-83-K-0028	
8c. ADDRESS (City, State and ZIP Code) Hanscom AFB Massachusetts 01731		10. SOURCE OF FUNDING NOS			
		PROGRAM ELEMENT NO. 62101F		PROJECT NO. 7661	TASK NO. 11
				WORK UNIT NO. AC	
11. TITLE (Include Security Classification) High-Voltage Charging of Spacecraft in Low Polar Orbit: A Study of Physical Effects Involved					
12. PERSONAL AUTHOR(S) J.G. Laframboise, J. Luo*, and L.W. Parker**					
13a. TYPE OF REPORT Final		13b. TIME COVERED FROM 15/07/83 TO 14/07/86		14. DATE OF REPORT (Yr., Mo., Day) 1988 April 4	
15. PAGE COUNT 148					
16. SUPPLEMENTARY NOTATION * Present address: Physics Department, University of Rhode Island, Kingston, Rhode Island 02881 ** Lee W. Parker, Inc., 252 Lexington Road, Concord, Massachusetts 01742					
17. COSATI CODES			18. SUBJECT TERMS (Continue on reverse if necessary and identify by block number)		
FIELD	GROUP	SUB GR	Spacecraft charging Low Polar Orbit		
			Auroral Ionosphere Electron Escape		
			Wake-Induced-Barrier Effect Computer Codes		
19. ABSTRACT (Continue on reverse if necessary and identify by block number) The work presented here is in six Sections. In the first, we review the main differences between the plasma environments in geostationary orbit and low polar orbit with regard to high-voltage charging situations. In Section 2, we develop a simple rough estimate of the required conditions for overall charging of a large spacecraft in low-orbit auroral-zone conditions. The results indicate that for any given spacecraft, surface potentials are likely to depend more strongly on the ratio of ambient flux of high-energy electrons to that of all ions than on any other environmental parameter, and this prediction has been corroborated by results of Gussenhoven et al for the DMSP satellites. In Section 3, we present results from a calculation of escape currents of electrons emitted from negatively-charged spacecraft surfaces having various orientations relative to the direction of the local magnetic field B. The suppression of such currents by B effects indicates that on mostly-dielectric large spacecraft such as the Shuttle Orbiter, local charging, (continued on reverse side)					
20. DISTRIBUTION/AVAILABILITY OF ABSTRACT UNCLASSIFIED/UNLIMITED <input checked="" type="checkbox"/> SAME AS RPT <input type="checkbox"/> DTIC USERS <input type="checkbox"/>			21. ABSTRACT SECURITY CLASSIFICATION Unclassified		
22a. NAME OF RESPONSIBLE INDIVIDUAL A.G. Rubin			22b. TELEPHONE NUMBER (Include Area Code) 617-377-2933		22c. OFFICE SYMBOL AFGL/PHK

19. ABSTRACT (continued):

especially on surfaces nearly parallel to **B**, may occur in ionospheric conditions which do not produce overall charging. This extends, to lower equivalent temperatures, the range of auroral-electron plasma conditions in which one can expect such a spacecraft to undergo high-voltage charging. We also investigate surface currents of nonescaping emitted electrons. In Section 4, we propose a wake-induced-barrier-effect mechanism which also suppresses escape of emitted electrons. This effect appears to permit beam-induced as well as polar-orbit high-voltage charging to occur. In Section 5, we present preliminary results of numerical simulation work directed toward making detailed tests of the predictions made in Sections 2-4. Section 6 contains some concluding remarks.

Accession For	
NTIS GRA&I	<input checked="" type="checkbox"/>
DTIC TAB	<input type="checkbox"/>
Unannounced	<input type="checkbox"/>
Justification	<input type="checkbox"/>
By	
Distribution/	
Availability Codes	
Dist. Special	
A-1	



TABLE OF CONTENTS

	Page
Acknowledgments	v
Abstract	vi
1. Introduction to the auroral-zone charging problem	1
2. Estimate of required environmental conditions for low-polar-orbit charging.	7
3. Calculation of escape currents of electrons emitted from negatively-charged spacecraft surfaces in a magnetic field.	16
3.1 Introduction to the escape-current problem	16
3.2 Theory for electric field normal to surface	20
3.3 Results and discussion for electric field normal to surface	26
3.4 Theory for non-normal electric-field directions	29
3.5 Results and discussion for non-normal electric-field directions	32
3.6 Calculation of escaping-electron densities	36
4. High-voltage charging of a dielectric-covered spacecraft: A wake-induced-barrier-effect mechanism.	38
4.1 Introduction to the wake-induced-barrier-effect problem	38
4.2 Description of the wake-induced-barrier-effect mechanism	40
4.3 Surface-potential calculation	46
4.4 Applications to low polar-orbit spacecraft charging; discussion	59
4.5 Applications to beam-induced Shuttle Orbiter charging; discussion	68

TABLE OF CONTENTS (continued)

	Page
5. Preliminary results from a numerical low-polar-orbit charging simulation.	75
6. Conclusions	81
References	89
Tables	100
Figures	100
** Appendix A: Listing of Program SCAPE for calculation of electron escape currents as described in Section 3.2	A1
** Appendix B: Listing of program WAKPO for calculating potential distribution across wake of dielectric spacecraft, as given by Eq. (4.13)	B1
Appendix C: Details of model calculation of downstream-point ion density described in Section 4.3	C1
** Appendix D: Listing of program IODEN for performing model calculation of downstream-point ion density as described in Section 4.3 and Appendix C	D1

** Appendices A, B and D will be published separately.

ACKNOWLEDGMENTS

We are grateful to W.J. Burke, M.S. Gussenhoven, L. Sonmor, and W.W.L. Taylor for valuable discussions and comments. One of us (J.G. Laframboise) wishes to acknowledge the contributions of co-authors to specific Sections of this Report, as follows: J. Luo (Sec. 4) and L.W. Parker (Sec. 5). We are indebted to L. Sonmor and S. Kerr for the use of their Runge-Kutta-Nystrom subroutine DIRKN; see Appendices B and D. We wish to thank the computer center of Air Force Geophysics Laboratory for the provision of computer time.

This work was supported by Air Force Geophysics Laboratory under contract number F19628-83-K-0028.

ABSTRACT

The work presented here is in six Sections. In the first, we review the main differences between the plasma environments in geostationary orbit and low polar orbit with regard to high-voltage charging situations. In Section 2, we develop a simple rough estimate of the required conditions for overall charging of a large spacecraft in low-orbit auroral-zone conditions. The results indicate that for any given spacecraft, surface potentials are likely to depend more strongly on the ratio of ambient flux of high-energy electrons to that of all ions than on any other environmental parameter, and this prediction has been corroborated by results of Gussenhoven et al for the DMSP satellites. In Section 3, we present results from a calculation of escape currents of electrons emitted from negatively-charged spacecraft surfaces having various orientations relative to the direction of the local magnetic field \mathbf{B} . The suppression of such currents by \mathbf{B} effects indicates that on mostly-dielectric large spacecraft such as the Shuttle Orbiter, local charging, especially on surfaces nearly parallel to \mathbf{B} , may occur in ionospheric conditions which do not produce overall charging. This extends, to lower equivalent temperatures, the range of auroral-electron plasma conditions in which one can expect such a spacecraft to undergo high-voltage charging. We also investigate surface currents of nonescaping emitted electrons. In Section 4, we propose a wake-induced-barrier-effect mechanism which also suppresses escape of emitted electrons. This effect appears to permit beam-induced as well as polar-orbit high-voltage charging to occur. In Section 5, we present preliminary results of numerical simulation work directed toward making detailed tests of the predictions made in Sections 2-4. Section 6 contains some concluding remarks.

1. INTRODUCTION TO THE AURORAL-ZONE CHARGING PROBLEM

The prediction of high-voltage charging or other environmental effects on a spacecraft in low Earth orbit is more difficult than in geosynchronous orbit, for at least three reasons: (a) space charge effects (on sheath and wake potentials) are more important, because space-charge densities are much higher (the Debye length is no longer \gg typical spacecraft dimensions) (b) ion flow effects are more important, because spacecraft orbital speed \gtrsim ion thermal speeds (c) the geomagnetic field \mathbf{B} is likely to have an important influence on charged-particle motions because \mathbf{B} is now much larger, and not all of the average particle gyroradii of importance are any longer \gg typical spacecraft dimensions. In the case of the Shuttle Orbiter, other complications arise. The most important one is that its surface is almost entirely dielectric rather than conductive. The possibility therefore exists that local charging may occur on the Orbiter, especially on its downstream-facing surfaces, in ionospheric conditions which do not produce overall charging. Another complication for the Orbiter is that charged-particle mean free paths may not always be much larger than spacecraft size, especially during thruster firings and water dumps. A further complication arises from evidence that spontaneous oscillations occur in some parts of the

Orbiter's ionized wake. Although there is no evidence that these can substantially affect the likelihood of high-voltage charging, this issue is largely unexplored. Another complicating factor is the geometrical complexity of the Orbiter's cargo bay area. When this study was begun, polar orbit Shuttle flights appeared to be imminent, and its primary motivation was the need to gain an understanding of all important effects governing the possibility of high-voltage charging on the Orbiter's external surfaces.

Table 1 summarizes some important characteristic lengths and speeds for low-orbit conditions. A surprising feature of this Table is that the sheath thicknesses indicated are much larger than the ambient Debye length, but this is because the sheath potentials are much larger than the ambient-particle thermal energies. These distances are at most comparable to typical spacecraft dimensions, in contrast with the geosynchronous situation. Table 1 also shows that secondary electrons have an average gyroradius \ll typical spacecraft dimensions, so their escape will be inhibited strongly on surfaces which are nearly parallel to the magnetic field \mathbf{B} (Fig. 3.1), while auroral electrons have an average gyroradius \gtrsim typical spacecraft dimensions, so their collection will be affected only moderately, except for very large spacecraft. We return to this question in Section 3. Also evident from Table 1 is the large value of the ion

speed ratio (spacecraft speed/ion most-probable thermal speed) in low-orbit conditions. In these conditions, ion collection on downstream surfaces will be inhibited. If a surface is simultaneously downstream and nearly parallel to the magnetic field, as is likely to be the case in the auroral zones, then the tendency for high-voltage charging to occur on it will be greatly increased (Fig. 3.2).

High-voltage charging of large spacecraft by the low-polar-orbit plasma environment was first predicted by Parks and Katz (1981). The first observation of such charging was made by Gussenhoven et al (1985) using the DMSP 6 and 7 satellites. Their observations indicate that high-voltage charging (conventionally defined as involving spacecraft surface potentials at least 100 volts different from that of the surrounding plasma) will be environmentally produced only when a spacecraft encounters an "auroral" electron plasma which imposes on it a sufficiently large ratio of "hot" electron ambient flux to total ion (ambient or ram) flux (see their Fig. 7 and associated discussion). This corroborates a prediction, made by Laframboise (1985b), that for any given spacecraft, surface potentials are likely to depend more strongly on the ratio of ambient flux of high-energy electrons to that of all ions, than on any other environmental parameter; see also Laframboise and Parker (1986,1987). Section 2 of this Report contains a derivation of this prediction. The theoretical prediction of Parks and Katz (1981), Katz and Parks (1983), indicates that such charging is more likely

for larger spacecraft because electron collection increases more rapidly with spacecraft size than ion collection does.

It is generally accepted also that high-voltage charging will occur only when the ambient electron plasma has a relatively large fraction of its total flux at energies well above the secondary-yield maximum of the spacecraft surface material(s), so that secondary electrons are not emitted in sufficient numbers to discharge the spacecraft. This situation involves "threshold" behaviour, with a large increase in surface charging produced by very small changes in the ambient distribution near the threshold condition (Rubin et al, 1978; Garrett and Rubin, 1978; Besse, 1981; Garrett, 1981; Laframboise et al, 1982; Meyer-Vernet, 1982; Laframboise and Kamitsuma, 1983; Lai et al, 1983; Olsen, 1983; Mullen et al, 1986; Katz et al, (1986). It is also accepted that the spacecraft must be in darkness, because the flux of photoelectrons from spacecraft surfaces, which is in the range $10\text{-}50\ \mu\text{A}/\text{m}^2$ for most surface materials (Feuerbacher and Fitton, 1972; Grand, 1973) is generally larger than the flux of high-energy auroral electrons encountered during known polar-orbit charging events, which is usually about $10\ \mu\text{A}/\text{m}^2$ (Gussenhoven et al, 1985, Fig. 11). However, this is not always the case; the two "type-1" auroral-electron distributions reported by Yeh and Gussenhoven (1987, Table 2a) have fluxes of 57 and $42\ \mu\text{A}/\text{m}^2$.

Laframboise (1985a, 1988) pointed out that magnetic-field effects may suppress secondary-electron escape and thereby increase the likelihood of high-voltage charging. Escape of photoelectrons should be suppressed similarly, because secondary electrons and photoelectrons both have relatively low average energies of emission, such that Maxwellian fits to their emission-velocity distributions give temperatures of about 3eV and 1.5eV respectively (Sternglass, 1954; Hachenberg and Brauer, 1959; Chung and Everhart, 1974; Hinteregger et al, 1959; Feuerbacher and Fitton, 1972; Grand, 1973; Wrenn and Heikkila, 1973). However, no examples of daylight polar-orbit high-voltage charging have so far been seen. In Section 3 of this Report, we examine this suppression effect in detail. In Section 4, we examine another effect, the wake-induced-barrier effect, which can also suppress secondary-electron or photoelectron emission from surfaces in the wake of a large dielectric-covered spacecraft. Either of these effects may produce local high-voltage charging in circumstances which would not produce overall charging. In particular, they extend, to lower equivalent temperatures, the range of auroral-electron plasma conditions in which one can expect such a spacecraft to undergo high-voltage charging.

In Section 5 of this Report, we present preliminary results from a numerical simulation which was constructed for the purpose of making detailed tests of the predictions made in Sections 2-4. This work involves calculations of floating-potential distributions on infinite dielectric cylinders in collisionless plasma crossflows whose properties model those of the auroral plasma.

Section 6 contains some concluding remarks. We use SI units throughout.

2. ESTIMATE OF REQUIRED ENVIRONMENTAL CONDITIONS FOR LOW-POLAR-ORBIT CHARGING.

In this Section, we develop a simple rough estimate of the conditions necessary for high-voltage whole-body charging of a large spacecraft in low polar orbit, and we show that spacecraft surface potentials are likely to depend more strongly on the ratio of ambient flux of *high-energy* electrons to that of *all* ions than on any other applicable environmental parameter. To do this, we make the following approximations:

(1) In this Section, we assume that magnetic-field effects on charged-particle motion are negligible. This assumption should be acceptable for initial estimates because the gyroradii of ions and high-energy electrons are generally a few meters or larger, especially in a high-voltage sheath (Table 1), and collection of "cold" (~ 0.1 eV) ionospheric electrons by a negatively-charged spacecraft will be very small, so their density is well-approximated by a Boltzmann factor, independently of the presence of a magnetic field. In Sec. 3, we return to the question of magnetic-field effects.

(2) We assume that ambient high-energy electrons have an isotropic velocity distribution. Large departures from this have been observed in auroral-plasma conditions (Fennell et al, 1981; Lin and Hoffman, 1982; W.J. Burke, 1984, private communication; Yeh and Gussenhoven, 1987), but this should not seriously affect the type of rough estimate made here. Parks and Katz (1981) and Katz and Parks (1983) assumed both the ion and electron fluxes to be unidirectional; we discuss this point later in this Section.

(3) We ignore secondary-electron emission; magnetic-field effects would tend to suppress this on some parts of the spacecraft in any case [Laframboise (1983a, 1985); Sec. 3].

(4) We assume that the spacecraft is a unipotential sphere, large compared to the typical ambient Debye length of $\lesssim 1$ cm (Table 1). We consider only *overall* charging of the spacecraft. This neglects the possibility that *local* high-voltage charging may occur, especially on surfaces in the spacecraft wake (Sections 3-5).

(5) We assume that both ions and electrons have double-Maxwellian velocity distributions, with the colder component in either case having a temperature of 0.1 eV, and the hotter 1 keV or larger. In the spacecraft reference frame, these are superposed on a drift velocity equal and opposite to the spacecraft velocity.

(6) Ions are assumed to be either H^+ or O^+ .

Note that assumption (3) could cause a false prediction that high-voltage charging occurs, while assumption (4) could cause a false prediction that it does not. The effects of assumptions (1), (2), and (5) are less clear; these could conceivably either increase or decrease predicted surface potentials. With regard to (6), assuming that the ions are H^+ results in maximum wake-filling by ions. If there are any electrically-isolated surfaces in the spacecraft wake, this would result in decreased surface potentials (magnitudes); assuming O^+ gives the reverse (see also Sec. 4).

Probably the most serious difficulty in formulating a theory for low-orbit charging is the prediction of ion collection on downstream surfaces. As mentioned in assumption (4) above, we avoid this difficulty by considering only total, rather than

local, ion collection, on a unipotential sphere. We return to the question of local ion collection in Sec. 4. Kanal [1962, Eq. (63)] gives an expression for the total ion current collected by such a sphere from a drifting Maxwellian plasma in the limit of zero potentials (relative to space potential), as follows:

$$i_i = \frac{1}{2} \left[\pi^{\frac{1}{2}} \left(S_i + \frac{1}{2S_i} \right) \text{erf}(S_i) + \exp(-S_i^2) \right] \quad (2.1)$$

where $i_i = I_i/I_{oi}$, I_{oi} is the ion random current $en_{i\infty} (kT_i/2\pi m_i)^{\frac{1}{2}}$, $S_i = U/(2kT_i/m_i)^{\frac{1}{2}}$ is the ion speed ratio, U is the ion drift speed relative to the spacecraft, e is the magnitude of the electronic charge, k is Boltzmann's constant, and m_i , T_i , and $n_{i\infty}$ are ion mass, temperature, and ambient number density. We assume that $U = 8$ km/sec, corresponding to low circular orbit.

We need to take account of the effect of a large ion-attracting surface potential on ion collection, in the limit of small Debye length λ_D compared to the sphere radius r_s . To do this, we use a result of Parrot et al (1982). These authors show that for a probe in a collisionless, nonmagnetized, Maxwellian plasma having $T_i/T_e = 1$ and *without* ion drift, and in the limit when $\lambda_D/r_s \rightarrow 0$ but $-e\phi_s/kT \gg 1$ [where ϕ_s is surface potential relative to space, and these limits must be approached in such a way that $(-e\phi_s/kT)(\lambda_D/r_s)^{4/3}$ remains $\ll 1$, i.e., sheath thickness remains \ll sphere radius], the ion (attracted-particle) current is larger than the random current by a factor of 1.45. This factor represents the effect of "presheath" electric fields on ion collection. Even though several of their assumptions are unfulfilled in our case, the resulting effects on ion collection are probably small enough for our purposes. We therefore multiply Eq. (2.1) by the same factor to obtain an estimate of total ion collection as influenced by surface-potential effects. The resulting ion-current

dependence on ion speed ratio is plotted in Fig. 2.1. For O^+ ions at $T = 0.1$ eV (1160K), H^+ at 0.1 eV, O^+ at 1keV, and H^+ at 1keV, we have $S_i = 7.31, 1.83, 0.0731$, and 0.0183 (the latter two are effectively zero), respectively. The corresponding ion-current enhancement factors (values of i_i) from Fig. 2.1 are 9.50, 2.69, 1.45, and 1.45, respectively.

If the ambient ions are H^+ , the ion collected current is now given by:

$$I_i = 4\pi r_s^2 n_{ic} \left\{ \frac{kT_{ic}}{2\pi m_i} \right\}^{\frac{1}{2}} \quad (2.69) \quad (2.2)$$

$$+ 4\pi r_s^2 n_{ih} \left\{ \frac{kT_{ih}}{2\pi m_i} \right\}^{\frac{1}{2}} \quad (1.45)$$

where the subscripts ic and ih refer to the cold and hot ion populations. If the ions are O^+ , then the factor 2.69 in (2.2) should be replaced by 9.50.

The electron collected current is:

$$I_e = 4\pi r_s^2 n_{ec} \left\{ \frac{kT_{ec}}{2\pi m_e} \right\}^{\frac{1}{2}} \exp\left\{ \frac{e\phi_s}{kT_{ec}} \right\} \quad (2.3)$$

$$+ 4\pi r_s^2 n_{eh} \left\{ \frac{kT_{eh}}{2\pi m_e} \right\}^{\frac{1}{2}} \exp\left\{ \frac{e\phi_s}{kT_{eh}} \right\}.$$

If high-voltage charging occurs, then $-e\phi_s \gg kT_{ec}$, and the first term on the right-hand side of this equation becomes negligible.

For current balance, $I_i = I_e$. This leads to:

$$2.69n_{ic} \sqrt{T_{ic}} + 1.45n_{ih} \sqrt{T_{ih}} = n_{eh} \sqrt{m_i/m_e} \sqrt{T_{eh}} e^{-e|\phi_s|/kT_{eh}} \quad (2.4)$$

where $\sqrt{m_i/m_e} = 43$ for H^+ ions. Therefore:

$$e|\phi_s|/kT_{eh} = \ln \left[\frac{43n_{eh} \sqrt{T_{eh}}}{2.69n_{ic} \sqrt{T_{ic}} + 1.45n_{ih} \sqrt{T_{ih}}} \right] \quad (2.5)$$

for H^+ ions, with 43 and 2.69 replaced by 172 and 9.50 for O^+ ions. This is equivalent to:

$$e|\phi_s|/kT_{eh} = \ln \left[\frac{\text{hot-electron ambient flux}}{2.69 (\text{cold-ion ambient flux}) + 1.45 (\text{hot-ion ambient flux})} \right] \quad (2.6)$$

For high-voltage charging to become probable, the argument of the \ln function must be close to or larger than $e \approx 2.72$, i.e:

$$\frac{\text{hot-electron ambient flux}}{2.69(\text{cold-ion ambient flux}) + 1.45(\text{hot-ion ambient flux})} \gtrsim 2.72. \quad (2.7)$$

For O^+/H^+ mixtures and for hot-ion temperatures other than 1 keV, generalization of this result is straightforward. Since any hot ions are likely to have $T_{ih}/T_{ic} \approx 10^4$, the hot-ion ambient flux will exceed the cold-ion ambient flux if the hot ions constitute more than about 1% of the total ambient-ion number density. Equation (2.7) indicates that the onset of high-voltage charging can be expected to depend primarily on the ratio of hot-electron ambient flux to the ambient flux of *all* ions, as

mentioned at the beginning of this Section. This completes our argument in support of this conclusion.

In analyzing spacecraft data, one is therefore likely to find better correlation of spacecraft voltages with the ratio which appears in Eq. (2.7), or something nearly equal to it, than with any other measurable quantity, such as electron or ion density or average energy, taken individually. This expectation has been borne out in recent work by Gussenhoven et al (1985, Fig. 7), involving charging data from the DMSP F6 and F7 satellites. In calculating values of this ratio, the ambient fluxes which are involved need to have been measured *simultaneously* on the same spacecraft. Even though the approximations made in deriving (2.7) are severe, and the precise dependence of spacecraft voltages on this ratio may therefore differ substantially from that given in Eq. (2.7) (and the coefficients in (2.7) will need to be modified if O^+ dominates), our general conclusion, i.e. that spacecraft voltages should correlate most strongly with this ratio, or something nearly equal to it, is likely to remain valid. Furthermore, the dependence of spacecraft voltages on this flux ratio is likely to retain an approximately exponential form. In situations where most secondary and backscattered electrons emitted by the spacecraft will escape (see Sec. 3), primary-electron incident fluxes will be approximately cancelled for many spacecraft materials by electron escape at incident energies up to a few keV (Laframboise et al, 1982a,b; Laframboise and Kamitsuma, 1983; Lai et al, 1983), so the hot-electron ambient flux term in (2.7) needs to be modified accordingly.

The most serious approximation made in deriving (2.7) is probably item (4) in the list at the beginning of this Section. This is because ion fluxes on downstream surfaces are likely to be very much smaller than their average over the entire spacecraft (see also Sections 3-5). They are also likely to be strongly dependent on spacecraft geometry, local surface potential distribution, and O^+/H^+ concentration ratio. Therefore, the critical value of ambient flux ratio, at which the onset of high-

voltage charging occurs, is likely to vary substantially among spacecraft having different geometries and surface materials. In particular, for spacecraft having electrically-isolated downstream surfaces, this critical ratio is likely, because of local charging on these surfaces, to be much lower than for spacecraft which have an entirely conductive surface (Sections 3-5).

Furthermore, in contrast with the situation for total ion collection, no known, simple, reliable method has been available for estimating ion fluxes on downstream surfaces. Parks and Katz (1983, Sec. 4; 1985) have developed an ion flux and density calculation for the downstream point on a sphere in a model potential which has a given, simple analytic form. In Sec. 4.3 and Appendix C we use a similar method to develop an ion density calculation for the downstream location on a cylinder in a collisionless crossflow. Detailed numerical simulation, which includes realistic self-consistent spacecraft sheath potential distributions, and which probably needs to involve at least some ion orbit-following, will be essential to determine the accuracy of such approximations. In Sec. 5, we report on preliminary results from a calculation of this kind.

So far, we have not mentioned the difficulties which can arise in measuring the ambient ion fluxes which appear in Eq. (2.7). So far, we have also defined "ambient flux" to be that measured in an Earth-fixed reference frame. The alternative would be to define it as that measured in the spacecraft frame, i.e., including ram effects. Ion fluxes measured by spacecraft instruments are strongly influenced by ram effects. In fact, the numerical factors 2.69, 1.45, and 9.50, which appear in Eq. (2.7) and the associated discussion, already constitute a rough ram-effect correction, but for *total* current to a sphere, not for *local* collection by a forward-facing instrument aperture. It may happen that the ram-effect correction factors for an instrument are nearly equal to the above factors, so that the instrument measure-

ment, without any correction, already gives a good estimate of the denominator of Eq. (2.7). In any case, the response of the instrument will depend on its geometry, and this problem has already been treated by other authors (Parker, 1970; Parker and Whipple, 1970; Whipple et al, 1974; Chang et al, 1979; Singh and Baugher, 1981; Comfort et al, 1982; Laframboise, 1983b), so we do not discuss it here.

Parks and Katz (1981) and Katz and Parks (1983) have estimated charging potentials on spherical spacecraft of 0.5m and 5m radius, assuming that the ions are O^+ , the hot-electron temperature T_{eh} is 5 keV, and spacecraft speed is 8 km/sec. Their results can be compared directly with those given by our Eqs. (2.5) - (2.7). They have used the theory of Langmuir and Blodgett (1924) to obtain values for sheath radius as a function of spacecraft potential. They present spacecraft potentials as functions of the ratio κ of hot ("precipitating") electron ram current to ion ram current. To make a comparison, their value of κ needs to be expressed in terms of our ambient flux ratio. They have assumed the ambient electron flux to be unidirectional. To convert to an equivalent isotropic flux, we note that current to a sphere = $4\pi r_s^2 \times$ isotropic (random) flux, but = $\pi r_s^2 \times$ unidirectional (ram) flux. Therefore, equivalent isotropic flux = $\frac{1}{4} \times$ unidirectional flux, for a sphere.

Also for a sphere, the ratio of ion ram to random currents is
 $U/(8kT_i/\pi m_i)^{\frac{1}{2}} = \frac{1}{2} \sqrt{\pi} S_i$. Using $S_i = 7.31$, this ratio = 6.48, so therefore:

$$\begin{aligned} \text{their } \kappa &= \frac{\text{hot electron ram current}}{6.48 \times \text{total ion random current}} \\ &= \frac{\pi r_s^2 \times \text{hot electron ram flux}}{6.48 \times 4\pi r_s^2 \times \text{total ion random flux}} \\ &= \frac{1}{6.48} \times \frac{\text{hot electron (equivalent) random flux}}{\text{total ion random flux}} \\ &= \frac{1}{6.48} \times \text{our flux ratio } R. \end{aligned} \tag{2.8}$$

With coefficients for O^+ used, our Eq. (2.6) gives:

$$\phi_s = -5000 \ln (R/9.50). \quad (2.9)$$

Figure 2.2 shows our result and theirs [from their Fig. 3 (1981) or Fig. 2 (1983)], plotted together. At larger potentials, the combined set of results shows a monotonic progression toward increased charging for larger spacecraft. For $-\phi_s < 350\text{V}$, their 5m sphere shows more charging than our large-radius-limit sphere. This is because their ion-current enhancement factor, which is determined by the size of a sharp-edged Langmuir-Blodgett sheath, falls below ours, which includes the effect of a quasineutral presheath. This discussion suggests that the tendency toward high-voltage charging always increases with spacecraft size, but magnetic-field effects may modify this (Laframboise, 1983a, Sec. 1; Laframboise, 1988, Sec. 1; see also Sec. 3.1 of this Report). The corresponding curves for *local* charging, on surfaces in a spacecraft wake, will lie to the left of those shown in Fig. 2.2, but these remain to be computed numerically, as we have done for a particular spacecraft geometry in Sec. 5.

3. CALCULATION OF ESCAPE CURRENTS OF ELECTRONS EMITTED FROM NEGATIVELY-CHARGED SPACECRAFT SURFACES IN A MAGNETIC FIELD.

3.1. INTRODUCTION TO THE ESCAPE-CURRENT PROBLEM

In Sec. 1, it was pointed out that in low Earth orbit, the geomagnetic field B is more likely to have an important influence on charged-particle motions than in geosynchronous orbit, because B is now much stronger, and not all of the average particle gyroradii of importance are any longer \gg typical spacecraft dimensions. In this Section, we wish to investigate an important consequence of this situation, which concerns the escape of electrons emitted from spacecraft surfaces. The emitted velocity distributions of secondary electrons and photoelectrons are frequently approximated, in both speed and direction, by Maxwellians corresponding to a temperature T close to 3 eV for secondary electrons (Sternglass, 1954; Hachenberg and Brauer, 1959; Chung and Everhart, 1974) and 1.5 eV for photoelectrons (Hinteregger et al, 1959; Feuerbacher and Fitton, 1972; Grand, 1973; Wrenn and Heikkila, 1973). Backscattered electrons have energy distributions which generally bear less resemblance to Maxwellians, and they also have much larger average energies (Sternglass, 1954, Fig. 8), so the treatment to be developed herein cannot be applied as readily to them. However, their contribution to the prevention of high-voltage spacecraft charging is generally less decisive than that of either secondary electrons or photoelectrons because their current contribution by its nature is always smaller than that of the incident "primary" electrons. A review of the properties of electron emission from surfaces in space has been given by Whipple (1981).

In low Earth orbit, in the auroral-zone geomagnetic field ($|\mathbf{B}|=0.44$ gauss $= 4.4 \times 10^{-5}\text{T}$), the gyroradii of a "typical" 3eV secondary electron, a 1.5 eV photoelectron, and a 10 keV auroral electron are 13 cm, 9 cm, and 8 m, respectively. The average gyroradius of "cold" ionospheric electrons (temperature $T = 0.1$ eV) in the same \mathbf{B} is even smaller (2 cm), but this is not an important parameter in most cases because these electrons are repelled if the spacecraft potential is negative, and their density is then well-approximated by a Boltzmann factor, which is unaltered by \mathbf{B} effects.

The reason why \mathbf{B} affects escape of emitted electrons is shown in Fig. 3.1. In Fig. 3.1(a), the spacecraft surface is perpendicular to \mathbf{B} , and the emitted electrons, which experience an electric force $-e\mathbf{E}$ directed away from the surface, all escape, helping to discharge it. In Fig. 3.1(b), the spacecraft surface is nearly parallel to \mathbf{B} , and almost all of the emitted electrons return to it, even though they still experience an electric force directed away from it.

These electrons therefore are unable to help discharge it, so a surface nearly parallel to \mathbf{B} is more likely to charge to a large negative voltage. Note that the component of \mathbf{E} which is perpendicular to \mathbf{B} results only in an $\mathbf{E} \times \mathbf{B}$ drift parallel to the surface.

For any object much larger than 13 cm, the escape of secondary electrons and photoelectrons will be strongly affected by this process. For example, most surfaces on the Shuttle are effectively "infinite planes" by this criterion. On the other hand, the average gyroradius of high-energy auroral electrons is comparable to Shuttle dimensions, so the deposition of these electrons onto Shuttle surfaces is likely to be only moderately inhibited.

For a larger object (size $\gg 8$ m), deposition of auroral electrons will also become strongly orientation-dependent, with both collection and escape of electrons now being inhibited on surfaces nearly parallel to **B**. This suggests that high-voltage charging of such surfaces may be more likely on objects of intermediate size than on either larger or smaller ones. In the calculation of Parks and Katz (1981), Katz and Parks (1983), the tendency toward high-voltage charging increased with spacecraft size because in their model, ion collection increased less rapidly with spacecraft size than did electron collection. To determine which of these two effects predominates will require more detailed calculations than have been done so far. The theory of magnetic-field effects on current collection by objects in space plasmas is still very incomplete (Parker and Murphy, 1967; Linson, 1969; Sanmartin, 1970; Laframboise and Rubinstein, 1976; Rubinstein and Laframboise, 1978, 1982, 1983; McCoy et al, 1980).

As already mentioned, strong ion flow effects also are generally present in low orbit; the ion speed ratios (flow speed/most probable ion thermal speed) for H^+ at 1 keV, H^+ at 0.1 eV, and O^+ at 0.1 eV are 0.02, 1.8, and 7.3, respectively. Whenever the latter is the predominant ion species, ion collection on downstream surfaces will be strongly inhibited. If a surface is simultaneously downstream and nearly parallel to **B**, as is likely to be the case in the auroral zones, then the tendency for high-voltage charging to occur on it will be greatly increased (Fig. 3.2). An extensive literature exists on wakes of satellites in low Earth orbit. Reviews of it have been given by Brundin (1963), Gurevich et al (1970), Whipple (1981), Samir and Stone

(1986), and Stone and Samir (1986). Most of this literature treats only low-voltage wakes and conductive spacecraft. Exceptions include Parks and Katz (1983a,b), Parker (1983) and Laframboise and Parker (1987).

To "straightforwardly" include **B** effects on electron escape in a large two or three dimensional simulation program would involve the numerical integration of very large numbers of emitted-electron orbits. The resulting computing costs usually would be formidable, especially since most of these orbits would have relatively large curvatures. A desirable alternative is to "parameterize" the situation by treating in advance a simplified but still sufficiently realistic model problem. Such a treatment also serves several other purposes. For particular situations, it permits simple estimates of the effects considered. It may help to stimulate experimental investigations of these effects. It also permits gaining an understanding of some of the major effects which govern the overall problem, and this can be its most important use. In Sections 3.2-3.5, we develop a "parameterization" of magnetic-field effects on escaping-electron currents. In Sec. 3.6, we propose a simple approximate method for calculating the space-charge-density distribution of escaping electrons.

3.2. THEORY FOR ELECTRIC FIELD NORMAL TO SURFACE

In order to develop a simplified treatment of electron escape, we make the following approximations. (1) We assume (Sec.3.1) that electrons are emitted from the spacecraft surface with a Maxwellian velocity distribution corresponding to a temperature T . (2) We assume that the spacecraft surface is an infinite plane, and the electric and magnetic fields \mathbf{E} and \mathbf{B} outside it are uniform and time-independent. (3) In this Section, we assume that the electric force $-e\mathbf{E}$ on electrons is directed along the outward normal to the surface; here e is the magnitude of the elementary charge. This assumption is relaxed in Sec. 3.4, in order to permit variations of potential along the surface to be taken into account.

If $-e\mathbf{E}$ is normal to the surface, our assumptions imply that the ratio $i = I/I_0$ of escaping to emitted flux is a function of two parameters: the angle θ between the surface normal and the direction of \mathbf{B} (Fig. 3.3), and a parameter describing the strength of \mathbf{E} . A convenient choice for this parameter is the difference in potential across the average emitted-electron gyroradius $\bar{a} = (1/eB)(\pi mkT/2)^{1/2}$, divided by kT/e , where m is electron mass and k is Boltzmann's constant.

This quotient is:

$$\epsilon \equiv \frac{E}{B} \sqrt{\frac{\pi m}{2kT}} \quad (3.1)$$

where $E \equiv |\mathbf{E}|$ and $B \equiv |\mathbf{B}|$.

This quantity also has an alternative, more useful interpretation: it is the ratio of the magnitude $|\mathbf{E} \times \mathbf{B}|/B^2$ of the $\mathbf{E} \times \mathbf{B}$ drift speed, to one-half the average thermal speed $(8kT/\pi m)^{1/2}$ of the emitted electrons. It is useful to estimate the value of ϵ for a high-voltage spacecraft sheath in low-orbit conditions. To do this, we use the spherically-symmetric sheath solution of Al'pert et al (1965, Table XXIV and Fig. 72). For a sphere of radius 3m having a surface potential of -1 kV or -5 kV relative to space, in a collisionless plasma having an ambient ion temperature of 0.1 eV, number density of $3 \times 10^5 \text{ cm}^{-3}$, and resultant (ion) Debye length of 0.43 cm, their results give, respectively, sheath thicknesses of 2.6 and 6.1 m, and surface electric fields $E = 0.86$ and 2.9 kV/m . Using $B = 4.4 \times 10^{-5} \text{ T}$ and $T = 3 \text{ eV}$ (1.5 eV) for secondary electrons (photoelectrons), we then obtain $\epsilon = 33.9$ and 114.2 (47.9 and 161.5). These are relatively large values, whose significance can be understood if we consider what would happen if ϵ were infinite.

In this limit, it is easy to show that emitted electrons would all escape unless \mathbf{B} were exactly parallel to the surface (θ were 90°). This can be shown as follows. In this limit, emitted electrons would have no "thermal" motion. The (y,z) projection of their motion would then be similar to that shown in Fig. 3.4. This motion would be the sum of: (i) an $\mathbf{E} \times \mathbf{B}$ drift in the y direction (ii) a uniform acceleration along \mathbf{B} , whose projection in the (y,z) plane would be upward (iii) just enough gyromotion to produce a cycloidal path when combined with (i), so that in the absence of (ii), the electron would (just) return to the surface at the end of each gyroperiod. In the presence of (ii), these "return points" are displaced upward by progressively increasing amounts

(Fig. 3.4), so the electron can never return to the surface, unless \mathbf{B} is exactly parallel to the surface, so that the upward component of $-e\mathbf{E}$ along \mathbf{B} vanishes.

This result suggests that for large finite values of ϵ (including the values calculated above), electron escape is likely to be almost complete except for θ very near 90° , where it should drop to zero very steeply. The occurrence of high-voltage charging in marginal circumstances may therefore depend very strongly on the precise orientation of a surface.

The escaping electron flux is given by:

$$\begin{aligned}
 I &= \iiint f(\mathbf{v}_0) H(\mathbf{v}_0) v_{oz} d^3\mathbf{v}_0 \\
 &= \int_{-\infty}^{\infty} dv_{ox} \int_{-\infty}^{\infty} dv_{oy} \int_0^{\infty} n \left\{ \frac{m}{2\pi kT} \right\}^{3/2} \exp\left\{ -\frac{mv_0^2}{2kT} \right\} H(v_{ox}, v_{oy}, v_{oz}) v_{oz} dv_{oz}
 \end{aligned} \tag{3.2}$$

where: \mathbf{v}_0 is the initial velocity of an emitted electron, $f(\mathbf{v}_0) \equiv d^3n/d^3\mathbf{v}_0$ is the velocity distribution of emitted electrons, n is a reference number density, and $H(\mathbf{v}_0)$ is equal to 1 for escaping electrons and 0 for those which return to the surface. The emitted flux is:

$$I_0 = n(kT/2\pi m)^{1/2}. \tag{3.3}$$

We also introduce the dimensionless velocity:

$$\mathbf{u} = \mathbf{v} (m/2kT)^{1/2}. \tag{3.4}$$

Equation (3.2) then becomes:

$$\begin{aligned}
 \frac{I}{I_0} &= \frac{2}{\pi} \int_{-\infty}^{\infty} \int_{-\infty}^{\infty} du_{ox} du_{oy} e^{-u_{ox}^2 - u_{oy}^2} \int_0^{\infty} du_{oz} u_{oz} e^{-u_{oz}^2} H(u_{ox}, u_{oy}, u_{oz}) \\
 &= \frac{1}{\pi} \int_{-\infty}^{\infty} \int_{-\infty}^{\infty} du_{ox} du_{oy} \exp(-u_{ox}^2 - u_{oy}^2) \sum_{k=1}^{k_{\max}(u_{ox}, u_{oy})} (-1)^{k+1} \\
 &\quad \times \exp[-u_{\text{lim},k}^2(u_{ox}, u_{oy})] \\
 &\approx \frac{1}{\pi} \sum_i \sum_j \Delta u_{ox,i} \Delta u_{oy,j} \exp(-u_{ox,i}^2 - u_{oy,j}^2) \sum_{k=1}^{(k_{\max})_{i,j}} (-1)^{k+1} \\
 &\quad \times \exp[-(u_{\text{lim},k}^2)_{i,j}] \quad (3.5)
 \end{aligned}$$

which is in a form suitable for numerical summation. The quantities $u_{\text{lim},1}$, $u_{\text{lim},2}, \dots, u_{\text{lim},k_{\max}}$ are the values of u_{oz} for which H changes between 0 and 1 for each u_{ox} and u_{oy} . These values must be found by numerically determining which particle orbits reimpact the surface. These orbits can, however, be determined in analytic form, with time as a parameter. To do this, we use the coordinate system shown in Fig. 3.3, together with a y -axis (not shown) directed into the plane of the Figure. The equation of motion for an electron is:

$$\dot{\mathbf{v}} = -\frac{e}{m} (\mathbf{E} + \mathbf{v} \times \mathbf{B}). \quad (3.6)$$

We solve this with the initial conditions $\xi = y = \eta = 0$, $v_{\xi} = v_{ox}$, $v_y = v_{oy}$, and $v_{\eta} = v_{oz}$. We introduce the dimensionless variables:

$$\epsilon_x = \frac{E_x}{B} \sqrt{\frac{\pi m}{2kT}}, \quad \epsilon_y = \frac{E_y}{B} \sqrt{\frac{\pi m}{2kT}}, \quad \text{etc;}$$

$$\tilde{x} = x/\bar{a}, \tilde{y} = y/\bar{a}, \text{ etc;} \quad (3.7)$$

$$\tau = \omega_c t = (eB/m)t.$$

In the present discussion, ϵ_x and ϵ_y are both zero, but for later use (Sections 3.4 and 3.5), we have retained these quantities in the formulas below. We obtain:

$$u_{o\xi} = u_{ox} \sin \theta + u_{oz} \cos \theta;$$

$$u_{o\eta} = -u_{ox} \cos \theta + u_{oz} \sin \theta;$$

$$\tilde{\xi} = \frac{-1}{\pi} \epsilon_\xi \tau^2 + \frac{2}{\sqrt{\pi}} u_{o\xi} \tau; \quad (3.8)$$

$$\tilde{y} = \left\{ \frac{2}{\sqrt{\pi}} u_{oy} - \frac{2}{\pi} \epsilon_\eta \right\} \sin \tau + \left\{ \frac{2}{\sqrt{\pi}} u_{o\eta} + \frac{2}{\pi} \epsilon_y \right\} (\cos \tau - 1) + \frac{2}{\pi} \epsilon_\eta \tau;$$

$$\tilde{\eta} = \left\{ \frac{2}{\sqrt{\pi}} u_{o\eta} + \frac{2}{\pi} \epsilon_y \right\} \sin \tau + \left\{ \frac{2}{\sqrt{\pi}} u_{oy} - \frac{2}{\pi} \epsilon_\eta \right\} (1 - \cos \tau) - \frac{2}{\pi} \epsilon_y \tau;$$

$$\tilde{z} = \tilde{\xi} \cos \theta + \tilde{\eta} \sin \theta.$$

Equations (3.8) can also be differentiated to find $d\tilde{z}/d\tau$. The numerical procedure for finding the quantities $u_{lim,k}$ in Eq. (3.5) then involves calculating \tilde{z} and $d\tilde{z}/d\tau$ at a succession of points along an orbit (the electron will reimpact during the first gyroperiod $0 < \tau \leq 2\pi$ if at all, so this interval always suffices), and making the appropriate tests on these quantities to find out whether the orbit reimpacts or escapes. For each $u_{ox,i}$ and $u_{oy,j}$, this is done for a succession of values of u_{oz} . These tests also yield the local minimum of $\tilde{z}(\tau)$ if one exists. Whenever a change occurs between no escape and escape from one such value of u_{oz} to the next, an interpolation using these

minima can be used to provide the corresponding value of $u_{lim,k}$. In cases where they are unavailable, the arithmetic mean of the two successive u_{oz} values is used.

We have chosen the abscissas $u_{ox,i}$ and $u_{oy,j}$ in Eq. (3.5) by first solving numerically the transcendental equation $\frac{1}{2} + \frac{1}{2} \operatorname{erf}(u_k/\sqrt{2}) = k/n$ for $k = 1, 2, \dots, n-1$. The resulting values u_k then subdivide the normalized Gaussian distribution $\exp(-u^2)/\sqrt{\pi}$ into n "slices" whose areas decrease as $\exp(-\frac{1}{2}u_k^2)$ when n is large. In terms of these u_k , we then choose values $u_{o,k}$ at the centroids of these slices, and weights c_k equal to the areas under each. We obtain:

$$u_{o,k} = \frac{\exp(-u_{k-1}^2) - \exp(-u_k^2)}{\sqrt{\pi}(\operatorname{erf} u_k - \operatorname{erf} u_{k-1})} \quad (3.9)$$

$$c_k = \frac{1}{2}(\operatorname{erf} u_k - \operatorname{erf} u_{k-1}) \quad (3.10)$$

for $k = 1, 2, \dots, n$. A convenient method for calculating the required values of $\operatorname{erf} u = 1 - \operatorname{erfc} u$ has been given by Shepherd and Laframboise (1981). The resulting values $u_{o,k}$ are then used to provide the required values of $u_{ox,i}$ and $u_{oy,j}$, and the c_k are used to provide values of $(1/\sqrt{\pi}) \Delta u_{ox,i} \exp(-u_{ox,i}^2)$ and $(1/\sqrt{\pi}) \Delta u_{oy,j} \exp(-u_{oy,j}^2)$, for use in Eq. (3.5). We have provided values of u_{oz} for use in determining the $u_{lim,k}$ values in Eq. (3.5) by solving the equation $1 - \exp(-u_{oz,k}^2/2) = k/n$ for $k = 0, 1, 2, \dots, n-1$. This gives $u_{oz,k} = \{2 \ln[1/(1-k/n)]\}^{1/2}$; these values are distributed most densely near $u_{oz} = 0$, but still densely enough at large u_{oz} that the resulting intervals give vanishing flux contributions in this limit. This completes the definition of the procedure used for calculating the ratio I/I_0 of escaping to emitted flux. The computer program used for performing this calculation is listed in Appendix A.

3.3. RESULTS AND DISCUSSION FOR ELECTRIC FIELD NORMAL TO SURFACE

Current densities of escaping electrons, computed as described in Sec. 3.2, are shown in Table 2 and Fig. 3.5. Each value of $i = I/I_0$ was calculated using $80 \times 80 \times 40$ orbits, whose initial velocity components u_{ox} , u_{oy} , and u_{oz} were chosen as described in Sec. 3.2, and with points on the orbits calculated at intervals $\Delta\tau = \pi/45$. With these increments, the results have a numerical accuracy of about 0.2% or better. For 8 values of ϵ and 11 values of θ , the resulting calculation took about 100 hr total on a Hewlett-Packard 1000F computer with Vector Instruction Set. The result for $\epsilon = 0$ is just the analytic result $i = \cos \theta$. To see why this is so, we consider the electron orbit shown in Fig. 3.6, which has been fictitiously extended so as to pass through the surface and re-emerge from it. In the absence of an electric field ($\epsilon = 0$), this orbit has the same speed at the re-emergence point C as at the emission point A. Since we have also assumed that the emitted velocity distribution is isotropic, and therefore a function of speed only, the real orbit, for which C is the emission point, must carry the same population as would the fictitious re-emerged orbit. The flux crossing the reference surface DE, which is $\perp \mathbf{B}$, is therefore the same as if such passages and re-emergences actually occurred, and is the same as if another reference surface FG, also $\perp \mathbf{B}$, were emitting electrons having the same velocity distribution. However, in reality, the electrons come from the real surface HJ, which is not $\perp \mathbf{B}$, and all the electron-orbit guiding centers which are inside any given magnetic-flux tube through DE will also be inside the projection of the same flux tube onto

HJ, and the ratio of the intersection areas of this tube with HJ and DE is just $\sec \theta$. The ratio of escaping to emitted flux must therefore be the reciprocal of this, or $\cos \theta$, as stated above.

Also evident in Fig. 3.5 is the fact, mentioned in Sec. 3.2, that when ϵ is large enough, electron escape becomes essentially complete except when θ is very nearly 90° . This means that in Shuttle high-voltage charging conditions, for which $30 \leq \epsilon \leq 160$ (Sec. 3.2), the occurrence of high-voltage charging in marginal circumstances may depend very strongly on the precise orientation of a surface. A slowly-rotating surface which passes through tangentiality to B may experience a sudden, brief high-voltage charging event. For the same reason, attempts to predict high-voltage charging may be afflicted by "sensitivity effects", which are defined as large changes in predicted results resulting from small changes in physical input parameters. An important consequence of sensitivity effects here is that if one attempts to predict "worst-case" charging by assuming that emitted electrons do not escape, then the resulting predictions are likely to be overly pessimistic most of the time. On the other hand, if one assumes that they do escape, correct predictions will be obtained almost all of the time, but occasionally a large underestimate of charging will occur. A different kind of sensitivity effect, involving ambient electron distributions which are almost Maxwellians having temperatures close to the "threshold temperature for high-voltage charging" of the spacecraft surface material, was identified by Laframboise et al (1982a) and Laframboise and Kamitsuma (1983); see also Schnuelle et al (1981, Fig. 4).

The results for i in Table 2 are approximated with an absolute error of 2.5% or less by the empirical formula:

$$\begin{aligned}
 b_1 &= 1 + 1.35\epsilon^{1.1394} \exp \left\{ 0.083725 \left\{ 1 + \tanh \left[1.9732 \ln \left(\frac{\epsilon}{1.13} \right) \right] \right\} \right. \\
 &\quad \left. - 0.07825 \ln \left[1 + (\epsilon/8.5)^{1.78148} \right] \right\}; \\
 b_2 &= 0.38033\epsilon^{0.95892} \exp \left\{ 2.0988 \left\{ 1 + \tanh \left[1.49 \ln \left(\frac{\epsilon}{3.26} \right) \right] \right\} \right\}; \\
 c &= \ln (90^\circ/\theta); \\
 i &= \cos [90^\circ \exp(-b_1 c - b_2 c^2)].
 \end{aligned} \tag{3.11}$$

This formula also has the correct limiting behavior when $\epsilon \rightarrow 0$ or ∞ , or $\theta \rightarrow 0^\circ$ or 90° . In order to calculate the escaping flux using (3.11), one also needs to know the emitted flux I_o . For photoemission, values of I_o for various spacecraft materials have been given by Feuerbacher and Fitton (1972) and Grand (1973). For secondary and backscattered emission, analytic approximations for fractional yields (I_o /incident flux) as functions of incident energy and direction have been given by Laframboise et al (1982a) and Laframboise and Kamitsuma (1983); see also Katz et al (1986). The results presented in this Section have already been presented by Laframboise (1985).

In a real situation, E would not be uniform, but would decrease with distance from the surface, contrary to our assumptions. Our results can therefore be expected to overestimate electron escape. This would probably not be a large effect. For example, the spherical-sheath thicknesses mentioned in

Sec. 3.2 for -1kV and -5kV surface potentials are 2.6 and 6.1 m, so variations of E will be small within the 13 cm gyroradius of a 3eV emitted electron. If desired, one can make an approximate compensation for this nonuniformity by calculating ϵ using an electric field value which is averaged over the first average-gyroradius distance from the surface.

3.4. THEORY FOR NON-NORMAL ELECTRIC-FIELD DIRECTIONS

If a spacecraft surface is charged to a nonuniform potential, the electric field E outside it has a nonzero component tangential to the surface. The resulting problem geometry is more complicated, and two additional angles, α and ψ , which define the direction of the electric force $-eE$, need to be specified (Fig. 3.7). We still assume that E and B are uniform, as in Sec. 3.2.

It may then happen that even though $-eE$ is still directed away from the surface, its projection along the direction of B is directed toward the surface, as shown in Fig. 3.8a. This happens when the angle between $-eE$ and either B or B , whichever is outward, is greater than 90° . The resulting situation is analogous to that for a sailboat tacking against the wind (Fig. 3.8b).

When this situation exists, every emitted electron returns to the surface, and the escaping flux is zero. The resulting situation then differs from that shown in Fig. 3.5 in at least one important respect. The range of surface orientations (relative to B) for which electron escape is entirely prevented, is no longer infinitesimal (at $\theta = 90^\circ$), but finite, and this may greatly enlarge

the portion of a spacecraft's surface for which secondary-electron or photo-electron escape is not available as a discharge mechanism.

Even though no electrons escape under these conditions, the possibility exists that they may travel a relatively long distance, equal to many gyro-radii, parallel to the surface before returning. This may produce relatively large surface currents, and these may modify substantially the charge distribution on the spacecraft. The question of surface currents resulting from migration of reimpacting electrons along the surface remains to be examined in detail; this situation is discussed in Section 6. Here, we point out only one general feature of this charge migration. The general motion of an emitted electron is a superposition of gyromotion about \mathbf{B} , an $\mathbf{E} \times \mathbf{B}$ drift, and an acceleration in the \mathbf{B} or $-\mathbf{B}$ direction. The $\mathbf{E} \times \mathbf{B}$ drift direction may have either an inward or outward normal component. If it is outward, migration distances over the surface will be larger, and so therefore will surface currents. Since \mathbf{B} is in the (x,z) plane, the z -component of $\mathbf{E} \times \mathbf{B}/B^2$ is $-B_x E_y/B^2$. For $B_x > 0$, this component has a sign opposite to that of E_y . Therefore, when $E_y < 0$ [region (3) in Fig. 3.9], the migration distances of reimpacting electrons, and therefore also the surface currents produced by them, are likely to be much larger than when $E_y > 0$ [region (2) in Fig. 3.9]. These surface currents will be primarily along the tangential projection of the $\mathbf{E} \times \mathbf{B}$ drift direction, rather than of $-\mathbf{eE}$, so they may have little effect on helping to discharge the spacecraft. For some orientations of \mathbf{E} and \mathbf{B} , emitted electrons may gain enough kinetic energy before reimpacting to cause substantial amounts of secondary emission to occur when they do so. Surface currents

then may be greatly increased by "electron multiplier" effects (Goodrich and Wiley, 1961; Wiley and Hendee, 1962).

Our predictions are based on the assumption that \mathbf{E} and \mathbf{B} are spatially uniform and time-independent. However, if average migration distances become equal to many gyroradii, it is then more likely that spatial uniformity will be seriously violated, and many of our predictions, especially the quantitative ones presented in Sec. 3.5, may then become unreliable. The same circumstances increase the possibility that time-dependent phenomena (plasma turbulence) may also affect our predictions. This possibility may be remote, because the spontaneous plasma oscillations observed recently in the disturbed region around the Shuttle are of relatively small amplitude. They involve relative density fluctuations ($\Delta n/n$) of at most a few percent, and the largest amplitudes of these fluctuations generally do not occur close to the spacecraft's surfaces (Murphy, 1985; Murphy et al, 1986). However, this question remains to be thoroughly explored.

Before we present computed results, we need to determine, in terms of the angles θ , α , and ψ in Fig. 3.7, when the projection of $-e\mathbf{E}$ along \mathbf{B} is directed toward the surface. This projection is:

$$(-e\mathbf{E} \cdot \mathbf{B})\mathbf{B}/B^2 \quad (3.12)$$

The z-component of this is:

$$\begin{aligned} & -e(E_x B_y + E_z B_z) B_z/B^2 \\ & = -eE \cos^2 \theta \cos \alpha (1 + \tan \alpha \cos \psi \tan \theta) \end{aligned} \quad (3.13)$$

Since $-eE \cos^2 \theta \cos \alpha > 0$, this means that escape is prevented if:

$$\tan \alpha \cos \psi \tan \theta < -1, \quad (3.14)$$

or equivalently:

$$\begin{aligned} \theta &< \tan^{-1} (-\cot \alpha \sec \psi), \text{ for } 0 \leq \psi < 90^\circ; \\ \theta &> \tan^{-1} (-\cot \alpha \sec \psi), \text{ for } 90^\circ < \psi \leq 180^\circ. \end{aligned} \quad (3.15)$$

3.5. RESULTS AND DISCUSSION FOR NON-NORMAL ELECTRIC-FIELD DIRECTIONS

Figures 3.10 - 3.17 show escaping-electron current densities $i \equiv i(\alpha, \psi, \theta, \epsilon)$ when $-eE$ is not normal to the spacecraft surface ($\alpha \neq 0^\circ$). Details of the computations of these results are the same as those given in Sections 3.2 and 3.3, except that $64 \times 64 \times 32$ orbits were used for calculating each value of i , and the results have a numerical accuracy of about 0.4% or better.

In Figs. 3.10 and 3.11, $\psi = 0^\circ$, so $-eE$, B , and the surface normal are coplanar. The $E \times B$ drift direction is therefore tangential to the surface. In Fig. 3.10, no electrons escape ($i = 0$) when $-90^\circ \leq \theta < -60^\circ$ because the acceleration of all electrons along B is toward the surface, as discussed in Sec. 3.4. For $\theta > -60^\circ$, this acceleration is away from the surface, but it is larger for $\theta > 0^\circ$ than for $\theta < 0^\circ$, so increasing the electric field magnitude ϵ increases electron escape more for $\theta > 0^\circ$. For $\theta > -60^\circ$, $i = \cos \theta$ when $\epsilon = 0$, as was the case for $-eE$ normal to the surface (Fig. 3.5). Some care is needed in defining what is meant by the case " $\epsilon = 0$ ". For $90^\circ \leq \theta < -60^\circ$,

$i = 0$ in the limit $\epsilon \rightarrow 0+$, but in the limit $\epsilon \rightarrow 0-$, the electric field is reversed, so $i = \cos \theta$ in this limit, and i therefore has a discontinuity at $\epsilon = 0$. The discontinuity is reversed for $\theta > -60^\circ$. However, we are interested here primarily in cases when $\epsilon > 0$ (negatively-charged spacecraft surfaces), so in this work, we take " $\epsilon = 0$ " to mean the limiting case $\epsilon \rightarrow 0+$. In Fig. 3.11, α has been increased from 30° to 60° , so the effects just discussed in connection with Fig. 3.10 are seen again, but more strongly. This time, escape is suppressed completely for $-90^\circ \leq \theta < -30^\circ$.

In Fig. 3.12, the acceleration of electrons along \mathbf{B} is toward the surface, and therefore $i = 0$, for $\theta < \tan^{-1}(-\sqrt{6}) = -67.79^\circ$, as given by Eq. (3.15). Also, we now have $\psi \neq 0^\circ$, so the electric force vector is no longer in the same plane as \mathbf{B} and the surface normal. As a result, the $\mathbf{E} \times \mathbf{B}$ drift now has a nonzero normal component. This decreases electron escape for $\theta < 0^\circ$, and increases it for $\theta > 0^\circ$. It also causes the escape to remain nonzero at $\theta = 90^\circ$. As before, the larger outward acceleration along \mathbf{B} also increases escape for $\theta > 0^\circ$. For θ just larger than 67.79° , we see that escape is suppressed almost completely for larger values of ϵ ; this is because the inward direction of the $\mathbf{E} \times \mathbf{B}$ normal component causes most electrons to reimpact the surface during the first gyroperiod after emission. In Fig. 3.13, α has been increased from 30° to 60° , with consequent enhancement of the effects just discussed. We now have $i=0$ for $\theta < \tan^{-1}(-\sqrt{2/3}) = -39.23^\circ$.

In Figs. 3.14 and 3.15, $\psi = 90^\circ$, and the projection of $-e\mathbf{E}$ along \mathbf{B} is away from the surface for all θ , so suppression of electron escape by deceleration along \mathbf{B} does not occur. However, for θ close to 90° , the effect of the inward

direction of the $\mathbf{E} \times \mathbf{B}$ normal component overcomes the effect of the outward acceleration along \mathbf{B} , especially because \mathbf{B} is now nearly tangential to the surface, and therefore electron escape is effectively suppressed for larger values of ϵ . In Fig. 3.15, suppression for $\epsilon = 20$ is essentially complete over a range of θ values extending more than 30° on either side of $\theta = -90^\circ$.

In Figs. 3.16 and 3.17, we have $\psi = 135^\circ$, and the effects of electron deceleration along \mathbf{B} and of $\mathbf{E} \times \mathbf{B}$ drift now suppress electron escape at opposite ends of the range of θ . From Eq. (3.15), we now have $i = 0$ for $\theta > \tan^{-1}(\sqrt{6}) = 67.79^\circ$ and $\theta > \tan^{-1}(\sqrt{2/3}) = 39.23^\circ$, respectively. In Fig. 3.16, the $\mathbf{E} \times \mathbf{B}$ effect significantly enhances electron escape as θ increases, just before the deceleration effect cuts it off.

The results shown in Fig. 3.5 and Figs. 3.10-3.17 encompass, albeit rather sparsely, the entire range of possible directions of \mathbf{B} and \mathbf{E} for α up to 60° . To see this, we first note that in the important case where $-e\mathbf{E}$ is normal to the surface, the i values for $-90^\circ \leq \theta \leq 0^\circ$ can be generated from those for the range $0^\circ \leq \theta \leq 90^\circ$, which is covered in Fig. 3.5; this can be seen by rotating the \mathbf{B} vector in Fig. 3.7 by 180° about the z axis. Secondly, the i values for $\alpha = 30^\circ$ and 60° and $\psi = 180^\circ, 225^\circ, 270^\circ$, and 315° can be generated from those in Figs. 3.10-3.17 by rotating the \mathbf{B} and $-e\mathbf{E}$ vectors in Fig. 3.7 together about the z axis by 180° . The effect of this is to increase all the ψ values by 180° and also to reverse the sign of θ . Finally, we can obtain the i values for cases where \mathbf{B} is reversed by first noting that reversal of \mathbf{B} implies reversal of both the ξ coordinate in Fig. 3.7 (in order that ξ

remain parallel to \mathbf{B}) and the η coordinate [in order that the (ξ, y, η) axes remain right-handed]. The quantities $\sin \theta$, $\cos \theta$, $u_{o\xi}$, $u_{o\eta}$, $\tilde{\xi}$, ϵ_ξ , and ϵ_η in Eq. (3.8) will then all reverse. To keep $z \equiv z(\tau)$ in Eq. (3.8) unchanged, we require also that $\tilde{\eta}$ reverse, and we therefore require that ϵ_y and u_{oy} also be reversed. However, the emitted velocity distribution is symmetric in u_{oy} , and reversing ϵ_y involves replacing the angle ψ by $360^\circ - \psi$, and this replacement gives back the same set of ψ values for which our computations already give i .

We can summarize the results in Figs. 3.10-3.17 by noting that when $\alpha \neq 0$, two new mechanisms, which were not present when $-e\mathbf{E}$ was normal to the surface (Fig. 3.5), can suppress electron escape. These are: an inward normal component of $\mathbf{E} \times \mathbf{B}$, if ϵ is strong enough, and a decelerating projection of $e\mathbf{E}$ along \mathbf{B} , for any $\epsilon > 0$. These may act at the same end or at opposite ends of the range of magnetic-field directions $-90^\circ \leq \theta \leq 90^\circ$. These mechanisms can greatly enlarge the range of surface orientations for which escape is suppressed.

3.6. CALCULATION OF ESCAPING-ELECTRON DENSITIES

Once the fluxes of escaping electrons are known (Sections 3.3-3.5), a simple, inexpensive, approximate calculation of their space-charge density distribution can be set up. The proposed method is as follows: (1) ignore the gyromotion of electrons once they have escaped. Their motion then involves: (a) an acceleration along magnetic field lines, of amount $-(e/m)\mathbf{E} \cdot \mathbf{B}/B$ (b) a drift motion of velocity $\mathbf{E} \times \mathbf{B}/B^2$ across magnetic field lines. (2) Integrate enough of the trajectories defined by this motion (i.e. their guiding-center trajectories) to define trajectory tubes whose cross-section at any point can be calculated with sufficient accuracy; the method described by Laframboise et al (1982b, Sec. 7), can be used to calculate the area of a trajectory tube without reference to neighbouring trajectories. (3) Calculate their space-charge density $n(\mathbf{r})$ at any point by (a) ignoring the "thermal" spread of their velocities (b) then invoking the fact that their density \times their velocity [as given by the orbit integration mentioned in (2)], \times the cross-sectional area $A(\mathbf{r})$ of the trajectory tube (which must be calculated in a plane \perp the trajectory) at the point \mathbf{r} in question, = a constant (whose value is given by the initial conditions at the point on the spacecraft where the trajectory originates) (c) finding their velocity at the point in question by using energy conservation, together with the values of electric potential $\phi(\mathbf{r})$ and ϕ_0 at that point and the emission point, and their assumed velocity v_0 at the emission point. The result is:

$$n(\mathbf{r}) = n_0 v_0 A_0 / \left\{ A(\mathbf{r}) \sqrt{v_0^2 + (2e/m) [\phi(\mathbf{r}) - \phi_0]} \right\} \quad (3.16)$$

where $n_0 v_0$ is the escaping flux calculated in Sections 3.3-3.5. At most positions, $n(\mathbf{r})$ will be insensitive to the precise value assumed for v_0^2 ; assuming that $v_0 = \text{the one-sided thermal speed } (2kT/\pi m)^{1/2}$ will suffice for most purposes.

4. HIGH-VOLTAGE CHARGING OF A DIELECTRIC-COVERED SPACECRAFT: A WAKE-INDUCED BARRIER-EFFECT MECHANISM.

4.1. INTRODUCTION TO THE WAKE-INDUCED-BARRIER-EFFECT PROBLEM.

In Section 3, we examined the suppression of emitted-electron escape by magnetic fields. On a dielectric-covered spacecraft, this suppression can be expected to result in local high-voltage charging in certain kinds of auroral-plasma conditions which would not produce overall charging. This point is discussed further in Sections 1 and 6.

In this Section, we examine a different effect, namely the wake-induced-barrier effect, which produces a similar result, i.e. suppression of the escape of emitted electrons. Our work here is directed specifically to the situation of a large spacecraft with dielectric exterior surfaces either in the auroral plasma or emitting an electron beam as in the SEPAC Spacelab-1 experiment.

The study of Parks and Katz (1981), Katz and Parks (1983) concerned overall high-voltage charging of a conductive spacecraft. Our work in this Section shows that local high-voltage charging on a large dielectric spacecraft can be

expected to occur in the auroral ionosphere in conditions different than those already known to have produced high-voltage charging on other spacecraft. In Section 4.2, we describe the wake-induced-barrier effect, including the differences between it and the barrier effect on geosynchronous-altitude satellites. In Section 4.3, we develop theory for calculating spacecraft surface potentials produced by the wake-induced-barrier effect. In Sections 4.4 and 4.5, we apply this theory to spacecraft in the auroral plasma or emitting an electron beam, respectively.

4.2. DESCRIPTION OF THE WAKE-INDUCED-BARRIER-EFFECT MECHANISM

In low-orbit conditions, the plasma environment of a spacecraft is usually "mesothermal", i.e. it has ion mean thermal speed \ll spacecraft speed \ll electron mean thermal speed. Under these conditions, the ambient ion flux in the spacecraft reference frame is mostly from the upstream direction, whereas ambient electrons come more-or-less equally from all directions [unless the ambient electron distribution itself is highly anisotropic; see Fennell et al (1981), Lin and Hoffman (1982), and Yeh and Gussenhoven (1987)]. Relatively few ions are then able to reach the region just downstream of the spacecraft, and a "wake" region of unbalanced electron space charge forms there. This wake region is more-or-less "wedge-shaped" (or cone-shaped, depending on the spacecraft geometry). If the ratio of spacecraft size to (electron) Debye length is large enough, this unbalanced space charge is believed to produce a potential minimum downstream of the spacecraft. The existence of such a minimum has been predicted by many authors including Maslennikov and Sigov (1965, 1967, 1969), Maslennikov et al (1968), Taylor (1967), Kiel et al (1968), Call (1969, Figs. 3.1-3.3, 3.14, 3.21, and 3.23), Gurevich et al (1970), and Vaglio-Laurin and Miller (1970). These papers are part of an extensive literature on wakes of spacecraft in low Earth orbit. Reviews of this literature have been

given by Brundin (1963), Gurevich et al (1970), Samir and Stone (1986), and Stone and Samir (1986).

In situations studied by the above-mentioned authors, the spacecraft is assumed to be conductive, and therefore its potential relative to space will "float" at a uniform value determined by total, rather than local, current balance. If the ambient electrons are cold ($kT_e \sim 0.1$ eV), then this floating potential will be a few tenths of a volt negative with respect to space. The resulting potential distribution downstream of the spacecraft has the general appearance shown in Fig. 4.1(a).

We now consider situations which will arise during polar-orbit flights planned for the Shuttle Orbiter. Such situations will differ from the one just described in two important ways. First, the Orbiter's surface is mostly dielectric rather than conductive. Second, the auroral-zone ambient plasma often contains a high-energy "hot" electron constituent whose equivalent kinetic temperature is generally in the range 1 - 15 keV (Gussenhoven et al, 1985; Yeh and Gussenhoven, 1987).

In such situations, each small dielectric portion of the spacecraft's total surface will float separately at a potential determined by local rather than total

current balance. If enough hot auroral electrons are present, the situation shown in Fig. 4.1(a) will no longer be able to maintain itself. To see why, we note that the negative potentials present in the wake will exclude the cold electron population from it almost completely, so the hot electrons will form almost its entire population. The potential at the minimum shown in Fig. 4.1(a) will then be more negative than the potentials on adjacent surfaces by an amount which is much larger than the average emission energies of either secondary electrons or photoelectrons. The resulting potential barrier will therefore reflect these electrons and cause them to return to these surfaces at locations generally close to their emission points. As a result, the secondary-emission or photoemission current contributions will become unavailable as a means of discharging these surfaces, which will then charge progressively more negatively until surface potentials "just inside" the potential minimum have become almost as negative as at the minimum. A finite fraction of the emitted secondaries and photoelectrons will now escape, and these surfaces will now arrive at a steady-state "floating" condition. We shall see later (Sec. 4.4) that on a large enough spacecraft, surface potentials more than 100 volts negative with respect to space can be expected because of this mechanism. In the remainder of this Section, we discuss some other features of it.

One such feature, which is characteristic of it, is that the location of the potential minimum will migrate inward until it almost reaches the spacecraft. The general appearance of the equipotential surfaces downstream of the spacecraft will then be as shown in Fig. 4.1b.

A similar phenomenon, which often controls the high-voltage differential charging of geosynchronous-altitude satellites, is called the "barrier effect". This effect was first predicted by Fahleson (1973) and observed by Whipple (1976). It was then rediscovered independently in a numerical simulation by Katz et al (1979). It has also been studied by numerous other authors (Prokopenko and Laframboise, 1977, 1980; Laframboise and Prokopenko, 1977; Besse and Rubin, 1980; Olsen et al, 1981; Purvis, 1982; Katz and Mandell, 1982; Laframboise et al, 1982; Olsen and Purvis, 1983). However, two features of the present situation are very different than in the geosynchronous-altitude situation. In that situation, the Debye length of the ambient plasma was much larger than the spacecraft, and therefore the barrier could not be produced by space-charge effects. Barrier formation then occurred, over some part of the spacecraft surface, because another part of it had become charged to a much larger negative potential. For this to occur, the other part had to have a secondary-electron yield less than unity (for the existing incident electron distribution) and also had to be shaded, so that neither secondary-electron

emission nor photoemission could discharge it. In our situation, there is no requirement that a larger-potential surface exist somewhere else, and the barrier effect, instead of limiting the differential charging, actually produces it. Secondly, in the geosynchronous-altitude situation, the barrier effect is characterized by a saddle point in the potential outside the spacecraft, and as the surfaces inside the barrier charge more and more negatively, the saddle point migrates closer and closer to the spacecraft until it almost reaches it, and the potential difference between the saddle point and the surface adjacent to it decreases to a few volts, permitting a significant fraction of the emitted electrons to escape. In our situation, there is no saddle point. Instead, as mentioned above, there is a minimum in the potential outside the spacecraft, and as the surfaces inside the barrier charge more and more negatively, this minimum migrates almost to the surface [Fig. 4.1(b)]. More specifically, the entire surface-potential distribution must adjust itself until a "ridge", having an almost uniform (negative) "height" comparable to the emitted-electron mean energy, has formed outside the surface. Since this mean energy is only a few eV, this "ridge" will form close to the surface [Fig. 4.1(b)]. We see that a good estimate of the largest (negative) value of surface potential is given simply by the largest value of potential in the wake.

We now develop theory for calculating what values of surface potential will be achieved by this mechanism, as a function of spacecraft size and ambient plasma conditions. This is done in the next Section.

4.3. SURFACE-POTENTIAL. CALCULATION

We wish to develop a method of estimating the largest (negative) value of surface potential relative to space, as a function of position on the spacecraft's wake-region surfaces. In order to do this, we make a set of approximations which permit relatively simple, partly analytic solutions for this potential, while retaining the most important physical features of the problem. Such a procedure is especially valuable in view of the complexity of an exact treatment (Section 4.4; Section 5). These approximations are as follows.

As mentioned in Section 4.2, we assume that the most negative potential in the wake region just downstream of the spacecraft is a good approximation to the most negative potential on the spacecraft.

We assume that the spacecraft is an infinite cylinder. However, for most of our purposes, its detailed shape will not be important; its most important dimension will be its least dimension transverse to its motion. We assume that its surface is made of dielectric material, and it is immersed in a collisionless plasma crossflow which has a transverse drift velocity $U = 8$ km/sec relative to the spacecraft, corresponding to the speed of low Earth orbit. The ions in the plasma are assumed to be O^+ at a temperature of 0.1 eV. Their most-probable thermal speed $(2kT_i/m_i)^{1/2}$ is then 1.09 km/sec, and this is much less than U ,

so we can expect the wake to extend for many spacecraft diameters in the downstream direction (Fig. 4.1a). The electrons in the plasma are assumed to include a "cold" (0.1 eV) and a "hot" (1 keV or more) Maxwellian constituent, representing auroral plasma conditions. This is a very rough approximation to observed auroral-electron velocity distributions, which can be both very non-Maxwellian and very anisotropic (Sec. 4.2), but it is adequate for our purposes.

We ignore magnetic-field effects on charged-particle motions. This approximation should be acceptable for our purposes because the average gyroradii of the hot electrons and the ions are a few meters or larger, especially in a high-voltage wake region, and the cold electrons are almost completely excluded from the same region. Furthermore, collection of cold electrons by a negatively-charged spacecraft is very small, and therefore their density is well-approximated by a Boltzmann factor, independently of magnetic-field effects.

We assume that the rotation rate of the spacecraft is slow enough that transfer of surface charge into the spacecraft's wake region by rotation ("spin charging"; Parks and Katz, 1983) is negligible.

Our most severe approximations concern the ion-density distribution in the spacecraft wake. Exact calculations of these distributions are very difficult (Sec. 4.4; Sec. 5). We assume that the large-voltage region of the spacecraft's

wake is sufficiently elongated that variations in potential parallel to the wake axis (the x axis in Figure 4.1) are negligible in comparison with variations perpendicular to the same axis. This allows us to write a one-dimensional Poisson equation for potentials in this region. We further assume that outside this region, the potential ϕ is equal to space potential, which we take as our zero, and the ion and electron number densities n_i and n_e are equal. We assume that the cold-electron density decreases abruptly to zero at the edges of this region, so that the only electrons inside it are the hot ones. We ignore, for now, the effect of electron collection by the spacecraft on the space-charge density of the hot electrons, and we also ignore the density contribution made by the emitted electrons, whether these return to the surface or escape. We make an approximate correction for these two effects later. With our other approximations, these imply that the electron density in this region is given by a Boltzmann factor. We assume that the ion density in the same region is either zero (in the crudest approximation) or has a uniform value which we estimate later in this Section using a model-potential calculation (in the next approximation).

With these approximations, Poisson's equation in the large-voltage wake region (the "wake potential well") becomes:

$$\frac{d^2\phi}{dy^2} = \frac{n_{\infty eh} e}{\epsilon_0} \exp\left(\frac{e\phi}{kT_{eh}}\right) \quad (4.1)$$

where y is distance perpendicular to the wake centerline (Fig. 4.1), T_{eh} and $n_{\infty eh}$ are the temperature and ambient number density of the hot electron constituent, e is the magnitude of unit electronic charge, ϵ_0 is the permittivity of space, and k is Boltzmann's constant. Boundary conditions on the potential are:

$$\phi = 0 \text{ when } y = \pm y_{\max} \quad (4.2)$$

where y_{\max} is the half-width of the wake potential well just downstream of the spacecraft. Using symmetry, we have:

$$\phi = \phi_0 < 0, \quad \frac{d\phi}{dy} = 0 \text{ when } y = 0. \quad (4.3)$$

By our assumptions, y_{\max} is just the spacecraft radius r_s . We discuss later how to obtain an "improved" value for y_{\max} .

We define the following dimensionless variables:

$$\begin{aligned} \xi &= y/\lambda_{Deh} = y/(\epsilon_0 k T_{eh} / e^2 n_{\infty eh})^{\frac{1}{2}} \\ \Psi &= -e\phi/kT_{eh} \end{aligned} \quad (4.4)$$

where λ_{Deh} is the hot-electron Debye length. Equations (4.1) - (4.3) then become:

$$d^2 \Psi / d\xi^2 = - \exp (-\Psi) \quad (4.5)$$

$$\Psi = 0 \text{ when } \xi = \pm \xi_{\max} \quad (4.6)$$

$$\Psi = \Psi_0 > 0, d\Psi/d\xi = 0 \text{ when } \xi = 0 \quad (4.7)$$

Equation (4.5) is nonlinear, but it can be solved by multiplying both sides by $2 d\Psi/d\xi$ and noting that its left side then equals $(d/d\xi)(d\Psi/d\xi)^2$. Its solution subject to Eq. (4.7) then is:

$$\xi = \pm [2 \exp(\Psi_0)]^{\frac{1}{2}} \text{Arctan} [\exp(\Psi_0 - \Psi) - 1]^{\frac{1}{2}} \quad (4.8)$$

Using (4.6) now gives us, in implicit form, the desired relation between the normalized wake half-width ξ_{\max} and the normalized largest negative wake potential Ψ_0 , as follows:

$$\xi_{\max} = [2 \exp(\Psi_0)]^{\frac{1}{2}} \text{Arctan} [\exp(\Psi_0) - 1]^{\frac{1}{2}} \quad (4.9)$$

For various values of ξ_{\max} , the solid curves labeled "0" in Fig. 4.2 show Ψ as a function of the normalized transverse distance ξ from the wake centerline in the wake potential well, as given by Eq. (4.8). For narrow wakes (small ξ_{\max} and Ψ_0), the potential variation across the wake is nearly parabolic, but for wakes whose width is many hot-electron Debye lengths, the decrease in electron density in the wake produces an increase in local Debye length, with a consequent "flattening" of the potential profile in the well, and a slowing-down of the rate of increase of well depth Ψ_0 , from a limiting dependence of the form:

$$\Psi_0 \rightarrow \frac{1}{2} \xi_{\max}^2 \quad \text{for small } \xi_{\max} \quad (4.10)$$

to:

$$\Psi_0 \rightarrow \ln(2 \xi_{\max}^2 / \pi^2) \quad \text{for large } \xi_{\max} \quad (4.11)$$

The dependence of Ψ_0 on ξ_{\max} given by Eq. (4.9) is plotted as the uppermost solid curve, labeled "0", in Fig. 4.3. Equations (4.10) and (4.11) are plotted in Fig. 4.3 as dotted curves. Again, Ψ_0 will be almost equal to the largest normalized negative surface potential Ψ on the spacecraft.

Equation (4.10) is equivalent to:

$$\phi_0 \rightarrow -\gamma_{\max}^2 e n_{\infty h} / 2\epsilon_0 \quad (4.12)$$

and Eq. (4.12) indicates that for potentials small compared with the hot-electron temperature, the potential produced by the wake-induced-barrier mechanism depends only on the ambient density, and not the temperature, of the hot electrons.

The most important approximation in our calculation so far is the omission of ion density in Eq. (4.1). We now estimate the effects of including ion density. If n_{wl} is ion density in the wake, including it would result in replacement of Eq. (4.5) by:

$$\frac{d^2\Psi}{d\xi^2} = \frac{n_{wi}}{n_{\infty eh}} - e^{-\Psi} \quad (4.13)$$

If n_{wi} were *uniform*, it could never be large enough (for a given Ψ) to reverse the sign of $d^2\Psi/d\xi^2$, because the solutions of (4.13) would then become unphysical. Therefore, such a density contribution could produce only a further "flattening" of the wake potential profiles, and a limiting of Ψ to values less than that at which this sign-reversal would occur, i.e:

$$\Psi < \Psi_n \equiv \ln (n_{\infty eh}/n_{wi}) \quad (4.14)$$

We have solved Eq. (4.13) numerically for various values of ξ_{max} and $n_{wi}/n_{\infty eh}$. The computer program used for doing this is listed in Appendix B. Resulting wake potential profiles are shown as dotted curves in Fig. 4.2. Figure 4.3 shows, for various values of $n_{wi}/n_{\infty eh}$, the resulting dependences of Ψ_0 on ξ_{max} . The effects noted following Eq. (4.13) are clearly evident in these Figures. Equations (4.11) and (4.14) are similar to Eqs. (2) and (4a), respectively, of Vaglio-Laurin and Miller (1970), but our application here is to much larger wake potentials than theirs.

We now introduce an approximate correction for effects on electron density arising from emitted-electron space charge and ambient-electron collection by the spacecraft. In order to do this, we ignore magnetic-field effects on electron motion across the barrier, and we assume that in some region surrounding a

point on the barrier, the potential distribution has planar symmetry. We follow the usual procedure of approximating the emitted-electron velocity distribution, in both speed and direction, by a Maxwellian (Sec. 4.1). The velocity distributions of ambient and emitted electrons at the barrier are then half-Maxwellians directed toward and away from the spacecraft, respectively. If we also ignore "hopping-conduction" currents of emitted electrons along the spacecraft surfaces inside the barrier, then the inward and outward fluxes carried by these distributions must be equal. Since the emitted electrons have a much smaller average velocity than the ambient ones, their space-charge density in the region of the barrier must be much larger. This constitutes a major increase in wake-region electron density, and we shall see later (Sections 4.4 and 4.5) that it greatly increases predicted wake-region negative surface potentials. If ϕ_b is local barrier potential and T_s is the temperature of secondary electrons or photoelectrons emitted from the surface, then with the above-mentioned approximations, the total electron density at locations outside the barrier is:

$$\begin{aligned}
 n_e(\phi) = n_{\infty eh} & \left[\frac{1}{2} \left(\frac{T_{eh}}{T_s} \right)^{\frac{1}{2}} \exp \left[\frac{e\phi_b}{kT_{eh}} + \frac{e(\phi - \phi_b)}{kT_s} \right] \operatorname{erfc} \left[\frac{e(\phi - \phi_b)}{kT_s} \right]^{\frac{1}{2}} \right. \\
 & \left. + \exp \left(\frac{e\phi}{kT_{eh}} \right) \left\{ 1 - \frac{1}{2} \operatorname{erfc} \left[\frac{e(\phi - \phi_b)}{kT_{eh}} \right]^{\frac{1}{2}} \right\} \right] \quad (4.15)
 \end{aligned}$$

where $\text{erfc}(x) \equiv 1 - \text{erf}(x)$ is the complementary error function. At the barrier, Eq. (4.15) reduces to:

$$n_e(\phi_b) = n_{\infty eh} \exp \left[\frac{e\phi_b}{kT_{eh}} \right] \left[\frac{1}{2} + \frac{1}{2} \left(\frac{T_{eh}}{T_s} \right)^{\frac{1}{2}} \right] \quad (4.16)$$

The last factor in Eq. (4.16) constitutes a correction factor for the electron density in Eqs. (4.1) - (4.14), at locations close enough to that of the barrier (Fig. 4.1b). Since the direction of the y -coordinate in Eqs. (4.1) - (4.13) is more-or-less aligned with that of the barrier, we shall use this correction factor as a uniform multiplicative constant to be applied to the ambient density $n_{\infty eh}$ wherever appropriate in applications (Sections 4.4 and 4.5).

The accuracy of this procedure is not immediately clear. As one moves outward from the barrier, ϕ becomes less negative than ϕ_b , and the emitted-electron contribution, which is the dominant contribution to n_e near the barrier in Eq. (4.15), decreases rapidly. As a result, it becomes less clear than before whether the approximation $|\partial^2\phi/\partial x^2| \ll |\partial^2\phi/\partial y^2|$, which underlies the analysis presented in Eqs. (4.1) - (4.13), is valid. If it is not, then $|\partial^2\phi/\partial y^2|$, and therefore $|\phi|$, are overestimated by this procedure. One should therefore regard the last factor in Eq. (4.16) as an upper bound on the true correction to ϕ resulting from emitted-electron space charge. In representing the emitted

electrons as Maxwellian, we have ignored the fact that the velocity distribution of backscattered electrons is more poorly approximated by a Maxwellian and also has a much larger average energy than those of either secondary electrons or photoelectrons (Sternglass, 1954, Fig. 8). However, at the incident-electron energies of importance in our applications (Sections 4.4 and 4.5), backscattered electrons make a relatively minor contribution to the total emitted flux.

In order to estimate Ψ_0 using the results presented in Eqs. (4.8) - (4.16) and Figs. 4.2 and 4.3, we now need to develop a way of estimating the ratio $n_{wi}/n_{\infty eh}$ in Eqs. (4.13) and (4.14). Calculation of a realistic distribution for ion density in a spacecraft wake, in the presence of ion-drift and space-charge effects, is a task of great difficulty (Sec. 4.4; Sec 5). A very simple approximation is the "neutral approximation" in which electric-field effects on particle motion are ignored. For a plasma having ion speed ratio $S_i = U/(2kT_i/m_i)^{1/2}$, this approximation readily yields the result:

$$n_i/n_{i\infty} = \pi^{-1/2} \int_{-\infty}^{-S_i \cos \theta} e^{-u^2} du = \frac{1}{2} \left[1 - \operatorname{erf} (S_i \cos \theta) \right] \quad (4.17)$$

[see, for example, Parks and Katz, 1983, Eq. (27)], for ion density on a convex surface, where θ is the angle between the surface normal and the downstream direction. Because this result ignores the curvature of ion orbits caused by

electric fields, it grossly underestimates ion density on (or near) downstream-facing surfaces.

To obtain a better estimate, we use a method similar but not identical to that of Parks and Katz (1983, Sec. 4; 1985). Here, we specifically assume that the spacecraft is an infinite circular cylinder whose axis is perpendicular to the ion drift direction. We assume that ions arriving at the downstream axial surface point ($r=r_s$, $\theta = 0$ in Fig. 4.1) have moved through a potential distribution which has the form:

$$\phi(r, \theta) = g(\theta)/r^2 \quad (4.18)$$

where:

$$g(\theta) = \begin{cases} r_s^2 \phi_0 (1 - 4\theta^2/\pi^2), & \text{for } |\theta| < \pi/2 \\ 0 & \text{otherwise} \end{cases} \quad (4.19)$$

and ϕ_0 is the potential at ($r = r_s$, $\theta = 0$). As in Eq. (4.3), we have $\phi_0 < 0$. This choice for the potential is different than that of Parks and Katz (1983, Eq. 40; 1985, Eq. 14). It is a special case of the form $\phi(r, \theta) = f(r) + g(\theta)/r^2$, and for potentials of this form, the quantity:

$$C \equiv \frac{1}{2} L^2 + m q g(\theta) \quad (4.20)$$

is a constant of particle motion (Goldstein, 1980, pp. 454-457). Here, m and q are ion mass and charge, and $L = mrv_\theta$ is ion angular momentum in the (r, θ) plane. For the potential given by Eqs. (4.18) and (4.19), this feature permits ion orbits arriving at $(r = r_s, \theta = 0)$ to be integrated analytically. The density at this point is then given by a velocity-space integral whose integrand is known analytically. The integral itself must be evaluated numerically. Details are given in Appendix C. The computer program used for doing this calculation is listed in Appendix D. In contrast with the density integration of Parks and Katz (1983, 1985), ours does not involve an inequality (Parks and Katz, 1983, Eqs. 28-31, or 1985, Eqs. 2-5). The potential given by (4.18) and (4.19) is not the same as the one given by Eqs. (4.1-4.14), but this is not surprising since our treatment is not self-consistent. As we point out in Sections 4.4 and 5, a self-consistent treatment of our problem is a task of great difficulty, and our approximate treatment serves the purpose of providing a simple estimate of wake potentials. In the potential given by Eqs. (4.18-4.19), some ion orbits have angular turning-points (Appendix C and Fig. 4.4). Figure 4.5 shows normalized ion densities $\eta_1 = n_1/n_{1\infty}$ at the downbeam surface point ($r = r_s, \theta = 0$), in the presence of this potential, calculated as described in Appendices C and D. These values can be used to estimate the ratio n_{wi}/n_{weh} in Eqs. (4.13) and (4.14).

For completeness, we also develop a rough correction of the normalized wake half-width $\xi_{\max} = y_{\max}/\lambda_{\text{Deh}}$ for effects of finite speed ratio. We do this for the two geometries shown in Fig. 4.6. In terms of these geometries, we do this by using the distance BC, rather than the spacecraft radius or half-width $OA \equiv r_s$, for y_{\max} . We assume that the wake edge AD is straight (see Sec. 4.4) and has a slope of $-1/S_i$. The geometries of Figs. 4.6(a) and (b) then imply the results:

$$y_{\max} = r_s \left[1 - (1 + S_i^2)^{-\frac{1}{2}} \right] \quad (4.21)$$

for a cylinder or sphere, and:

$$y_{\max} = r_s (1 + 1/S_i^2)^{-\frac{1}{2}} \quad (4.22)$$

for a thin disk or plate normal to the ion drift direction. This derivation implies that in Eqs. (4.1) - (4.13) only, the y-coordinate is most usefully regarded as distance from B along the line BC in Fig. 4.6(a) or (b). As long as O^+ at $T_i \approx 0.1$ eV is the dominant ionic constituent, S_i is large enough that the corrections given by (4.21) or (4.22) are unimportant (Sec. 4.4).

This completes the development of our method for estimating the potential ϕ_0 at the downstream point $(r, \theta) = (r_s, 0)$. In Sections 4.4 and 4.5, we apply this method to wake-induced-barrier-effect charging of the Shuttle Orbiter and of hypothetical future spacecraft of larger size.

4.4. APPLICATIONS TO LOW-POLAR-ORBIT SPACECRAFT CHARGING; DISCUSSION

We examine first the charging of the Shuttle Orbiter in the auroral plasma. Our primary goal is to find out if there exist auroral-electron energy distributions which are not energetic enough to cause high-voltage charging by overcoming secondary-electron and backscattered-electron emission by spacecraft surfaces, but which can cause it via the wake-induced-barrier mechanism. The range of auroral-electron equivalent temperatures implied by these criteria is from a few hundred eV to a few keV, with the upper end of this range being strongly dependent on the secondary and backscattered emission properties of the surface material involved (Sec. 4.1). Within this range, the most important remaining criterion is a small enough auroral-electron Debye length, which implies a large enough auroral-electron density.

The best data available on energy distributions of auroral electrons are those of Gussenhoven et al (1985) and Yeh and Gussenhoven (1987), obtained using the DMSP F6 and F7 satellites. Gussenhoven et al (1985, Fig. 11) present Maxwellian fits to the higher-energy (above a few keV) portions of three electron energy distributions observed during a high-voltage charging event on DMSP F7. These fits yield $n_{\infty eh} = 3.9, 3.2, \text{ and } 4.9 \text{ cm}^{-3}$ and $kT_{eh} = 10.1, 14.4, \text{ and } 4.2$

keV, resulting in λ_{Deh} values of 378, 499, and 218 m, respectively. For secondary electrons having emission temperature $T_s = 3$ eV, applying the density-correction factor $\frac{1}{2} + \frac{1}{2} (T_{\text{eh}}/T_s)^{\frac{1}{2}}$ from Eq. (4.16) gives decreased λ_{Deh} values, respectively, of 70, 84, and 50 m. The appropriate value of r_s for the Shuttle Orbiter depends on its orientation. Its fuselage radius is roughly 3m. Its largest wake half-width will be produced when its wing plane is perpendicular to its motion. The largest circle which can be inscribed inside its cross-section in this plane has a radius of 7.5m. The Orbiter's projected dielectric area in the same plane is equivalent to that of a circular disk of radius 11.5 m. All of these dimensions are much smaller than the Debye-length values listed above. Equation (4.9) or the uppermost curve in Fig. 4.3 now indicates that the wake-induced-barrier mechanism will induce potentials of only a few volts negative, or, with the density-corrected λ_{Deh} values noted above, a few tens of volts negative. The largest such value is $\phi_0 = -111$ V, corresponding to $kT_{\text{eh}} = 4.2$ keV, $\lambda_{\text{Deh}} = 50$ m, and $r_s = 11.5$ m. Evidently, smaller values of λ_{Deh} , corresponding to greater electron densities (Eq. 4.12), are required for a reliable indication of high-voltage charging by this mechanism.

Yeh and Gussenhoven (1987, Tables 2a-c and Figs. 1-2) present a larger variety of auroral-zone electron-energy distributions. Among these, two result

in Debye-length values much smaller than the others. These are the "Type-1 spectra" given in their Table 2a. They give two such spectra. These are averages of spectra which produced negative DMSP spacecraft potentials $-\phi_s$ greater than 100V and in the range from 30V to 70V, respectively. Each of these is represented by two different Maxwellian fits below and above a transition energy of 12.16 and 11.34 keV, respectively. For the first spectrum, the parameters characterizing the two Maxwellian fits are $n_{e1} = 58.30 \text{ cm}^{-3}$, $kT_{e1} = 1.31 \text{ keV}$, $n_{e2} = 1.23 \text{ cm}^{-3}$ and $kT_{e2} = 5.49 \text{ keV}$. For the second, these parameters are $n_{e1} = 46.88 \text{ cm}^{-3}$, $kT_{e1} = 1.14 \text{ keV}$, $n_{e2} = 0.08 \text{ cm}^{-3}$, and $kT_{e2} = 5.68 \text{ keV}$. The most important difference between these two spectra is that the density of the hotter Maxwellian is much larger in the first one. As the authors point out, this is consistent with the idea that the higher-energy electrons produce combined secondary and backscattered yields less than unity and are therefore responsible for the high-voltage charging. The Debye lengths λ_{Deh} for these two spectra are 35.2 m and 36.7 m, respectively, based on the lower-energy Maxwellian fit; the presence of the higher-energy Maxwellian has negligible effect on these values. These values are close to the smallest hot-electron Debye lengths which are likely to be encountered in the auroral zones (M.S. Gussenhoven, private communication, 1987). The analysis which follows is therefore based on the lower energy component of the first spectrum.

For $\lambda_{\text{Deh}} = 35.2$ m and the approximate Shuttle Orbiter wake half-widths of 7.5 m and 11.5 m, mentioned above, we obtain, using either Eq. (4.10) or the uppermost curve in Fig. 4.3, the surface potentials $\phi_0 = -29.7$ V and -70.3 V. Again using Eq. (4.9) with the density-correction factor from Eq. (4.16) and $T_s = 3\text{eV}$, we obtain $\lambda_{\text{Deh}} = 10.7\text{m}$ and the surface potentials $\phi_0 = -273\text{V}$ and -544V .

The variation among these four surface-potential values is rather large, but their geometric mean is -133V , so if we take this as the most realistic prediction obtainable using our analysis, we have a result which fulfils the definition of "high-voltage" charging as given in Sec. 1. It therefore appears that the Shuttle Orbiter is large enough to undergo high-voltage charging caused by the wake-induced-barrier mechanism, at least for some combinations of spacecraft orientations and known environmental conditions. For the same conditions, the same methods predict that in order to achieve $\phi_0 = -100\text{V}$ without invoking the density correction from Eq. (4.16), a spacecraft half-width of 14m is required, and this is only moderately larger than the Shuttle Orbiter. For a spacecraft half-width of 60m, the corresponding calculation gives $\phi_0 = -1000\text{V}$; however, this latter result is affected strongly by ion-density effects, and we discuss these later in this Section.

One consequence of this charging is particularly noteworthy. Suppose that the downstream-facing surfaces of a spacecraft are mostly dielectric, but somewhere near the center of the downstream surface region is a small area of exposed conductor which is grounded to the spacecraft frame, and this in turn is grounded to exposed conductive surfaces which are not in the wake and therefore are exposed to the full ram flux of upstream ions, so that these surfaces will float close to space potential. Evidently, the region around the edges of the exposed downstream conductor will then be subjected to high electrical stresses, producing a prime location for unwanted electrical discharges. A conductive surface on an experiment package in the Orbiter's cargo bay is an example of such a situation.

In the above derivation of spacecraft potentials, our most important approximation was the neglect of the ion space-charge density in the wake. The derivation in Sec. 4.3 and Appendix C gives us the means to estimate this quantity. In order to do this, we assume that the ambient plasma has a maximum total ion or electron density n_{oe} between $10^5/\text{cm}^3$ and $5 \times 10^5/\text{cm}^3$ in the Shuttle altitude range (Narcisi, 1973; Samir et al, 1981, Fig. 7; Swider, 1985, Figs. 21-90 and 21-91). The data presented by Rich (1983, Fig. 3) indicate a wider range of possible values. We assume that the cold-ion constituent has a temperature of 0.1 eV. We further assume that these ions are

either O^+ or H^+ and that a 1 keV hot-ion constituent may or may not be present. For a spacecraft orbital speed of 8 km/sec, and for O^+ at 0.1 eV, H^+ at 0.1 eV, O^+ at 1 keV, and H^+ at 1 keV, the ion speed ratio S_i has values of 7.31, 1.83, 0.0731, and 0.0183, respectively; the last two of these are effectively zero. In calculating the above-mentioned spacecraft potentials, we used a hot-electron ambient density value $n_{\infty eh}$ of 58.3 cm^{-3} . This is smaller than the above-mentioned total $n_{\infty e}$ values by factors of 1.7×10^3 and 8.6×10^3 , respectively. In order that our predicted spacecraft potentials not be greatly decreased by effects of ion space-charge, the ion density n_{wi} in the wake must be reduced below ambient by an even larger factor, say 10^5 . We now see from Fig. 4.5 that for $S_i = 7.31$, such a reduction requires $-\chi_0 = -e\phi_0/kT_i < \text{about } 1000$, i.e., $-\phi_0 < \text{about } 100 \text{ V}$. For larger values of $-\phi_0$, ion-density effects will begin to alter the value of ϕ_0 significantly. Using the same $n_{\infty e}$ values together with Eq. (4.14) and Fig. 4.5, we obtain limiting ϕ_0 values of -311 V and -198 V , respectively, in the limit of large spacecraft size. If we again use the density-correction factor from Eq. (4.16) with $T_s = 3 \text{ eV}$, these ϕ_0 values increase to -727 V and -395 V , respectively.

If any substantial fraction of H^+ is present, or any substantial ion fraction having $T_i \sim 1 \text{ keV}$, then Figs. 4.2-4.5 indicate that these ions will suppress wake-induced-barrier-effect charging.

At 300 km altitude, measured midlatitude H^+ concentration values of $64/\text{cm}^3$ and $2.0 \times 10^3/\text{cm}^3$ are given by Narcisi (1973, Figs. 5 and 6); see also Swider (1985, Figs. 21-90 and 21-91). Two measurements of $2.8 \times 10^2/\text{cm}^3$ at 300 km have been given by Samir et al (1981, Figs. 7a and 7b). A measurement close to this value has also been given by Rich (1983, Fig. 17). For the above-mentioned T_i and S_i values of 0.1 eV and 1.83, Fig. 4.5 indicates that the wake-point ion density at $\phi_0 = -100\text{V}$ is reduced below the ambient value by a factor of 4.3×10^{-2} . This gives wake-point H^+ concentrations of $2.8/\text{cm}^3$, $86/\text{cm}^3$, and $12/\text{cm}^3$, respectively. The first and third of these are substantially below the $n_{\infty eh}$ value of 58.3 cm^{-3} mentioned above, indicating that in these cases, not enough H^+ is present to suppress wake-induced charging. Furthermore, the same measurements show smaller H^+ concentrations at lower altitudes. Narcisi (1973) also presents data showing decreases in both O^+ and H^+ concentrations at auroral latitudes compared to midlatitudes. In addition, one does not necessarily find kilovolt ions when kilovolt electrons are present (M.S. Gussenhoven, private communication, 1987). Furthermore, the wake-point ion-density values displayed in Fig. 4.5 may be too large, for reasons discussed following Eq. (C17). For all these reasons, it therefore appears that the wake-induced-barrier mechanism can produce high-voltage charging on spacecraft at least as large as the Shuttle Orbiter.

The foregoing predictions involve considerable uncertainty. The most important causes of this are: (1) the lack of simultaneity of the above-mentioned measurements of $n_{\infty eh}$, n_{H^+} , and n_{O^+} , (2) the crudity of our correction for emitted-electron density, which involved the use of the last factor in Eq. (4.16) as a spatially-uniform factor, and (3) the crudity of our method for calculating the n_{wi} values presented in Fig. 4.5. The major source of crudity in item (3) is our assumption of a model potential [Eqs. (4.18) and (4.19)] which probably approximates the actual self-consistent potential distribution badly enough to produce important errors. To do better is a task of great computational difficulty. To calculate downstream-point surface potentials exactly requires knowing not just one value of ion density but rather the entire ion-density distribution around the spacecraft, and this is coupled with the entire potential distribution in a strongly nonlocal and nonlinear way through Poisson's equation and the particle dynamics. If most of the ions are O^+ at ~ 0.1 eV, the ambient ion velocity distribution is very anisotropic. The ram energy of an O^+ ion at 8 km/sec is about 4 eV, and ions entering a high-voltage wake are accelerated to kinetic energies much larger than this. The ion velocity distribution in such a wake will therefore be very "beam-like" and the resulting ion-density distribution is likely to be very sensitive to small changes in spacecraft geometry and external conditions, and also to small changes in the potential distribution of the

kind encountered in an iterative numerical calculation. The latter type of sensitivity may destabilize such a calculation. A numerical calculation by Laframboise and Parker (1987), of the surface-potential distribution on a nonemitting dielectric cylinder in a collisionless plasma crossflow containing a hot-electron constituent, illustrates many of these features. A description of their work also appears in Sec. 5. A more thorough investigation of the wake-induced-barrier effect will require numerical calculations in which all of these difficulties will be encountered.

4.5. APPLICATIONS TO BEAM-INDUCED SHUTTLE ORBITER CHARGING; DISCUSSION

Our second investigation concerns charging of the Shuttle Orbiter during electron-beam emission by the SEPAC Spacelab-1 experiment. Sasaki et al (1986) report that charging of the Orbiter due to beam emission was strongly dependent on the orientation of the Orbiter with respect to its velocity vector. For beam emission currents ≥ 100 mA, the Orbiter's frame potential was observed (see their Fig. 10) to reach the beam acceleration voltage when its cargo bay faced downstream, but not otherwise. Herein, we propose an explanation for this observation, based on the wake-induced-barrier mechanism. The basic premise is that if the "upper" side of the Orbiter faces downstream, then a large region of space surrounding the cargo bay will be depleted of ions. If the wake-induced-barrier mechanism then produces negative potentials on the Orbiter's upper wing surfaces and other wake-region dielectric surfaces, the region of positive potentials (the "potential well for electrons"), which must surround the exposed conductive surfaces associated with the SEPAC experiment in the cargo bay, will then be very constricted in spatial extent, and the process of electron return-current collection will be partly inhibited, requiring larger positive potentials on these surfaces in order to collect the electron current required for current balance.

In order to investigate this situation in detail, we use data presented by Taylor et al (1985). Plate 3 of their paper shows the response of the SEPAC energetic-electron analyzer during a time interval which included six pulses from the SEPAC electron gun. The duration of each pulse was 4 seconds. This time interval formed part of the SEPAC FO-2 experiment sequence, during which the Orbiter's cargo bay faced downstream. We analyze the electron spectrum measured during the second pulse, during which the electron beam current and emission energy were 70 mA and 5 keV. During this pulse, their Plate 3 shows a sharp peak near 1 kV in the spectrum measured by the energetic-electron analyzer, indicating Orbiter frame charging to that voltage. The same spectrum also shows, during all six pulses, an enhanced population of electrons up to the upper end of the detector range at 15 kV, i.e. well above beam energy. These electrons presumably were energized by a wave-particle interaction caused by the presence of the beam (Taylor et al, 1985). The population above 1 kV decreases monotonically with increasing energy.

We need to find out whether these energized electrons can produce a significant voltage on downstream-facing dielectric surfaces via the wake-induced-barrier mechanism. To do this, we must estimate their "ambient" density, i.e. that at space potential. We do the latter by fitting a Maxwellian

distribution to the above-mentioned spectrum. This spectrum shows energy-differential fluxes $\Phi = 6.31 \times 10^5$ and 1.585×10^5 electrons/cm² sec steradian eV at energies E of about 3.59 and 12.2 keV with respect to spacecraft frame potential, respectively. Assuming that these electrons have an isotropic velocity distribution, we have:

$$\frac{dJ_e}{dE} = \pi \Phi \quad (4.23)$$

and:

$$f_e = \frac{m_e^2}{2\pi E} \frac{dJ_e}{dE} \quad (4.24)$$

(Prokopenko and Laframboise, 1977, 1980), where dJ_{eo}/dE is the energy-differential flux onto one side of an arbitrarily-oriented surface element, and f_e is the electron velocity distribution function. By fitting a Maxwellian distribution of the form:

$$f_e = n_e \left[\frac{m_e}{2\pi kT_e} \right]^{3/2} \exp (-E/kT) \quad (4.25)$$

to the resulting values of f_e , we obtain $n_e = 18.6$ electrons/cm³ and $kT_e = 3.32$ keV. This is the value of n_e at spacecraft frame potential, so it must be multiplied by $\exp (-1.0/3.32)$ to obtain n_e at space potential. Doing this yields the "ambient" value $n_e = 13.8$ electrons/cm³. Again using Eq. (4.10) and our estimates of 7.5 and 11.5 m for Orbiter wake half-width, together with these values of n_e and kT_e , we obtain $\phi_0 = -7.0$ or -16.6 V, respectively, as estimates

for the wake-induced-barrier potential for this situation. Again using the electron-density correction factor from Eq. (4.16) with $kT_s = 3$ eV as in Sec. 4.4, we obtain $\phi_0 = -117$ or -266 V. As in Sec. 4.4, we propose the geometric mean of these four values, -43.6 V, as a rough "best guess" for the actual potential achieved. As in Sec. 4.4, these four estimates cover a large range of potentials. The smallest among them is not much larger than the potential difference of a few volts expected between the barrier and the surface potentials (Sec. 4.2), but they still serve to indicate that when the Orbiter's cargo bay faced downstream during the SEPAC experiment, the wake-induced-barrier mechanism probably caused at least marginally negative potentials to occur over most of the Orbiter's downstream-facing dielectric surfaces. The resulting steepening of the "potential well for electrons" around the SEPAC experiment would then restrict electron collection, by causing a breakdown of "orbit-limitation" of this collection (Mott-Smith and Langmuir, 1926; Laframboise and Parker, 1973) and this would force the spacecraft frame potential to become more positive in order to collect the required return current.

In contrast with this, one can readily infer that when the Orbiter's cargo bay and upper surfaces faced upstream rather than downstream, potentials on a larger portion of these surfaces would have been positive with respect to space, by amounts which increased with decreasing distance from the SEPAC electron

gun. To show this, we proceed as follows. Sasaki et al (1986) assume that the ambient plasma surrounding the Orbiter had a temperature of 1000 K and a density of $10^5/\text{cm}^3$. The corresponding random electron flux is 0.79 mA/m^2 . In comparison, the random flux for the Maxwellian parameters calculated just above is 0.02 mA/m^2 , and this is very much smaller. In cases where the cargo bay faced upstream, densities of ambient ions near it would be much larger, and the wake-induced potential barrier would be absent. Using the backscattered-electron and secondary-electron yield data for fused silica, the Shuttle dielectric surface material, given by Prokopenko and Laframboise [1980, Eq. (9)], Laframboise et al (1982, Table 1), and Yeh and Gussenhoven (1987, Fig. 3, rescaled for fused silica), we obtain that the total emitted-electron flux exceeds the incident-electron flux for incident-electron energies from 40 eV to 23.3 keV. Therefore, the impingement of monoenergetic electrons anywhere in this energy range constitutes a net positive rather than negative current, and if no other current sources were present, this current would drive a surface exposed to it to a positive potential large enough that the beam would impact at a kinetic energy of 23.3 keV; this energy is called the "second crossing" of the emission yield curve for this material (Leung et al, 1981).

For a beam emitted at 5kV with respect to spacecraft ground, this implies that dielectric surfaces exposed to it would float at 18.3 kV with respect to

spacecraft ground, assuming that: (a) it remained nearly-enough monoenergetic, (b) its impacting current density on surfaces close to space potential were enough to overcome the negative current density from the low-energy ambient electrons, and (c) the emitted electrons all or almost all escaped. If these dielectric surfaces thereby became the most positively-charged locations on the spacecraft, assumption (c) would be violated, since emitted electrons generally tend to migrate to the most positive electrode available, and this would prevent dielectric surfaces from acquiring voltages much more positive than those of the exposed conductors. These would be at spacecraft frame potential, which would be between 0 and 5 kV positive with respect to space.

To find out if returning beam fluxes can ever overcome the cold-electron ambient flux, we note that the largest electron current emitted by the SEPAC gun was 300 mA. If all of this current were to return and impact uniformly over an area equal to the Orbiter's projected wing-plane cross-section of 418 m², the resulting electron flux would then be 0.72 mA/m², and this is close to the cold-electron random flux value of 0.79 mA/m² noted above. Because ambient-electron current is also present, not all of the beam current will return, even when the spacecraft frame is charged to beam voltage, but the returning beam current is likely to be more concentrated at smaller distances from the SEPAC experiment, so this comparison suggests that a relatively

extended neighborhood of the SEPAC experiment existed within which dielectric surfaces charged to positive voltages close to the beam emission voltage, at times when the cargo bay was exposed to ambient upstream ions. The resulting enlargement of the positive-potential region surrounding the SEPAC experiment should then have permitted easier beam-current return to the spacecraft frame, thereby tending to prevent the spacecraft frame from charging to the beam emission voltage, and this appears to support our explanation, proposed herein, of the SEPAC observations of spacecraft-frame voltages. The edges of this region might be expected to fluctuate considerably, and this may explain some of the time-dependence reported in the observations of Taylor et al (1985) and Sasaki et al (1986).

It might be expected also that when the cargo bay faced upstream, the resulting increase in the density of both ambient ions and electrons near it would increase the tendency of the beam to be scattered by beam-plasma instabilities near the Orbiter, and this would further facilitate beam-current return. However, no such tendency is apparent when one compares the electron spectra shown in Plate 3 (cargo bay facing downstream) and Plate 4 (cargo bay facing upstream) of Taylor et al (1985).

5. PRELIMINARY RESULTS FROM A NUMERICAL LOW-POLAR-ORBIT CHARGING SIMULATION

The simple treatment developed in Sec. 2 led to a suggestion that the onset of high-voltage charging in low polar orbit can be expected to depend primarily on the ratio R of the hot-electron ambient flux to the ambient flux of all ions. In this Section we present preliminary results from numerical simulation work whose initial goal was to verify this suggestion. This work uses an adaptation of a previously-existing simulation program written by one of us (Parker, 1983) for an infinite cylindrical spacecraft geometry in a collisionless plasma crossflow. If the spacecraft surface is entirely dielectric, then at progressively increasing values of R , one might expect surfaces in the spacecraft wake to be the first to undergo high-voltage charging, followed by sideways-facing and finally frontward-facing surfaces, as shown schematically in Fig. 5.1. The numerical results show that at least one implied feature of Fig. 5.1, namely the apparent monotonic progression to larger negative voltages as one moves around the surface of the cylinder toward the wake point, is wrong; we will return to this question later.

Our simulation geometry is shown in Fig. 5.2. Our original intention was to model a completely dielectric cylinder, but we have substituted a set of electrically isolated conductive sectors in the wake region because we found that strong ion focusing effects occurred in the wake, and these produced very localized ion-current deposition regions or "ion hot spots", whose location was very sensitive to small variations which occurred in the sheath potential distribution as iteration proceeded toward a self-consistent set of sheath boundary values. Averaging these ion currents over the 10° or 20° intervals shown in Fig. 5.2 suppressed the resulting instabilities and allowed the iterative procedure to converge. The parameter values chosen for this

study included: Debye length λ_D /spacecraft radius $r_s = 0.001$, ion speed ratio S_i ($=$ drift speed U /ion most-probable thermal speed $\sqrt{2kT_i/m_i}$) $= 8$, ions O^+ at a temperature of 0.2 eV, cold electrons at 0.2 eV, and hot (auroral) electrons at 5 keV. We have again made the assumptions (1), (2), and (3) listed in Section 2.

The finite-element discretization used for position space is indicated in Figs. 5.2 and 5.3. "Inside-out" ion orbit-following was used for calculating ion surface-current densities. The ion velocity-space discretization used was similar to that described by Parker (1977). To achieve sufficient accuracy in ion flux values at wake-side surface points required use of 1024 incident ion directions at each of 32 ion energy levels at each such point. The iteration was started using an ion density distribution based on assuming that ions behaved as neutrals, and iterating until the surface potential, surface ion current density, sheath potential and sheath electron density distributions all converged. Electron densities and currents were described by superpositions of Boltzmann factors. Each such calculation took about 6 hours on the AFGL Cyber 850 computer. The next intended step was to calculate an ion density distribution corresponding to the resulting sheath potential distribution, then "freeze" this ion density distribution and iterate the other quantities involved as before, and so on. To carry this procedure to convergence would probably take 20 to 30 hours on the same computer, so we have not so far made such calculations, and the results presented here are therefore based on the "neutral approximation" for ion densities, but on ion orbit-following for ion current collection on surfaces.

Preliminary results from these calculations are shown in Fig. 5.4, for hot-electron to-total-ion flux ratios R [See Eq. (2.8)] equal to 0.1, 0.25, 0.5, and 5.0. On the front and sides of the cylinder ($\theta \geq 80^\circ$), surface potentials seem to

increase more-or-less monotonically as one moves away from the front ($\theta = 180^\circ$), except for some relatively small oscillations which are probably spurious. One possible cause of these is too coarse a position-space discretization. Successive modifications of the computational grid to reduce such errors resulted in the final grid shown in Fig. 5.3, in which nodes are placed very densely just outside its surface, and the density of nodes is also increased in the region $80^\circ < \theta < 100^\circ$. Other possible causes include incomplete convergence or insufficiently fine sampling of the ion velocity space. Even with 32,768 orbits followed per surface point, very few of these will connect back to the ambient plasma with an ambient velocity close to that of the heavily-populated part of the ion distribution. This strongly suggests that in future calculations, outside-in orbit-following needs to be used for defining the most important region(s) of velocity space for incoming ion orbits, perhaps combined with inside-out orbit-following for doing detailed sampling of these regions.

However, on rearward surfaces ($\theta \leq 80^\circ$), there is some non-monotonicity which appears to be real. For $R = 0.1, 0.25$, and 0.5 , there are three surface-potential maxima, one at the rearmost point ($\theta = 0^\circ$) and one on each side of it. For $R = 0.1$ and 0.25 , these features were almost unchanged (the potentials of the maxima changed by less than 2%) when as few as 4,096 ion orbits (4 ion energy levels) were used, and this attests to their reality. For $R = 5$, we obtain four maxima, two on either side of the rearmost point. The minima between these peaks correspond to the ion "hot spots", or deposition points of highly beam-like ion populations, mentioned above. Most real situations would not possess the symmetry about the fore-aft line which our problem does, but our results nonetheless indicate that high-voltage wake regions of spacecraft are likely to contain very beam-like ion population constituents generally.

This is related also to the fact that the ambient ion distribution is a highly-directed ($S_i = 8$) one. A situation with ion drift is very different than one without. A drifting distribution is not an equilibrium one. The drift provides the ions with thermodynamic free energy which can support a much greater variety of phenomena than in the nondrifting case, including self-excited oscillations (Krall and Trivelpiece, 1973, Chs. 2 and 9). For related reasons, the drift also makes possible ion focusing effects including those discussed here. These effects depend on the fact that when the ambient ion velocity distribution is anisotropic, as it is very greatly when $S_i = 8$, a knowledge of the phase-space boundary separating orbits which connect back to infinity from those which do not, no longer gives complete information about the ion velocity distribution at any finite location. In the steady-state treatment described here, self-excited oscillations cannot be treated. However, oscillations observed in the outer portions of the Orbiter's wake involve density fluctuations of only a few per cent (Murphy, 1985; Murphy et al, 1986), so they probably do not have much effect on the steady-state wake properties studied here.

Beam-like ion constituents have important implications for more complicated situations, such as the interior of the Orbiter's camera. As our work has indicated, beam impact points will be very sensitive to details of the potential distribution on or near a spacecraft. Ions may come around a corner of the spacecraft, just miss one equipment box, and impact on one small corner of the next box, which may then come to a potential very different than those of its surroundings.

In addition, more than one ion beam may be present at some points in the sheath. Beams may come around corners from opposite sides of a spacecraft, and beams may also be present which have circled the spacecraft one or more times. Ion velocity

distributions as a function of direction may therefore contain many narrow "peaks" and "valleys". Simulation of a very detailed kind, which will tax the capabilities of the fastest computers presently available, will be necessary to resolve such situations.

In Fig. 2.2 we have also plotted the largest value of negative surface potential for each of the four values of R shown in Fig. 5.4, for comparison with our simple prediction from Sec. 2. These values are shown as circled points in this Figure. These results qualitatively resemble the theoretical curves in the same Figure, and also our expected behaviour shown in Fig. 5.1, in that they appear to show almost no dependence on R until a "threshold" value is reached, and then they show a rapid increase. Furthermore, this increase appears to begin at a substantially lower R value than for these curves, as one expects since the curves are for whole-body charging and the plotted points are for charging of electrically-isolated surfaces in the wake.

One feature of these results is unexpected: the "pre-threshold" wake charging, instead of being close to zero, is already several hundred volts. However, this apparent threshold is not the true one. "High-voltage" charging conventionally means that surface potential exceeds 100V in magnitude. For our conditions, and for a surface potential of -100V, the hot-electron flux exceeds the cold-electron flux when $R > 1.2 \times 10^{-215}$. Also, for $R = 0.1$ (the left margin of Fig. 2.2), if we calculate downstream-point potential using the neutral approximation for ion flux [Tsien, 1946; Parks and Katz, 1983, Eq. 4], we obtain $\phi_s = -3.3 \times 10^5 \text{V}$. For $R = 0$ (cold electrons only), a similar calculation yields $\phi_s = -14.8 \text{V}$. It is evident that all the numerical simulation results shown in Fig. 2.2 are "post-threshold" in the sense that

they involve a current balance primarily between the hot electron flux and wake-region ion fluxes that are already heavily modified by orbit curvature in strong wake-region electric fields. This is evidently a situation in which even a small amount of ambient H^+ can be expected to produce a large decrease in the magnitudes of wake-region potentials. In Section 4.4, we examined H^+ effects on wake-region potentials using the model-potential calculation of ion densities developed in Section 4.3 and Appendices C and D, and we made a preliminary determination that H^+ densities were too small in most low-polar-orbit conditions to cause a significant reduction in wake-induced-barrier-effect potentials. In the situation studied in this Section, downstream H^+ fluxes rather than densities are the most important issue. We intend to include H^+ effects in future calculations.

6. CONCLUSIONS

In Section 1 of this Report, we reviewed the main differences between the plasma environments in geosynchronous orbit and low polar orbit with respect to high-voltage charging situations, and we gave reasons why the task of predicting high-voltage charging or related environmental effects on a spacecraft is more complicated in the low-polar-orbit situation.

In Section 2, we developed a simple rough estimate of the environmental conditions required for overall charging of a large spacecraft in low-orbit auroral-zone conditions. The results indicate that for any given spacecraft, surface potentials are likely to depend more strongly on the ratio of ambient flux of high-energy electrons to that of all ions than on any other environmental parameter. This prediction has been corroborated experimentally by results of Gussenhoven et al (1985) obtained using the DMSP F6 and F7 satellites; see their Fig. 7 and associated discussion, and also Laframboise and Parker (1986, 1987).

In Section 3, we presented an approximate theoretical treatment of suppression by magnetic fields of the escape of electrons emitted from negatively-charged spacecraft surfaces. Our treatment of this topic is intended to serve a variety of purposes. Its results provide a "parameterization" of the electron-escape problem which can be used as part of large spacecraft-charging

simulation programs, and this may permit important reductions in the cost of using such programs. Our results also permit simple estimates of the importance of magnetic electron-escape suppression in particular situations. However, their most important use may be to permit gaining an understanding of an effect which appears likely to dominate the high-voltage charging of mostly-dielectric large spacecraft such as the Shuttle Orbiter in low polar orbit. The nature of our results strongly implies that on such spacecraft, local charging, especially on downstream-facing surfaces nearly parallel to \mathbf{B} , may occur in ionospheric conditions which do not produce overall charging. These conditions may include lower equivalent auroral-electron temperatures and also daylit parts of the orbit. This question demands experimental investigations and detailed numerical simulations.

Our results in Sections 3.3-3.5 also show "sensitivity" effects which have disturbing implications. These effects imply that obtaining realistic predictions of high-voltage polar-orbit charging in geometrically complicated situations is likely to prove a computational task of great difficulty. An experimental investigation of magnetic-field effects on secondary-electron and photoelectron escape from negatively-charged surfaces would be of great value, and we hope that the work presented in Section 3 will stimulate such efforts.

In Section 4, we developed theory which permits an approximate calculation of potentials produced on wake-region spacecraft surfaces by the wake-induced-barrier effect. In Section 4.4, we have used this theory to estimate surface potentials on large spacecraft covered mostly with dielectric, including the Shuttle Orbiter, in auroral-plasma conditions. In Section 4.5, we have proposed an explanation, involving the wake-induced-barrier effect, for observations, made during electron-beam emissions from the SEPAC Spacelab-1 experiment, that the Orbiter's frame charged to beam emission voltage when the emitter faced downstream but not upstream.

In auroral-plasma conditions, we predict that the largest wake-induced-barrier-effect potentials will occur when the Orbiter's wing plane is perpendicular to its orbital motion and the hot (≥ 1 keV) electron constituent has the largest possible density (Eq. 4.12). For the largest such density so far observed, we predict potentials more than 100V negative on surfaces located near the wake center. For larger spacecraft in the same plasma conditions, we predict potentials several hundred volts negative.

In contrast with the situation for low-polar-orbit charging already observed on the DMSP F6 and F7 satellites (Gussenhoven et al, 1985; Yeh and Gussenhoven, 1987), wake-induced-barrier-effect charging does not require the ambient hot

electrons to be energetic enough that their incident flux overcomes secondary and backscattered emission fluxes, because these are suppressed by the potential barrier involved in this mechanism. As in the case of suppression by **B** effects, this extends, to lower equivalent temperatures, the range of auroral-electron plasma conditions for which high-voltage Orbiter charging can be expected. This barrier will also suppress photoemission. This appears likely to permit daylight charging by this mechanism, as also was the case for suppression by **B** effects. We therefore predict that daylight auroral-zone charging of wake-region dielectric surfaces to potentials more than 100V negative will occur at least occasionally on the Orbiter.

The largest uncertainties in our wake-induced-barrier-effect predictions result from three causes (Section 4.4). The first is the lack of available measurements of electron and ion energy distributions made at the same time and place with concentration measurements of individual ion species in the auroral zone at low-orbit altitudes. The second is the difficulty of accurately predicting wake-region electron-density enhancements caused by emitted-electron space charge, in the presence of magnetic-field and "hopping-conductivity" effects (Sections 3 and 4.3; see also Fig. 3.9). The third cause is the difficulty of accurately predicting ion-density distributions in high-voltage spacecraft wakes (Section 4.3 and Appendix C).

Further work is needed in all of these areas, and in Section 5, we have presented preliminary results from a numerical simulation which was developed in order to make detailed investigations of the phenomena identified in Sections 2-4. This work involves calculations of floating-potential distributions on infinite dielectric cylinders in collisionless plasma crossflows whose properties model those of the auroral plasma. Results from this simulation indicate the presence of multiple maxima and minima in the downstream-side surface potential distribution, in contrast with a monotonic progression of increasingly negative potentials from upstream to downstream surfaces, as might have been expected. These features are caused by the presence of ion "hot spots" or deposition points of very beam-like ion populations, which in turn are the result of a highly anisotropic ($S_i = 8$) ambient-ion velocity distribution accelerated into a wake region containing negative voltages large compared with the ion ram energy. When combined with the geometrical complexity of a typical payload arrangement in the Orbiter's cargo bay, this promises to make detailed prediction of wake-region surface potentials a formidable task.

The work presented in Sections 2-5 has involved initial explorations of several distinct topics related to high-voltage low-polar-orbit charging. Except perhaps for our treatment of electron escape currents in Section 3, we have not treated any of these topics exhaustively, and our treatments therefore need in the

future to be extended in many ways. The calculation of downstream-point ion space charge densities for a cylinder, presented in Section 4.3 and Appendices C and D, can be easily adapted to spherical geometry and also to provide downstream-point ion current densities. These current densities could then be used to provide simple estimates of required environmental conditions for downstream-point local charging in a manner analogous to the estimate for overall charging developed in Section 2. Using available electron-emission yield data (Sections 1, 3.3, and 4.5), these estimates should be corrected for secondary-electron and backscattered-electron emission for use in circumstances in which it is expected that these electrons can escape. The calculation of emitted-electron escape currents developed in Section 3 can be readily extended to provide corresponding values of surface currents due to reimpacting electrons. In fact, program SCAPE, which is listed in Appendix A, already includes provision for doing this, but tests of this feature of the program, conducted in conjunction with obtaining the escape-current results presented in Figs. 3.5 and 3.10-3.17 and Table 2, indicated that velocity-space discretizations which were fine enough for calculating these escape currents were not fine enough to yield equivalent accuracy in the surface-current calculations. Surface currents need to be taken into account in order to refine the estimates of wake-induced-barrier-effect potential obtained in Section 4. However, in that situation, electric forces

on emitted electrons are directed toward rather than away from spacecraft surfaces, so the formulation of Sec. 3 is inapplicable in its present form. The most applicable formulation would involve a modification of the analytic surface-current expression given by Eq. (9) of Laframboise et al (1981) or Eq. (6.7) of Laframboise et al (1982b), to include magnetic-field effects. The numerical simulation presented in Section 5 should be extended to include effects of magnetic fields, H^+/O^+ ion mixtures, electron emission from surfaces, surface currents produced by reimpact of nonescaping emitted electrons, wake-induced barriers, and other spacecraft shapes, e.g. spherical rather than infinite-cylindrical, and effects of ion-orbit curvature on space-charge densities. All of these results need to be compared with all available experimental data on polar-orbit charging.

There remain two topics which we mentioned in Section 1 but have not treated in this Report. The first of these is collisional effects. We have regarded these as being inappropriate for study as part of the work described by this Report because an understanding of the important collisionless effects is a precondition to understanding how these might be modified by collisions. In any case, the most likely result of collisional effects on the Orbiter appears to be that collisional ionization of fortuitous gas releases may occasionally cause discharge of surfaces charged to large voltages.

The other untreated topic is the possible modification of time-averaged spacecraft wake quantities by nonlinear effects of spontaneous plasma fluctuations. We have briefly alluded to these effects in Sections 3.4 and 5, and we have indicated therein that available evidence makes it seem unlikely that such effects are important. However, both this and the collisional problem are largely unexplored, and as we have indicated earlier in this Section and elsewhere in this Report, the various collisionless effects explored in Sections 2-5 are far from completely studied. At present, it is far from clear when large dielectric-covered spacecraft such as the Shuttle Orbiter will begin flights through the auroral zones, but the problem of predicting high-voltage charging in these regions appears to be complex enough to deserve further investigation, and this should take place well in advance of whenever such flights are rescheduled if it is considered desirable to achieve detailed predictive capability in time for them.

REFERENCES

- Al'pert, Ya.L., Gurevich, A.V., and Pitaevskii, L.P., Space Physics with Artificial Satellites. Consultants Bureau, New York, 1965.
- Bernstein, I.B., and Rabinowitz, I.N., Theory of Electrostatic Probes in a Low-Density Plasma. *Phys. Fluids* 2, 112, 1959.
- Besse, A.L., Unstable Potential of Geosynchronous Spacecraft. *J. Geophys. Res.* 86, 2443, 1981.
- Besse, A.L., and Rubin, A.G., A Simple Analysis of Spacecraft Charging Involving Blocked Photoelectron Currents. *J. Geophys. Res.* 85, 2324, 1980.
- Brundin, C.L., Effects of Charged Particles on the Motion of an Earth Satellite. *AIAA Jour.* 1, 2529, 1963.
- Call, S.M., The Interaction of a Satellite with the Ionosphere. Rep. 46, Plasma Lab., Columbia University, New York, 1969.
- Chang, J-S., Godard, R., and Laframboise, J.G., Mass-discrimination in ion and neutral extraction by mass-spectrometers under spacecraft conditions. *Planet. Space Sci.* 27, 1213, 1979.
- Chung, M.S., and Everhart, T.E., Simple calculation of energy distribution of low-energy secondary electrons emitted from metals under electron bombardment. *J. Appl. Phys.* 45, 707, 1974.
- Comfort, R.H., Baugher, C.R., and Chappell, C.R., Use of the thin sheath approximation for obtaining ion temperatures from the ISEE 1 limited aperture RPA, *J. Geophys. Res.* 87, 5109, 1982.
- de Leeuw, J.H., A brief introduction to ionospheric aerodynamics. In: *Proc. Fifth Internat. Symp. on Rarefied Gas Dynamics*, edited by C.L. Brundin, Academic Press, New York, pp. 1561-1586, 1967.
- Fahleson, U., Plasma-vehicle interactions in space: some aspects of present knowledge and future development, in: *Photon and Particle Interactions with Surfaces in Space*, edited by R.J.L. Grard, pp. 563-569, D. Reidel, Hingham, Mass., 1973.

- Fennell, J.F., Gorney, D.J., and Mizera, P.F., Auroral particle distribution functions and their relationship to inverted Vs and auroral arcs, in: Physics of Auroral Arc Formation, Geophys. Monogr. Ser. vol 25, edited by S.-I. Akasofu and J.R. Kan, p. 91, AGU, Washington, D.C., 1981.
- Feuerbacher, B., and Fitton, B., Experimental Investigation of Photoemission from Satellite Surface Materials. J. Appl. Phys. 43, 1563, 1972.
- Garrett, H.B., The Charging of Spacecraft Surfaces. Rev. Geophys. and Space Phys. 19, 577, 1981.
- Garrett, H.B., and Rubin, A.G., Spacecraft charging at geosynchronous orbit - generalized solution for eclipse passage. Geophys. Res. Lett. 5, 865, 1978.
- Goldstein, H., Classical Mechanics, 2nd Ed., Addison-Wesley, Reading, Mass., 1980.
- Goodrich, G.W., and Wiley, W.C., Resistance Strip Magnetic Electron Multiplier. Rev. Sci. Instrum. 32, 846, 1961.
- Grard, R.J.L., Properties of the Satellite Photoelectron Sheath Derived from Photoemission Laboratory Measurements. J. Geophys. Res. 78, 2885, 1973.
- Gurevich, A.V., Pitaevskii, L.P., and Smirnova, V.V., Ionospheric Aerodynamics. Sov. Phys. Uspek. 99, 595, 1970.
- Gussenhoven, M.S., Hardy, D.A., Rich, F., Burke, W.J., and Yeh, H.-C., High-Level Spacecraft Charging in the Low-Altitude Polar Auroral Environment. J. Geophys. Res. 90, 11009, 1985.
- Hachenberg, O., and Brauer, W., Secondary electron emission from solids. Advan. Electron. Electron. Phys. 11, 413, 1959.
- Hinteregger, H.E., Damon, K.R., and Hall, L.A., Analysis of photoelectrons from solar extreme ultraviolet. J. Geophys. Res. 64, 961, 1959.
- Kanal, M., Theory of current collection of moving spherical probes. Space Physics Research Lab., University of Michigan, Ann Arbor, report JS-5, 1962.

Katz, I., Cassidy, J.J., Mandell, M.J., Schnuelle, G.W., and Steen, P.G., The capabilities of the NASA charging analyzer program, in: Spacecraft Charging Technology - 1978, NASA Conf. Pub. 2071/Rep. AFGL-TR-79-0082, pp. 101-122, Air Force Geophysics Lab., Hanscom Air Force Base, Mass. 1979. **ADA084026**

Katz, I., and Mandell, M.J., Differential Charging of High-Voltage Spacecraft: The Equilibrium Potential of Insulated Surfaces. J. Geophys. Res. 87, 4533, 1982.

Katz, I., and Parks, D.E., Space shuttle orbiter charging. J. Spacecraft and Rockets 20, 22, 1983.

Katz, I., Mandell, M.J., Jongeward, G., and Gussenhoven, M.S., The Importance of Accurate Secondary Electron Yields in Modeling Spacecraft Charging. J. Geophys. Res. 91, 13739, 1986.

Kiel, R.E., Gey, F.C., and Gustafson, W.A., Electrostatic Potential Fields of an Ionospheric Satellite. AIAA Jour. 6, 690, 1968.

Krall, N.A., and Trivelpiece, A.W., Principles of Plasma Physics. McGraw-Hill, New York, 1973.

Laframboise, J.G., Is there a good way to model spacecraft charging in the presence of space charge coupling, flow, and magnetic fields? In: Proc. Air Force Geophys. Lab. Workshop on Natural Charging of Large Space Structures in Near Earth Polar Orbit, edited by R.C. Sagalyn, D.E. Donatelli, and I. Michael, Report No. AFGL-TR-83-0046/Environmental Research Paper No. 825, Air Force Geophysics Laboratory, Massachusetts, pp. 57-78, 1983a. **ADA134894**

Laframboise, J.G., Incident velocity distributions on sampling electrodes of spacecraft plasma instruments. In: Proc. 17th ESLAB Symposium on "Spacecraft/Plasma Interactions and their Influence on Field and Particle Measurements", Report No. ESA SP-198, European Space Agency Scientific and Technical Publications Branch, ESTEC, Noordwijk, The Netherlands, pp. 101-108, 1983b.

- Laframboise, J.G., Calculation of secondary-electron escape currents from inclined spacecraft surfaces in a magnetic field. In: Spacecraft Environmental Interactions Technology 1983, edited by C.K. Purvis and C.P. Pike, NASA Conference Publication 2359/Report No. AFGL-TR-85-0018, Air Force Geophysics Laboratory, Massachusetts, pp. 277-286, 1985a. ADA202020
- Laframboise, J.G., Predicting high-voltage charging of spacecraft in low polar orbit. Report No. AFGL-TR-85-0263, Air Force Geophysics Laboratory, Massachusetts, 1985b. ADA166617
- Laframboise, J.G., Calculation of Escape Currents from Negatively-Charged Spacecraft Surfaces in a Magnetic Field. J. Geophys. Res. 93, 1933, 1988.
- Laframboise, J.G., Kamitsuma, M., and Godard, R., Multiple floating potentials, "threshold-temperature" effects, and "barrier" effects in high-voltage charging of exposed surfaces on spacecraft. In: Proc. Internat. Symp. on Spacecraft Materials in Space Environment, June 1982, Toulouse, France, European Space Agency, Paris, Publication no. ESA SP-178, pp. 269-275, 1982a.
- Laframboise, J.G., Kamitsuma, M., Prokopenko, S.M.L., Chang, Jen-Shih, and Godard, R., Numerical simulation of spacecraft charging phenomena at high altitude. Final Report on Grant AFOSR-76-2962, York University, 1982b.
- Laframboise, J.G., and Kamitsuma, M., The threshold temperature effect in high-voltage spacecraft charging. In: Proc. Air Force Geophys. Lab. Workshop on Natural Charging of Large Space Structures in Near Earth Polar Orbit, edited by R.C. Sagalyn, D.E. Donatelli, and I. Michael, Report No. AFGL-TR-83-0046/Environmental Research Paper No. 825, Air Force Geophysics Laboratory, Massachusetts, pp. 293-308, 1983. ADA134894
- Laframboise, J.G., and Parker, L.W., Probe design for orbit-limited current collection. Phys. Fluids 16, 629, 1973.
- Laframboise, J.G., and Parker, L.W., Progress toward predicting high-voltage charging of spacecraft in low polar orbit. Report No. AFGL-TR-86-0261, Air Force Geophysics Laboratory, Massachusetts, 1986. ADA176939

- Laframboise, J.G., and Parker, L.W., Spacecraft charging in the auroral plasma: progress toward understanding the physical effects involved. In: "The Aerospace Environment at High Altitudes and its Implications for Spacecraft Charging and Communications", AGARD Conference Proceedings No. 406, North Atlantic Treaty Organization, Neuilly-Sur-Seine, France, pp. 13-1 to 13-16, 1987.
- Laframboise, J.G., and Prokopenko, S.M.L., Numerical Simulation of Spacecraft Charging Phenomena, in: Proc. Spacecraft Charging Technology Conference, edited by C.P. Pike and R.R. Lovell, pp. 309-318, Rep. AFGL-TR-77-0051, Air Force Geophysics Laboratory, Mass./Rep. NASA TMX-73537, Lewis Research Center, Cleveland, Ohio, 1977. ADA045459
- Laframboise, J.G., Prokopenko, S.M.L., Kamitsuma, M., and Godard, R., Results from a two-dimensional spacecraft charging simulation and comparison with a surface photocurrent model. In: Spacecraft Charging Technology 1980, NASA Conference Publication 2182/Report No. AFGL-TR-81-0270, Air Force Geophysics Laboratory, Massachusetts, pp. 709-716, 1981. ADA114426
- Laframboise, J.G., and Rubinstein, J., Theory of a cylindrical probe in a collisionless magnetoplasma. Phys. Fluids 19, 1900, 1976.
- Lai, S.T., Gussenhoven, M.S., and Cohen, H.A., The concepts of critical temperature and energy cutoff of ambient electrons in high-voltage charging of spacecraft. In: Proc. 17th ESLAB Symposium on "Spacecraft/Plasma Interactions and their Influence on Field and Particle Measurements", Report No. ESA SP-198, European Space Agency Scientific and Technical Publications Branch, ESTEC, Noordwijk, The Netherlands, pp. 169-175, 1983.
- Langmuir, I., and Blodgett, K.B., Currents limited by space charge between concentric spheres. Phys. Rev. 23, 49, 1924.
- Leung, M.S., Tueling, M.B., and Schnauss, E.R., Effects of Secondary Electron Emission on Charging, In: Spacecraft Charging Technology 1980, pp. 163-178, NASA Conf. Publ. 2182/Rep. AFGL-TR-81-0270, Air Force Geophys. Lab., Mass., 1981. ADA114426
- Lin, C.S., and Hoffman, R.A., Observations of inverted-V electron precipitation. Space Sci. Rev. 33, 415, 1982.

- Linson, L.M., Current-Voltage Characteristics of an Electron-Emitting Satellite in the Ionosphere. *J. Geophys. Res.* 74, 2368, 1969.
- Martin, A.K., Numerical solutions to the problem of charged particle flow around an ionospheric spacecraft. *Planet. Space Sci.* 22, 121, 1974.
- Maslennikov, M.V., and Sigov, Yu. S., A discrete model for the study of the flow of a rarefied plasma about a body. *Sov. Phys. Doklady* 9, 1063, 1965.
- Maslennikov, M.V., and Sigov, Yu. S., Discrete model of medium in a problem on rarefied plasma stream interaction with a charged body. In: *Proc. 5th Internat. Symp. on Rarefied Gas Dynamics*, edited by C.L. Brundin, Vol. 2, pp. 1657-1670, Academic Press, New York, 1967.
- Maslennikov, M.V., Sigov, Yu. S., and Churkina, G.P., Numerical experiments on flow of rarefied plasma around bodies of various shapes. *I. Cosmic Research* 6, 184, 1968.
- Maslennikov, M.V., and Sigov, Yu. S., Rarefied plasma stream interaction with charged bodies of various forms. In: *Proc. 6th Internat. Symp. on Rarefied Gas Dynamics*, edited by L. Trilling and H.Y. Wachman, Vol. 2, pp. 1671-1680, Academic Press, New York, 1969.
- McCoy, J.E., Konradi, A., and Garriott, O.K., Current leakage for low-altitude satellites. In: *Space Systems and Their Interactions with Earth's Space Environment*, edited by H.B. Garrett and C.P. Pike, *Progress in Astronautics and Aeronautics*, Vol. 71, Amer. Inst. Aeron. Astron., New York, pp. 523-553, 1980.
- Meyer-Vernet, N., Multivalued electrostatic potentials; "chance or necessity" for the charge of solid particles near Saturn? In: *Proc. IAU Colloq. No. 75: Planetary Rings*, Internat. Astron. Union, pp. 615-625, 1982.
- Mott-Smith, H.M., and Langmuir, I., The theory of collectors in gaseous discharges. *Phys. Rev.* 28, 727, 1926.
- Mullen, E.G., Gussenhoven, M.S., Hardy, D.A., Aggson, T.A., Ledley, B.G., and Whipple, E., SCATHA Survey of High-Level Spacecraft Charging in Sunlight. *J. Geophys. Res.* 91, 1474, 1986.

- Murphy, G.B., Electromagnetic environment of the Orbiter at S-band and Ku-band frequencies. Paper AIAA-85-7036-CP, AIAA Shuttle Environment and Operations II Conference, Houston, 11-13 Nov. 1985.
- Murphy, G.B., Pickett, J., D'Angelo, N., and Kurth, W.S., Measurements of Plasma Parameters in the Vicinity of the Space Shuttle. Planet. Space Sci. 34, 993, 1986.
- Narcisi, R.S., Mass Spectrometer Measurements in the Ionosphere. In: Physics and Chemistry of Upper Atmospheres, edited by B.M. McCormac, pp. 171-183, D. Reidel, Dordrecht, Holland, 1973.
- Olsen, R.C., A Threshold Effect for Spacecraft Charging. J. Geophys. Res. 88, 493, 1983.
- Olsen, R.C., McIlwain, C.E., and Whipple, E.C., Jr., Observations of differential charging effects on ATS 6. J. Geophys. Res. 86, 6809, 1981.
- Olsen, R.C., and Purvis, C.K., Observations of Charging Dynamics. J. Geophys. Res. 88, 5657, 1983.
- Parker, L.W., Theory of the external sheath structure and ion collection characteristics of a rocket-borne mass spectrometer, Report No. AFCRL-71-0105, Air Force Geophysics Laboratory, Massachusetts, 1970. AD720833
- Parker, L.W., Calculation of sheath and wake structure about a pillbox-shaped spacecraft in a flowing plasma. In: Proc. Spacecraft Charging Technology Conf., edited by C.P. Pike and R.R. Lovell, Report No. AFGL-TR-77-0051, Air Force Geophysics Laboratory, Massachusetts/NASA TMX-73537, Lewis Research Center, Cleveland, pp. 331-366, 1977. ADA045459
- Parker, L.W., Contributions to satellite sheath and wake modeling. In: Proc. 17th ESLAB Symposium on "Spacecraft/Plasma interactions and their Influence on Field and Particle Measurements", Report No. ESA SP-198, European Space Agency Scientific and Technical Publications Branch, ESTEC, Noordwijk, The Netherlands, pp. 81-100, 1983.
- Parker, L.W., and Murphy, B.L., Potential Buildup on an Electron-Emitting Ionospheric Satellite. J. Geophys. Res. 72, 1631, 1967.

- Parker, L.W., and Whipple, E.C., Jr., Theory of Spacecraft Sheath Structure, Potential, and Velocity Effects on Ion Measurements by Traps and Mass Spectrometers. J. Geophys. Res. 75, 4720, 1970.
- Parks, D.E., and Katz, I., Charging of a large object in low polar Earth orbit. In: Spacecraft Charging Technology 1980, NASA Conference Publication 2182/Report No. AFGL-TR-81-0270, Air Force Geophysics Laboratory, Massachusetts, pp. 979-989, 1981. **ADA114426**
- Parks, D.E., and Katz, I., Mechanisms that limit potentials on ionospheric satellites. J. Geophys. Res. 88, 9155, 1983.
- Parks, D.E., and Katz, I., Electric field effects on ion currents in satellite wakes. In: Spacecraft Environmental Interactions Technology 1983, edited by C.K. Purvis and C.P. Pike, NASA Conference Publication 2359/Report No. AFGL-TR-85-0018, Air Force Geophysics Laboratory, Massachusetts, pp. 195-204, 1985.
- Parrot, M.J.M., Storey, L.R.O., Parker, L.W., and Laframboise, J.G., Theory of cylindrical and spherical Langmuir probes in the limit of vanishing Debye number. Phys. Fluids 25, 2388, 1982.
- Prokopenko, S.M.L., and Laframboise, J.G., Prediction of Large Negative Shaded-Side Spacecraft Potentials. In: Proc. Spacecraft Charging Technology Conference, edited by C.P. Pike and R.R. Lovell, pp. 369-387, Rep. AFGL-TR-77-0051, Air Force Geophysics Laboratory, Mass./Rep. NASA TMX-73537, Lewis Research Center, Cleveland, Ohio, 1977. **ADA045459**
- Prokopenko, S.M.L., and Laframboise, J.G., High-Voltage Differential Charging of Geostationary Spacecraft, J. Geophys. Res. 85, 4125, 1980.
- Purvis, C., Evolution of Spacecraft Charging Technology, Paper No. 82-0273, Amer. Inst. Aeron. Astron. 20th Aerospace Sciences Meeting, Orlando, Florida, January 1982.
- Rich, F.J., Ionospheric Characteristics: A Review. In: Proc. Air Force Geophys. Lab. Workshop on Natural Charging of Large Space Structures in Near-Earth Polar Orbit: 14-15 September 1982, edited by R.C. Sagalyn, D.E. Donatelli, and I. Michael, Rep. AFGL-TR-83-0046, Air Force Geophys. Lab., Massachusetts, pp. 29-56, 1983. **ADA134894**

- Rubin, A.G., Rothwell, P.L., and Yates, G.K., Reduction of spacecraft charging using highly emissive surface materials. In: Proc. 1978 Symp. on the Effect of the Ionosphere on Space and Terrestrial Systems, Naval Research Lab., Washington, D.C., pp. 313-316, 1978.
- Rubinstein, J., and Laframboise, J.G., Upper-bound current to a cylindrical probe in a collisionless magnetoplasma. *Phys. Fluids* 21, 1655, 1978.
- Rubinstein, J., and Laframboise, J.G., Theory of a spherical probe in a collisionless magnetoplasma. *Phys. Fluids* 25, 1174, 1982.
- Rubinstein, J., and Laframboise, J.G., Theory of axially-symmetric probes in a collisionless magnetoplasma: Aligned spheroids, finite cylinders, and disks. *Phys. Fluids* 26, 3624, 1983.
- Samir, U., and Stone, N.H., The Interaction of Small and Large Spacecraft with Their Environment. In: Space Technology Plasma Issues in 2001, edited by H. Garrett, J. Feynmann, and S. Gabriel, JPL Publication 86-49, NASA Jet Propulsion Laboratory, Pasadena, pp. 69-91, 1986.
- Samir, U., Wildman, P.J., Rich, F., Brinton, H.C., and Sagalyn, R.C., About the Parametric Interplay Between Ionic Mach Number, Body-Size, and Satellite Potential in Determining the Ion Depletion in the Wake of the S3-2 Satellite. *J. Geophys. Res.* 86, 11161, 1981.
- Sanmartin, J.R., Theory of a Probe in a Strong Magnetic Field. *Phys. Fluids* 13, 103, 1970.
- Sasaki, S., Kawashima, N., Kuriki, K., Yanagisawa, M., and Obayashi, T., Vehicle Charging Observed in SEPAC Spacelab-1 Experiment. *J. Spacecraft* 23, 194, 1986.
- Schnuelle, G.W., Stannard, P.R., Katz, I., and Mandell, M.J., Simulation of charging response of SCATHA (P78-2) satellite. In: Spacecraft Charging Technology 1980, NASA Conference Publication 2182/Report No. AFGL-TR-81-0270, Air Force Geophysics Laboratory, Massachusetts, pp. 580-591, 1981. ADA114426
- Shepherd, M.M., and Laframboise, J.G., Chebyshev approximation of $(1+2x)\exp(x^2)\operatorname{erfc} x$ in $0 \leq x < \infty$. *Math. of Computation* 36, 249, 1981.

- Singh, N., and Baughen, C.R., Sheath effects on current collection by particle detectors with narrow acceptance angles. *Space Sci. Instrum.* 5, 295, 1981.
- Sternglass, E.J., Backscattering of Kilovolt Electrons from Solids. *Phys. Rev.* 95, 345, 1954.
- Stone, N.H., and Samir, U., The Plasma Dynamics of Hypersonic Spacecraft: Applications of Laboratory Simulations and Active In-Situ Experiments. In: *Space Technology Plasma Issues in 2001*, edited by H. Garrett, J. Feynmann, and S. Gabriel, JPL Publication 86-49, NASA Jet Propulsion Laboratory, Pasadena, pp. 127-148, 1986.
- Swider, W., Section 21.4 of Chapter 21: Atmospheric Composition, in: *Handbook of Geophysics and the Space Environment*, edited by A.S. Jursa, Air Force Geophysics Laboratory, Mass., pp. 21-51 to 21-67, 1985.
ADA167000, AFGL-TR-85-0315
- Taylor, J.C., Disturbance of a Rarefied Plasma by a Supersonic Body on the Basis of the Poisson-Vlasov Equations - I. The Heuristic Method. *Planet. Space Sci.* 15, 155, 1967.
- Taylor, W.W.L., Obayashi, T. Kawashima, N., Sasaki, S., Yanagisawa, M., Burch, J.L., Reasoner, D.L., and Roberts, W.T., Wave-particle interactions induced by SEPAC on Spacelab 1: Wave observations. *Radio Sci.*, 20, 486, 1985.
- Tsien, H.-S., Superaerodynamics, mechanics of rarefied gases. *J. Aeronaut. Sci.* 13, 653, 1946.
- Vaglio-Laurin, R., and Miller, G., Electrostatic Field in the Trail of Ionospheric Satellites. *AIAA Jour.* 8, 1098, 1970.
- Whipple, E.C., Jr., Observation of Photoelectrons and Secondary Electrons Reflected from a Potential Barrier in the Vicinity of ATS 6. *J. Geophys. Res.* 81, 715, 1976.
- Whipple, E.C., Potentials of surfaces in space. *Rep. Prog. Phys.* 44, 1197, 1981.

Whipple, E.C., Warnock, J.M. and Winkler, R.H., Effects of satellite potential on direct ion density measurements through the plasmopause. J. Geophys. Res. 79, 179, 1974.

Wiley, W.C., and Herdee, C.F., Electron multipliers utilizing continuous strip surfaces. IRE Trans. Nucl. Sci. NS-9, 103, 1962.

Wrenn, G.L., and Heikkila, W.J., Photoelectrons emitted from ISIS spacecraft. In: Photon and Particle Interactions with Surfaces in Space, edited by R.J.L. Grand, D. Reidel, Dordrecht, Netherlands, pp. 221-230, 1973.

Yeh, H.-C., and Gussenhoven, M.S., The Statistical Electron Environment for Defense Meteorological Satellite Program Eclipse Charging. J. Geophys. Res. 92, 7705, 1987.

TABLE 1. Low-Earth-Orbit Conditions**

a) CHARACTERISTIC LENGTHS		
Ambient Debye Length:		≤ 1 cm
Thickness of 1kV and 5kV spherically-symmetric sheath*** around a sphere of radius 3m:		2.5m and 5.8m
Thickness of 1kV and 5kV planar Child-Langmuir sheath:		5.0m and 17m (WHY SO LARGE?)
Particle gyroradii:		
ambient electrons (0.1 eV)	2 cm	
secondary electrons (3 eV)	13 cm	
auroral electrons (10 keV)	8 m	
ions (O^+ ; 0.1 eV)	3m in "rest" frame	
	27 m* in spacecraft frame	
	(larger inside a high-voltage sheath)	
(b) CHARACTERISTIC SPEEDS:		
Ion thermal speed:	1 km/sec	
Spacecraft speed:	≤ 8 km/sec, depending on orbit	SITUATION IS
Electron thermal speed:	100 km/sec, for ambient electrons	" MESOTHERMAL "

* Particle motions do not depend on the frame of reference in which they are viewed. The transformation from rest frame to spacecraft frame produces a $\mathbf{V} \times \mathbf{B}$ electric field $\leq 0.35V/m$ where \mathbf{V} = spacecraft velocity and \mathbf{B} = magnetic induction; electric fields inside a 1kV sheath are ~ 200 V/m.

** deLeeuw (1967), p. 1564; Martin (1974).

*** Al'pert et al (1965), Fig. 72.

TABLE 2

Values of the ratio $i = I/I_0$ of escaping to emitted flux, for various values of θ , the angle (in degrees) between the surface normal and the magnetic-field direction, ϵ , the nondimensional repelling electric-field strength, and the two angles α and ψ , also in degrees, defining the electric-field direction. The definitions of α and ψ are given by Figure 3.7. These four quantities appear in Table 2 as THETA, EPS, ALPHA, and PSI, respectively. For $\theta = 0^\circ$ and $\alpha = 0^\circ$, the electric field is normal to the surface. The results for this case have a numerical accuracy of about 0.2% or better; see Sections 3.2 and 3.3. For nonzero values of α and ψ , the results have a numerical accuracy of about 0.4% or better; see Sections 3.4 and 3.5. The results given in Table 2 are plotted in Figures 3.5 and 3.10-3.17.

ESCAPING FLUXES AND SURFACE CURRENTS OF EMITTED ELECTRONS IN UNIFORM E AND B FIELDS.
86 AUG 29A , CASE 3

NALFA NPSI NTH NEPS NTAU MINT NVX NVY NVZ
1 1 11 8 90 4 80 80 40

ANGLES DEFINING ELECTRIC-FIELD DIRECTION: ALPHA = 0.000 DEGREES, PSI = 0.000 DEGREES

ESCAPING FLUXES

EPS	0.00	.20	.50	1.00	2.00	5.00	10.00	20.00
THETA								
0.00	1.000	1.000	1.000	1.000	1.000	1.000	1.000	1.000
15.00	.964	.990	.999	1.000	1.000	1.000	1.000	1.000
30.00	.865	.930	.977	.997	1.000	1.000	1.000	1.000
45.00	.706	.796	.892	.970	.999	1.000	1.000	1.000
60.00	.499	.585	.704	.856	.982	1.000	1.000	1.000
75.00	.258	.311	.396	.545	.802	.998	1.000	1.000
80.00	.173	.209	.270	.383	.618	.968	1.000	1.000
85.00	.087	.105	.137	.198	.341	.723	.971	1.000
87.00	.052	.063	.082	.119	.209	.487	.810	.991
89.00	.016	.020	.026	.039	.069	.172	.338	.618
90.00	0.000	0.000	0.000	0.000	0.000	0.000	0.000	0.000

ESCAPING FLUXES AND SURFACE CURRENTS OF EMITTED ELECTRONS IN UNIFORM E AND B FIELDS.

86 JUN 13A , CASE 3

NALFA NPSI NTH NEPS NTAU MINT NVX NVY NVZ
1 1 21 8 90 4 64 64 32

ANGLES DEFINING ELECTRIC-FIELD DIRECTION: ALPHA = 30.000 DEGREES, PSI = 0.000 DEGREES

ESCAPING FLUXES

EPS THETA	0.00	.20	.50	1.00	2.00	5.00	10.00	20.00
-60.00	.499	.527	.565	.615	.676	.724	.738	.745
-57.00	.544	.577	.623	.688	.780	.908	.981	1.000
-54.00	.587	.625	.678	.754	.862	.980	1.000	1.000
-51.00	.628	.671	.730	.812	.919	.997	1.000	1.000
-48.00	.668	.714	.777	.861	.956	1.000	1.000	1.000
-45.00	.706	.755	.819	.900	.978	1.000	1.000	1.000
-40.00	.765	.816	.879	.947	.994	1.000	1.000	1.000
-35.00	.818	.868	.925	.976	.999	1.000	1.000	1.000
-30.00	.864	.912	.958	.990	1.000	1.000	1.000	1.000
-15.00	.963	.986	.997	1.000	1.000	1.000	1.000	1.000
0.00	1.000	1.000	1.000	1.000	1.000	1.000	1.000	1.000
15.00	.963	.988	.998	1.000	1.000	1.000	1.000	1.000
30.00	.864	.932	.977	.996	1.000	1.000	1.000	1.000
45.00	.706	.810	.908	.976	.999	1.000	1.000	1.000
60.00	.499	.615	.759	.908	.992	1.000	1.000	1.000
75.00	.258	.346	.489	.712	.948	1.000	1.000	1.000
80.00	.173	.241	.361	.579	.842	1.000	1.000	1.000
85.00	.086	.126	.203	.372	.730	.999	1.000	1.000
87.00	.051	.077	.129	.253	.576	.992	1.000	1.000
89.00	.016	.025	.045	.099	.278	.854	1.000	1.000
90.00	0.000	0.000	0.000	0.000	0.000	0.000	0.000	0.000

ESCAPING FLUXES AND SURFACE CURRENTS OF EMITTED ELECTRONS IN UNIFORM E AND B FIELDS.

86 MAY 30A , CASE 3

NALFA NPSI NTH NEPS NTAU MINT NVX NVY NVZ
1 1 19 8 90 4 64 64 32

ANGLES DEFINING ELECTRIC-FIELD DIRECTION: ALPHA = 60.000 DEGREES, PSI = 0.000 DEGREES

ESCAPING FLUXES

EPS THETA	0.00	.20	.50	1.00	2.00	5.00	10.00	20.00
-30.00	.864	.874	.887	.902	.918	.929	.932	.933
-29.00	.873	.883	.897	.915	.937	.965	.985	.998
-28.00	.881	.892	.908	.928	.953	.985	.998	1.000
-27.00	.889	.901	.918	.939	.966	.994	1.000	1.000
-24.00	.912	.925	.943	.966	.989	1.000	1.000	1.000
-21.00	.931	.946	.963	.983	.997	1.000	1.000	1.000
-18.00	.949	.962	.978	.992	1.000	1.000	1.000	1.000
-15.00	.963	.976	.988	.997	1.000	1.000	1.000	1.000
0.00	1.000	1.000	1.000	1.000	1.000	1.000	1.000	1.000
15.00	.963	.983	.994	.999	1.000	1.000	1.000	1.000
30.00	.864	.921	.963	.989	.999	1.000	1.000	1.000
45.00	.706	.799	.887	.955	.992	1.000	1.000	1.000
60.00	.499	.613	.746	.879	.973	1.000	1.000	1.000
75.00	.258	.355	.502	.702	.909	.998	1.000	1.000
80.00	.173	.251	.381	.586	.848	.997	1.000	1.000
85.00	.086	.134	.225	.397	.699	.990	1.000	1.000
87.00	.051	.083	.147	.280	.562	.971	1.000	1.000
89.00	.016	.028	.054	.116	.284	.808	.999	1.000
90.00	0.000	0.000	0.000	0.000	0.000	0.000	0.000	0.000

ESCAPING FLUXES AND SURFACE CURRENTS OF EMITTED ELECTRONS IN UNIFORM E AND B FIELDS.

86 JUL 04A , CASE 3

NALFA NPSI NTH NEPS NTAU MINT NVX NVY NVZ
1 1 24 8 90 4 64 64 32

ANGLES DEFINING ELECTRIC-FIELD DIRECTION: ALPHA = 30.000 DEGREES, PSI = 45.000 DEGREES

ESCAPING FLUXES

EPS	0.00	.20	.50	1.00	2.00	5.00	10.00	20.00
THETA								
-67.79	.377	.356	.318	.242	.102	.001	0.000	0.000
-65.00	.422	.409	.385	.331	.204	.011	0.000	0.000
-62.50	.461	.457	.445	.413	.321	.074	.001	0.000
-60.00	.499	.502	.503	.495	.451	.252	.044	.000
-57.00	.544	.556	.571	.589	.604	.582	.500	.321
-54.00	.587	.607	.634	.674	.736	.848	.945	.996
-51.00	.628	.655	.693	.749	.837	.964	.999	1.000
-48.00	.668	.701	.747	.813	.907	.995	1.000	1.000
-45.00	.706	.744	.795	.865	.951	.999	1.000	1.000
-42.00	.742	.783	.838	.906	.976	1.000	1.000	1.000
-39.00	.776	.820	.874	.937	.989	1.000	1.000	1.000
-30.00	.864	.908	.952	.987	1.000	1.000	1.000	1.000
-15.00	.963	.986	.997	1.000	1.000	1.000	1.000	1.000
0.00	1.000	1.000	1.000	1.000	1.000	1.000	1.000	1.000
15.00	.963	.989	.998	1.000	1.000	1.000	1.000	1.000
30.00	.864	.935	.980	.997	1.000	1.000	1.000	1.000
45.00	.706	.819	.922	.984	.999	1.000	1.000	1.000
60.00	.499	.638	.803	.945	.997	1.000	1.000	1.000
75.00	.258	.397	.614	.867	.992	1.000	1.000	1.000
80.00	.173	.306	.539	.834	.989	1.000	1.000	1.000
85.00	.086	.214	.471	.801	.986	1.000	1.000	1.000
87.00	.051	.182	.450	.786	.985	1.000	1.000	1.000
89.00	.016	.163	.430	.770	.983	1.000	1.000	1.000
90.00	0.000	.157	.419	.761	.981	1.000	1.000	1.000

ESCAPING FLUXES AND SURFACE CURRENTS OF EMITTED ELECTRONS IN UNIFORM E AND B FIELDS.

86 JUL 07A , CASE 3

NALFA NPSI NTH NEPS NTAU MINT NVX NVY NVZ
1 1 20 8 90 4 64 64 32

ANGLES DEFINING ELECTRIC-FIELD DIRECTION: ALPHA = 60.000 DEGREES, PSI = 45.000 DEGREES

ESCAPING FLUXES

EPS	0.00	.20	.50	1.00	2.00	5.00	10.00	20.00
THETA								
-39.23	.773	.755	.724	.658	.489	.074	.000	0.000
-36.00	.808	.798	.781	.744	.645	.279	.015	0.000
-33.00	.837	.834	.828	.814	.773	.587	.247	.008
-30.00	.864	.867	.869	.872	.872	.853	.803	.672
-27.00	.889	.896	.905	.918	.938	.973	.994	1.000
-24.00	.912	.921	.934	.952	.976	.998	1.000	1.000
-21.00	.931	.943	.957	.975	.993	1.000	1.000	1.000
-18.00	.949	.960	.974	.989	.998	1.000	1.000	1.000
-15.00	.963	.974	.986	.996	1.000	1.000	1.000	1.000
0.00	1.000	1.000	1.000	1.000	1.000	1.000	1.000	1.000
15.00	.963	.984	.995	.999	1.000	1.000	1.000	1.000
30.00	.864	.927	.971	.993	.999	1.000	1.000	1.000
45.00	.706	.816	.914	.975	.996	1.000	1.000	1.000
60.00	.499	.653	.819	.943	.992	1.000	1.000	1.000
75.00	.258	.441	.690	.899	.986	1.000	1.000	1.000
80.00	.173	.364	.644	.882	.984	1.000	1.000	1.000
85.00	.086	.292	.602	.863	.982	1.000	1.000	1.000
87.00	.051	.270	.585	.854	.981	1.000	1.000	1.000
89.00	.016	.254	.566	.845	.980	1.000	1.000	1.000
90.00	0.000	.246	.556	.841	.979	1.000	1.000	1.000

ESCAPING FLUXES AND SURFACE CURRENTS OF EMITTED ELECTRONS IN UNIFORM E AND B FIELDS.

86 JUN 24A , CASE 3

NALFA NPSI NTH NEPS NTAU MINT NVX NVY NVZ
1 1 28 8 90 4 64 64 32

ANGLES DEFINING ELECTRIC-FIELD DIRECTION: ALPHA = 30.000 DEGREES, PSI = 90.000 DEGREES

ESCAPING FLUXES

EPS	0.00	.20	.50	1.00	2.00	5.00	10.00	20.00
THETA								
-90.00	.004	0.000	0.000	0.000	0.000	0.000	0.000	0.000
-89.00	.016	0.000	0.000	0.000	0.000	0.000	0.000	0.000
-87.00	.051	.004	0.000	0.000	0.000	0.000	0.000	0.000
-85.00	.086	.027	.002	0.000	0.000	0.000	0.000	0.000
-80.00	.173	.118	.055	.009	0.000	0.000	0.000	0.000
-75.00	.258	.222	.167	.089	.014	0.000	0.000	0.000
-72.00	.308	.284	.245	.178	.072	.001	0.000	0.000
-69.00	.358	.346	.325	.284	.194	.028	0.000	0.000
-66.00	.406	.406	.403	.393	.358	.222	.062	.001
-63.00	.453	.464	.479	.499	.529	.579	.630	.710
-60.00	.499	.520	.550	.596	.677	.849	.973	1.000
-55.00	.573	.607	.657	.731	.848	.987	1.000	1.000
-50.00	.642	.687	.748	.832	.937	.999	1.000	1.000
-45.00	.706	.758	.823	.902	.978	1.000	1.000	1.000
-40.00	.765	.819	.882	.947	.993	1.000	1.000	1.000
-30.00	.864	.914	.959	.990	1.000	1.000	1.000	1.000
-15.00	.963	.986	.997	1.000	1.000	1.000	1.000	1.000
0.00	1.000	1.000	1.000	1.000	1.000	1.000	1.000	1.000
15.00	.963	.988	.998	1.000	1.000	1.000	1.000	1.000
30.00	.864	.932	.978	.997	1.000	1.000	1.000	1.000
45.00	.706	.809	.912	.981	.999	1.000	1.000	1.000
60.00	.499	.624	.784	.936	.997	1.000	1.000	1.000
75.00	.258	.392	.608	.871	.994	1.000	1.000	1.000
80.00	.173	.311	.557	.860	.993	1.000	1.000	1.000
85.00	.086	.238	.534	.858	.992	1.000	1.000	1.000
87.00	.051	.220	.534	.857	.992	1.000	1.000	1.000
89.00	.016	.217	.535	.857	.992	1.000	1.000	1.000
90.00	0.000	.217	.534	.858	.992	1.000	1.000	1.000

ESCAPING FLUXES AND SURFACE CURRENTS OF EMITTED ELECTRONS IN UNIFORM E AND B FIELDS.

86 JUN 24A , CASE 6

NALFA NPSI NTH NEPS NTAU MINT NVX NVY NVZ
1 1 30 8 90 4 64 64 32

ANGLES DEFINING ELECTRIC-FIELD DIRECTION: ALPHA = 60.000 DEGREES, PSI = 90.000 DEGREES

ESCAPING FLUXES

EPS	0.00	.20	.50	1.00	2.00	5.00	10.00	20.00
THETA								
-90.00	.004	0.000	0.000	0.000	0.000	0.000	0.000	0.000
-89.00	.016	0.000	0.000	0.000	0.000	0.000	0.000	0.000
-87.00	.051	.000	0.000	0.000	0.000	0.000	0.000	0.000
-85.00	.086	.006	0.000	0.000	0.000	0.000	0.000	0.000
-80.00	.173	.066	.007	0.000	0.000	0.000	0.000	0.000
-75.00	.258	.156	.055	.004	0.000	0.000	0.000	0.000
-70.00	.341	.254	.143	.037	.001	0.000	0.000	0.000
-65.00	.422	.353	.254	.122	.013	0.000	0.000	0.000
-60.00	.499	.449	.371	.249	.079	.000	0.000	0.000
-55.00	.573	.539	.487	.397	.227	.011	0.000	0.000
-50.00	.642	.624	.596	.544	.430	.138	.004	0.000
-45.00	.706	.701	.693	.676	.634	.479	.228	.016
-42.00	.742	.743	.745	.744	.738	.699	.615	.425
-39.00	.776	.783	.792	.804	.822	.859	.901	.954
-36.00	.808	.819	.834	.854	.887	.947	.988	1.000
-33.00	.837	.852	.871	.896	.933	.985	.999	1.000
-30.00	.864	.881	.902	.929	.964	.997	1.000	1.000
-27.00	.889	.907	.929	.954	.983	1.000	1.000	1.000
-15.00	.963	.977	.988	.997	1.000	1.000	1.000	1.000
0.00	1.000	1.000	1.000	1.000	1.000	1.000	1.000	1.000
15.00	.963	.983	.994	.999	1.000	1.000	1.000	1.000
30.00	.864	.919	.965	.992	.999	1.000	1.000	1.000
45.00	.706	.799	.896	.970	.997	1.000	1.000	1.000
60.00	.499	.631	.793	.937	.993	1.000	1.000	1.000
75.00	.258	.436	.692	.914	.990	1.000	1.000	1.000
80.00	.173	.375	.679	.912	.989	1.000	1.000	1.000
85.00	.086	.335	.678	.910	.989	1.000	1.000	1.000
87.00	.051	.332	.678	.910	.989	1.000	1.000	1.000
89.00	.016	.333	.678	.910	.989	1.000	1.000	1.000
90.00	0.000	.333	.679	.910	.989	1.000	1.000	1.000

ESCAPING FLUXES AND SURFACE CURRENTS OF EMITTED ELECTRONS IN UNIFORM E AND B FIELDS.

86 JUL 11A , CASE 3

NALFA NPSI NTH NEPS NTAU MINT NVX NVY NVZ
1 1 21 8 90 4 64 64 32

ANGLES DEFINING ELECTRIC-FIELD DIRECTION: ALPHA = 30.000 DEGREES, PSI = 135.000 DEGREES

ESCAPING FLUXES

EPS	0.00	.20	.50	1.00	2.00	5.00	10.00	20.00
THETA								
-90.00	.004	0.000	0.000	0.000	0.000	0.000	0.000	0.000
-89.00	.016	.000	0.000	0.000	0.000	0.000	0.000	0.000
-87.00	.051	.015	.001	0.000	0.000	0.000	0.000	0.000
-85.00	.086	.052	.019	.002	0.000	0.000	0.000	0.000
-82.50	.130	.106	.074	.034	.003	0.000	0.000	0.000
-80.00	.173	.163	.146	.115	.061	.002	0.000	0.000
-77.50	.216	.219	.222	.223	.214	.158	.070	.006
-75.00	.258	.274	.297	.334	.405	.598	.836	.991
-72.50	.300	.327	.368	.438	.576	.880	.997	1.000
-70.00	.341	.379	.436	.531	.707	.971	1.000	1.000
-65.00	.422	.477	.558	.682	.865	.998	1.000	1.000
-60.00	.499	.567	.661	.790	.939	1.000	1.000	1.000
-45.00	.706	.785	.871	.951	.995	1.000	1.000	1.000
-30.00	.864	.924	.969	.994	1.000	1.000	1.000	1.000
-15.00	.963	.987	.997	1.000	1.000	1.000	1.000	1.000
0.00	1.000	1.000	1.000	1.000	1.000	1.000	1.000	1.000
15.00	.963	.987	.998	1.000	1.000	1.000	1.000	1.000
30.00	.864	.922	.970	.995	1.000	1.000	1.000	1.000
45.00	.706	.783	.874	.959	.998	1.000	1.000	1.000
60.00	.499	.579	.691	.841	.976	1.000	1.000	1.000
67.79	.377	.454	.571	.747	.945	1.000	1.000	1.000

ESCAPING FLUXES AND SURFACE CURRENTS OF EMITTED ELECTRONS IN UNIFORM E AND B FIELDS.

86 JUL 15A , CASE 3

NALFA NPSI NTH NEPS NTAU MINT NVX NVY NVZ
1 1 20 8 90 4 64 64 32

ANGLES DEFINING ELECTRIC-FIELD DIRECTION: ALPHA = 60.000 DEGREES, PSI = 135.000 DEGREES

ESCAPING FLUXES

EPS	0.00	.20	.50	1.00	2.00	5.00	10.00	20.00
THETA								
-90.00	.004	0.000	0.000	0.000	0.000	0.000	0.000	0.000
-89.00	.016	0.000	0.000	0.000	0.000	0.000	0.000	0.000
-87.00	.051	.003	0.000	0.000	0.000	0.000	0.000	0.000
-85.00	.086	.026	.002	0.000	0.000	0.000	0.000	0.000
-80.00	.173	.126	.071	.021	.001	0.000	0.000	0.000
-75.00	.258	.235	.202	.150	.073	.003	0.000	0.000
-72.00	.308	.299	.284	.257	.201	.073	.006	0.000
-69.00	.358	.361	.364	.364	.355	.302	.205	.070
-66.00	.406	.421	.439	.463	.500	.573	.659	.791
-63.00	.453	.477	.508	.552	.622	.769	.911	.994
-60.00	.499	.531	.572	.629	.719	.882	.982	1.000
-57.00	.544	.581	.630	.696	.793	.942	.997	1.000
-54.00	.587	.629	.683	.753	.850	.972	.999	1.000
-45.00	.706	.755	.811	.876	.947	.997	1.000	1.000
-30.00	.864	.904	.941	.973	.995	1.000	1.000	1.000
-15.00	.963	.980	.992	.998	1.000	1.000	1.000	1.000
0.00	1.000	1.000	1.000	1.000	1.000	1.000	1.000	1.000
15.00	.963	.980	.992	.999	1.000	1.000	1.000	1.000
30.00	.864	.898	.937	.975	.998	1.000	1.000	1.000
39.23	.773	.813	.864	.925	.982	1.000	1.000	1.000

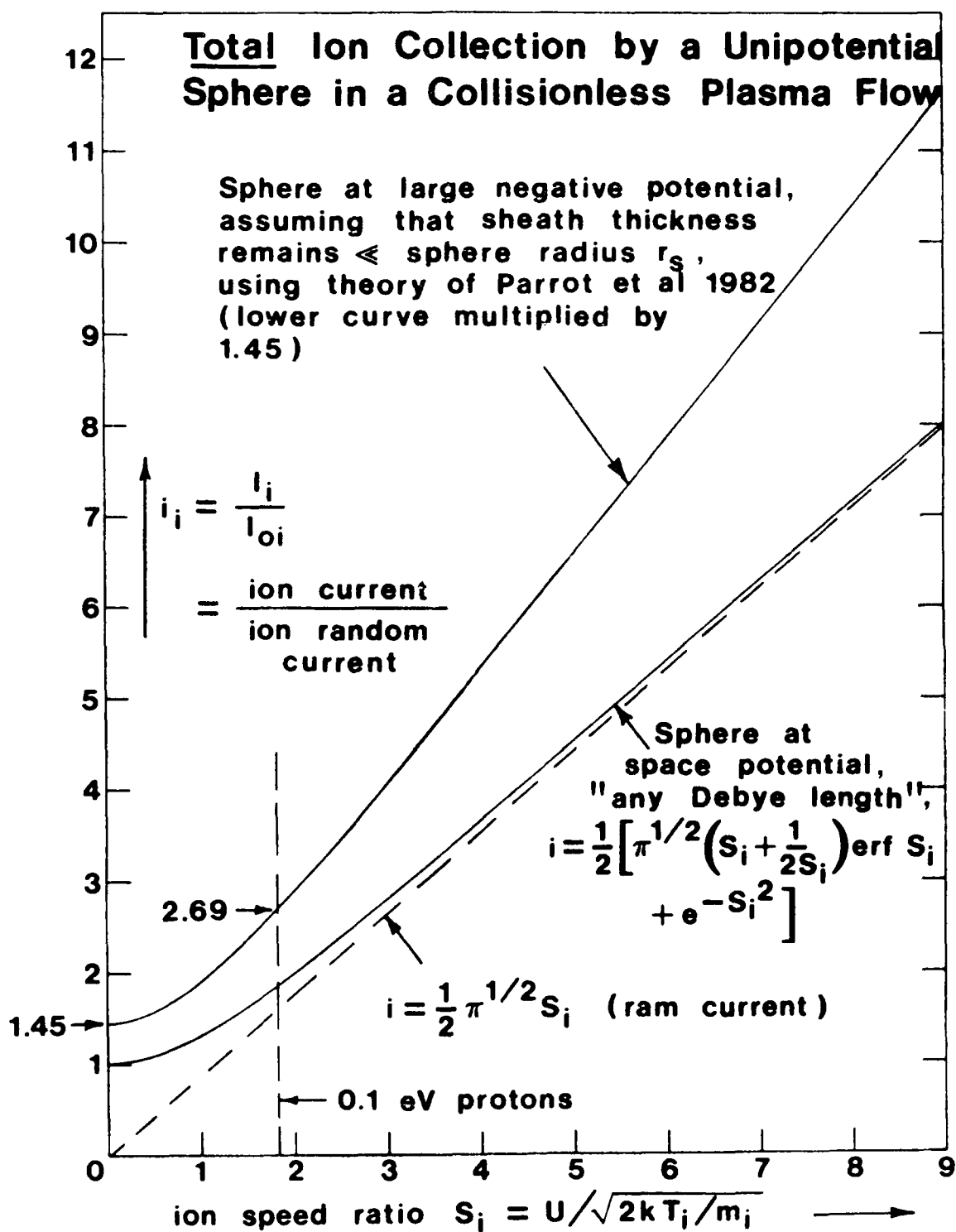


Figure 2.1. Dependence of ion current to a sphere on ion speed ratio.

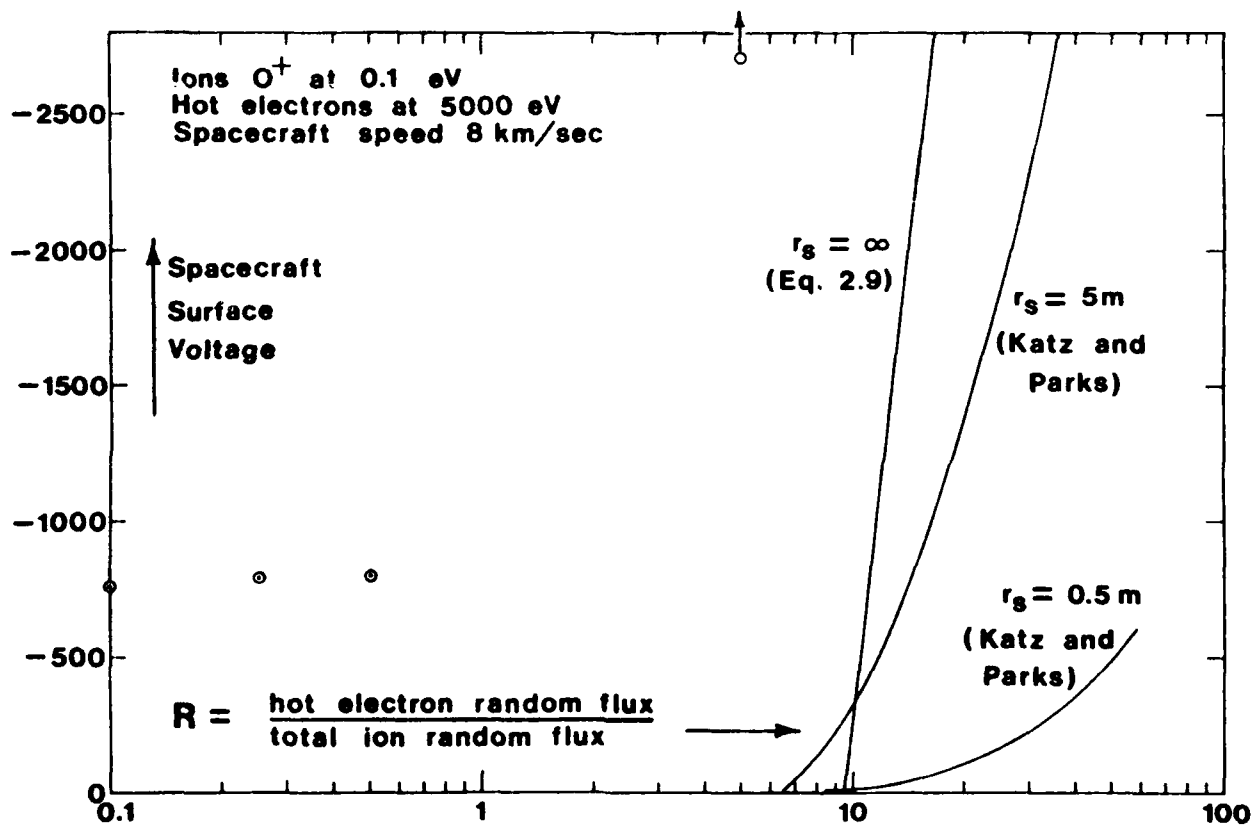


Figure 2.2. Dependence of spacecraft surface potential on hot electron/total ion ambient flux ratio. The four circled points are the largest values of surface potential from the numerical solutions discussed in Sec. 5 and presented in Fig. 5.4.

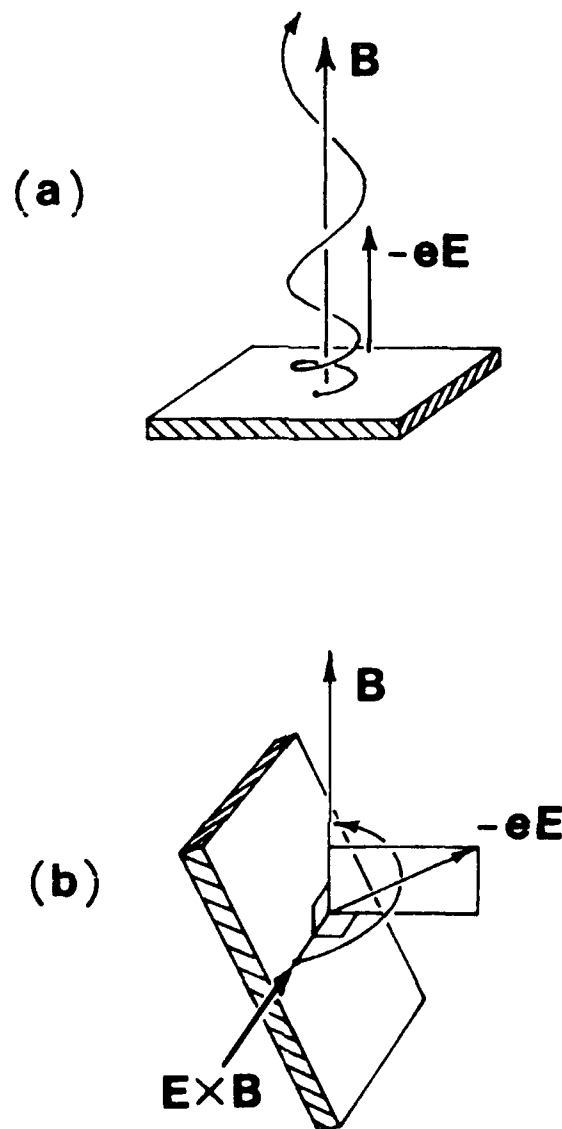


Figure 3.1. Effect of surface orientation on escape of emitted electrons. In (a), the spacecraft surface is perpendicular to the magnetic field B , and the emitted electrons, which experience an electric force $-eE$ directed away from the surface, all escape. In (b), the spacecraft surface is nearly parallel to B , and almost all of the emitted electrons return to the surface, even though they still experience an electric force directed away from it. Note that the component of E perpendicular to B results only in an $E \times B$ drift parallel to the surface.

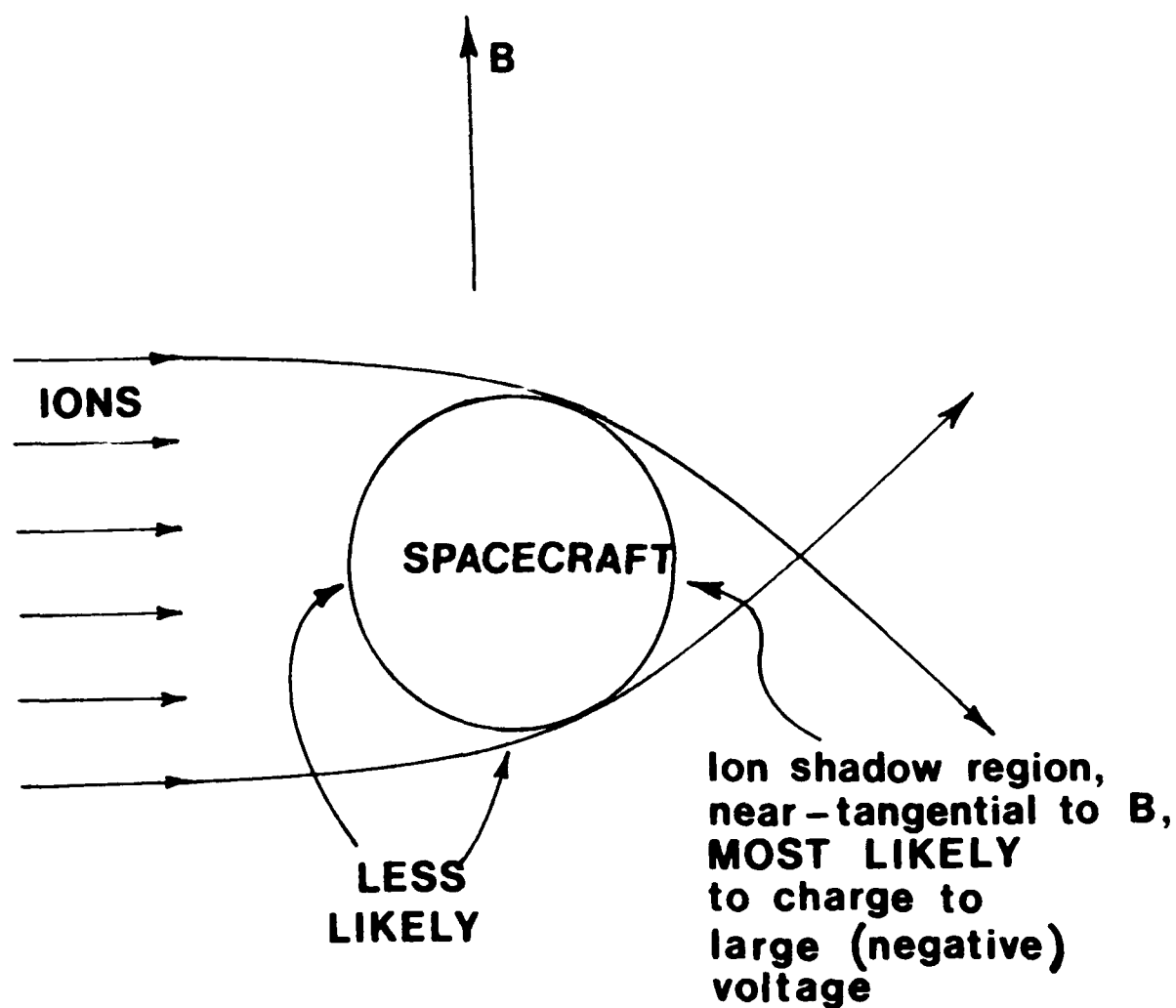


Figure 3.2. Most probable high-voltage charging locations for a nonconductive spacecraft in low-polar-orbit (auroral-plasma) conditions.

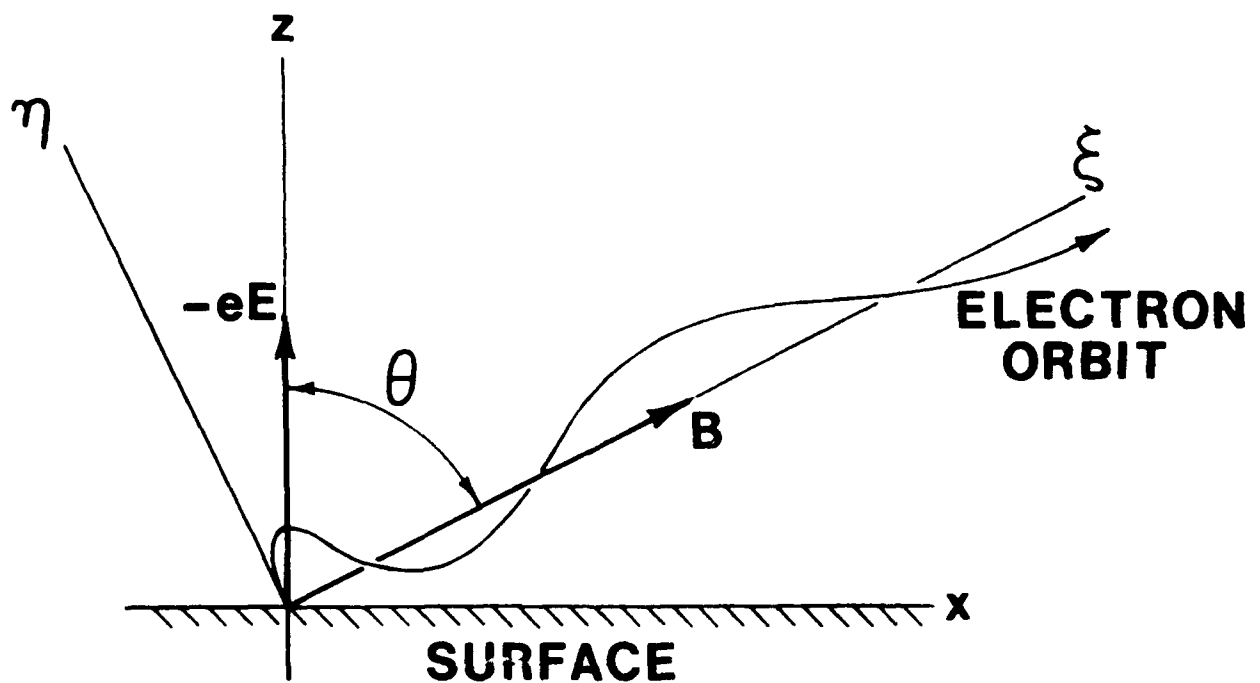


Figure 3.3. Coordinate system for calculating electron escape fluxes when E is perpendicular to the spacecraft surface. The y-coordinate (not shown) is directed into the plane of the Figure.

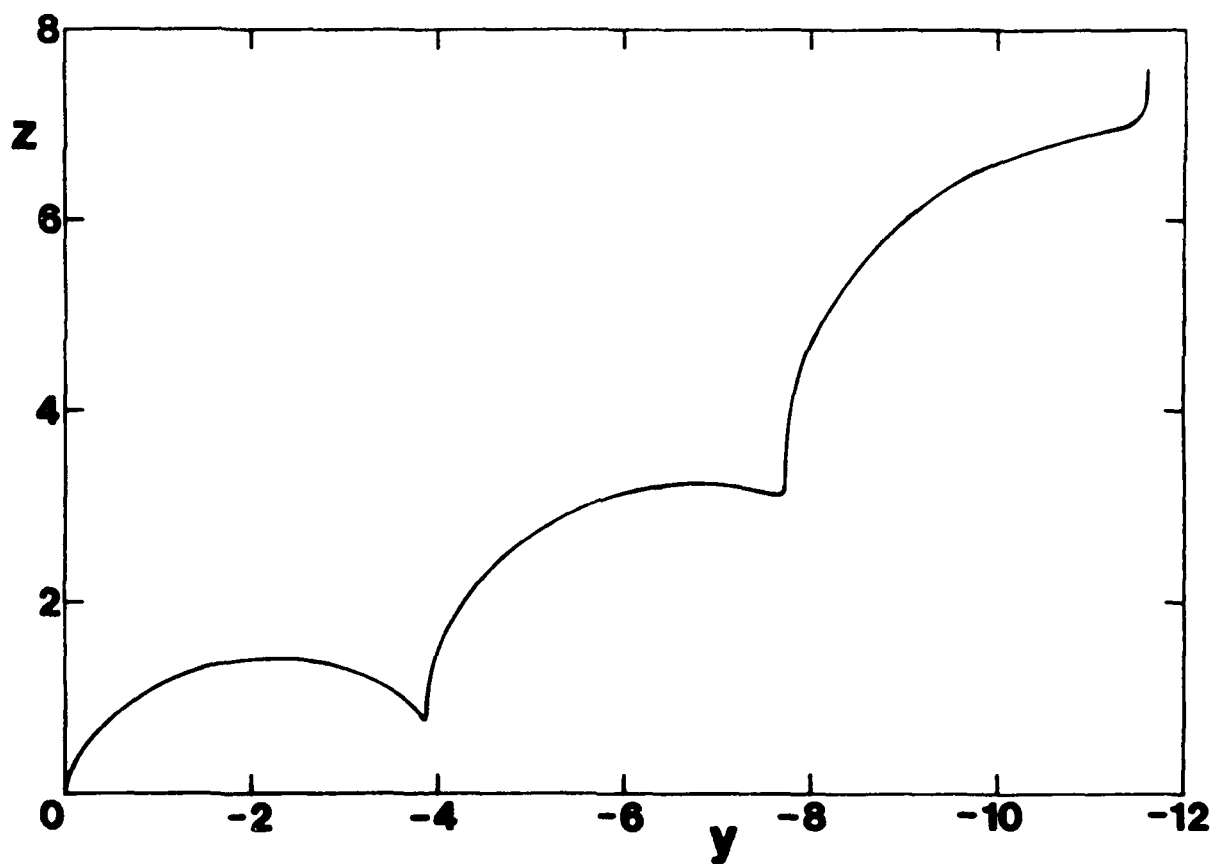


Figure 3.4. Example of an electron orbit having zero initial velocity. The magnetic field \mathbf{B} is parallel to the (x,z) plane, and makes an angle $\theta = 75^\circ$ with the z axis. $\epsilon = 1$. Three gyroperiods of the orbit ($0 \leq \tau \leq 6\pi$) are shown.

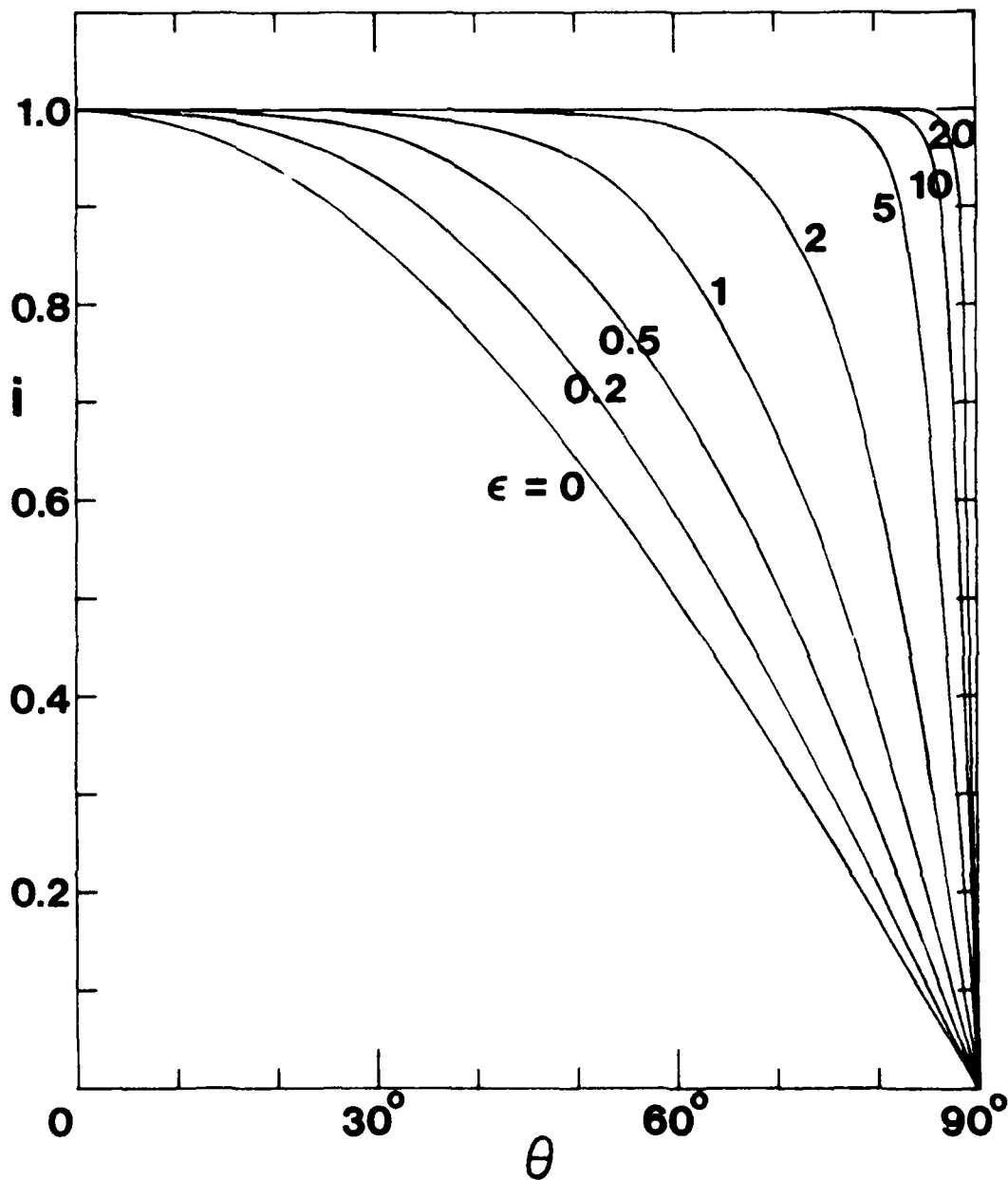


Figure 3.5. Ratio $i = I/I_0$ of escaping to emitted electron flux, as a function of the angle θ between the surface normal and the magnetic-field direction, for various values of the repelling electric field strength parameter $\epsilon = (E/B) (\pi m/2kT)^{1/2}$. The electric field is normal to the surface. The result for $\epsilon = 0$ is given by $i = \cos \theta$. Values of i plotted in this graph are also given in the first section of Table 2, labeled "ALPHA = 0.00 DEGREES, PSI = 0.00 DEGREES". Realistic values of ϵ for Shuttle high-voltage charging conditions are in the range $30 \leq \epsilon \leq 160$ (Sec. 3.2)!

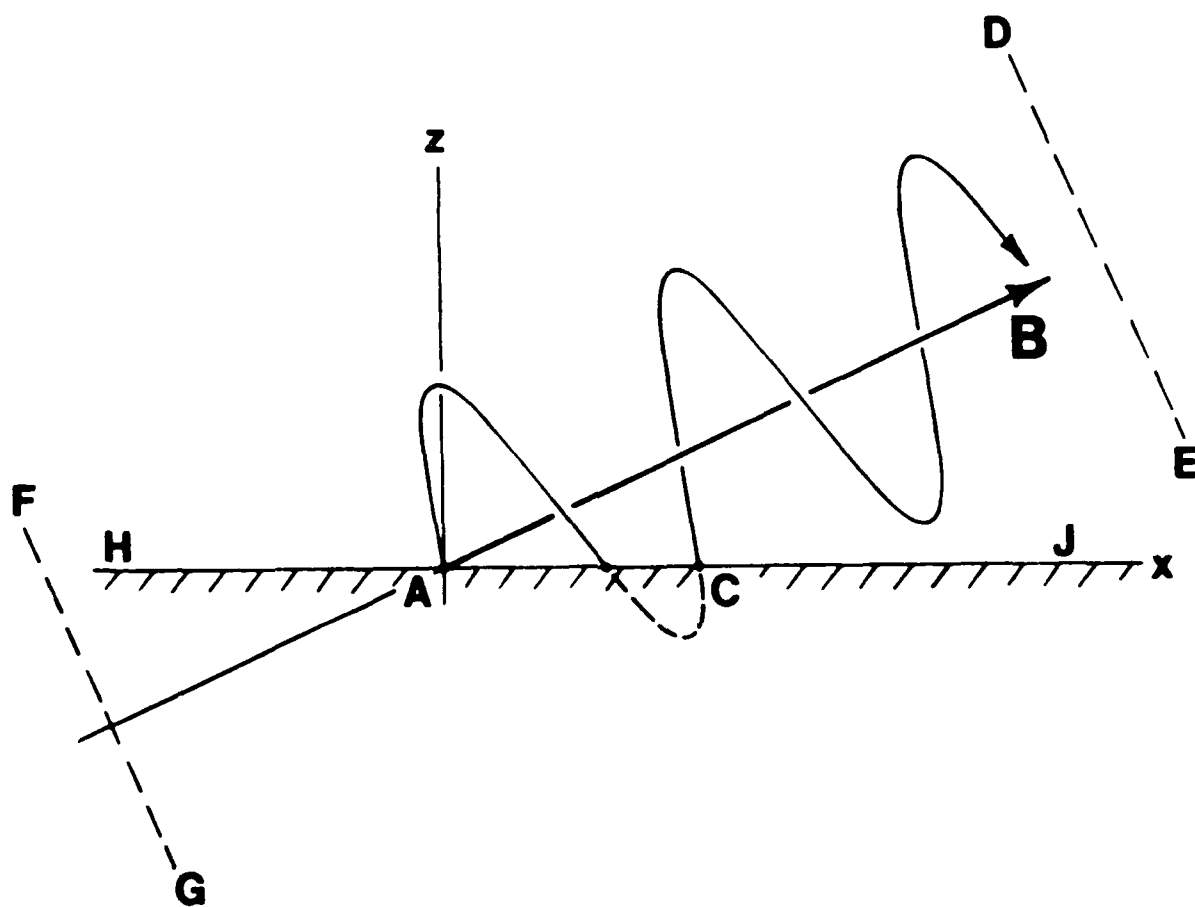


Figure 3.6. Electron orbit for $c = 0$, fictitiously extended so as to pass through the surface and re-emerge from it.

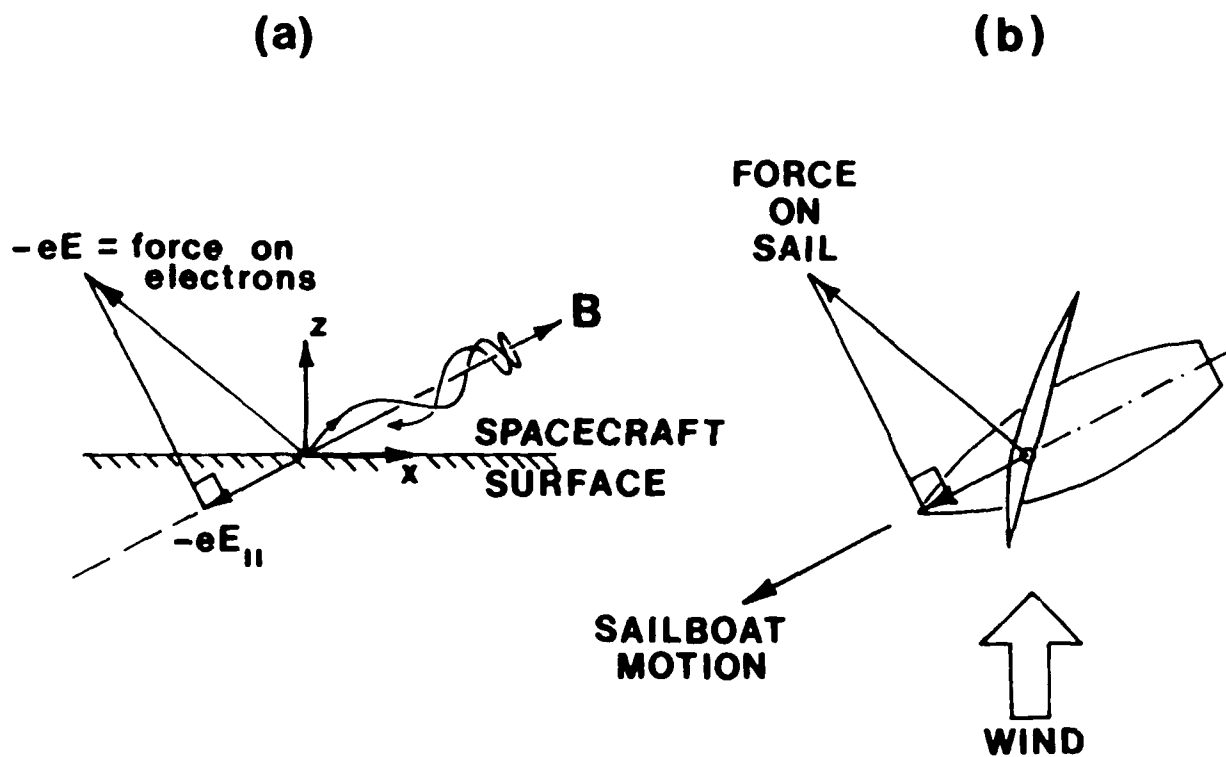


Figure 3.8. (a) Typical orbit of emitted electron when the electric force $-\mathbf{eE}$ on it has an outward normal component, but the projection of $-\mathbf{eE}$ along \mathbf{B} has an inward normal component (b) analogous situation involving sailboat tacking into wind.

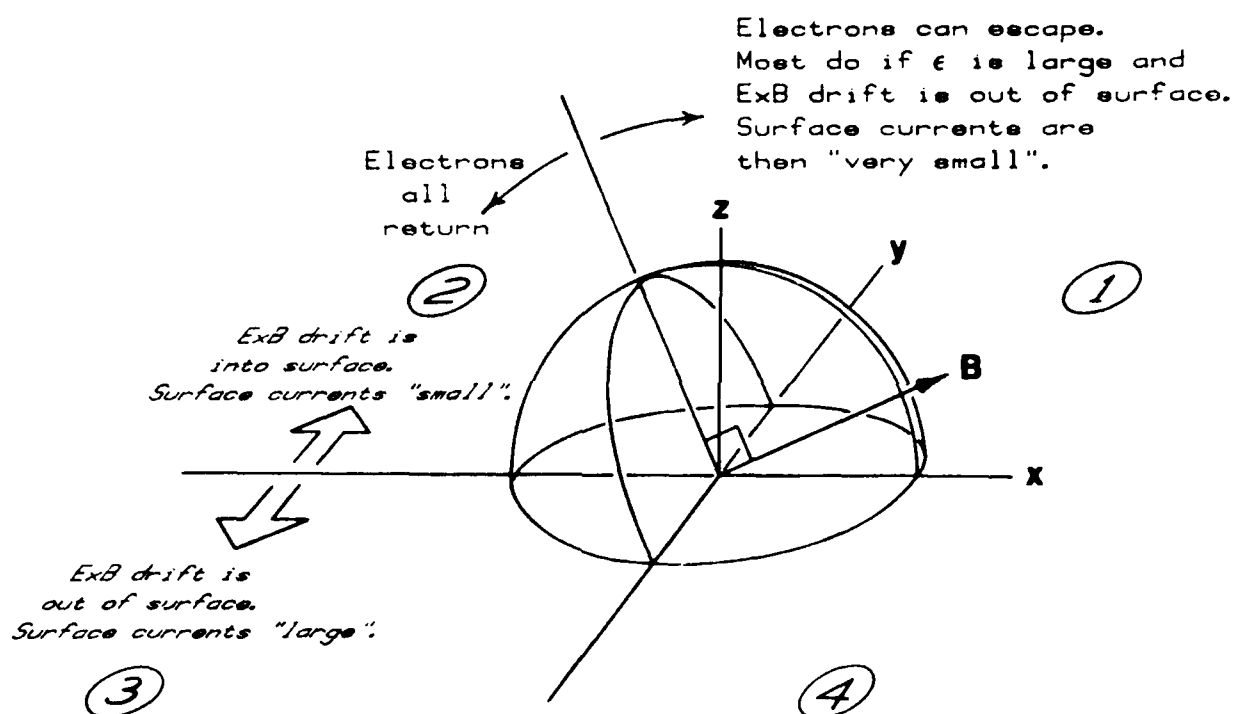
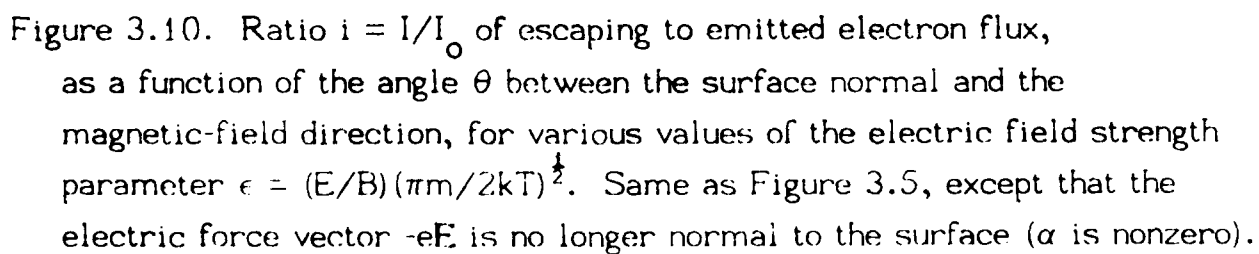


Figure 3.9. Dependence of electron escape and surface currents on electric field direction at surface.



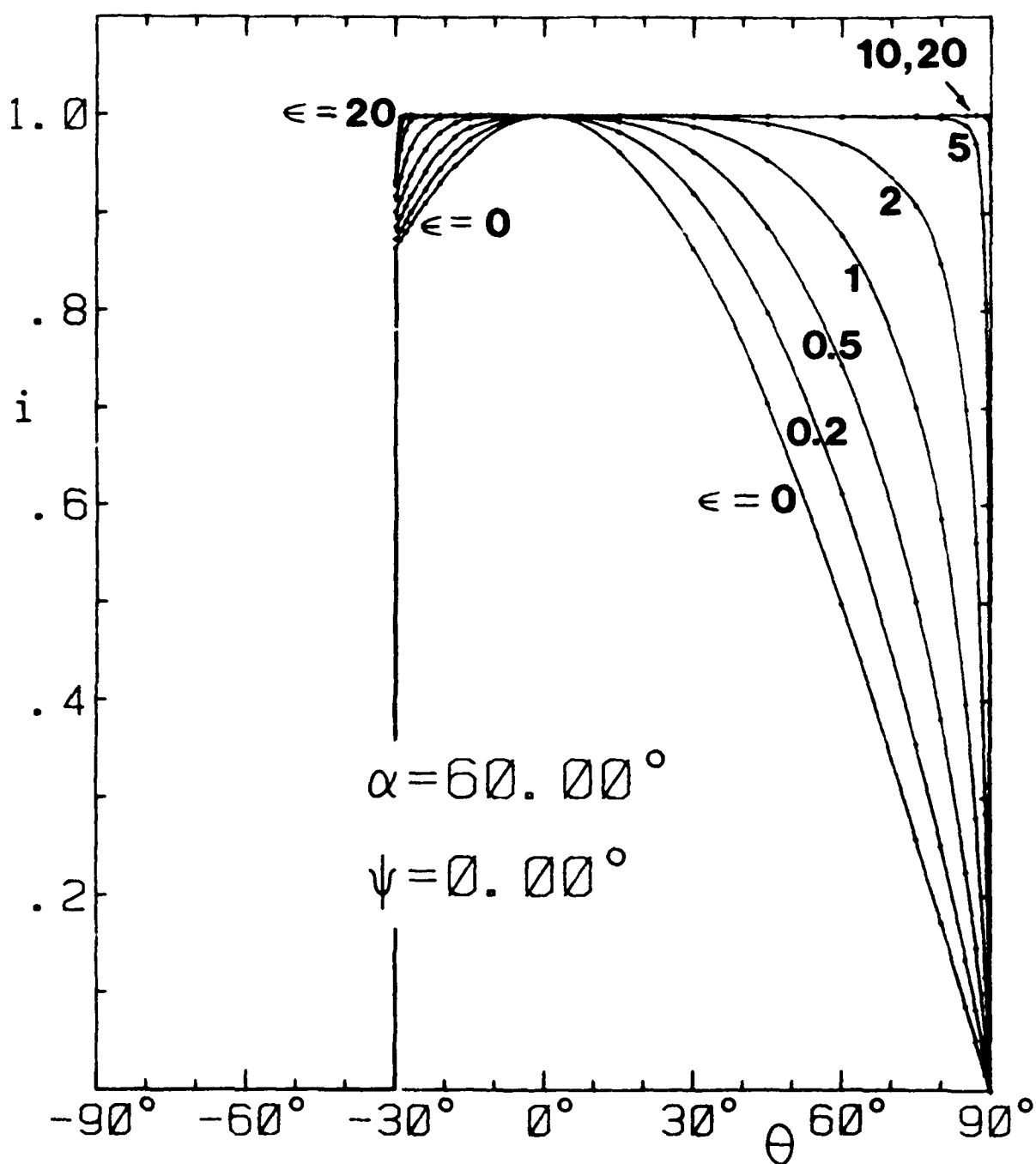


Figure 3.11. Same as figure 3.10, except that $-eE$ is tilted further away from the surface normal ($\alpha = 60^\circ$).

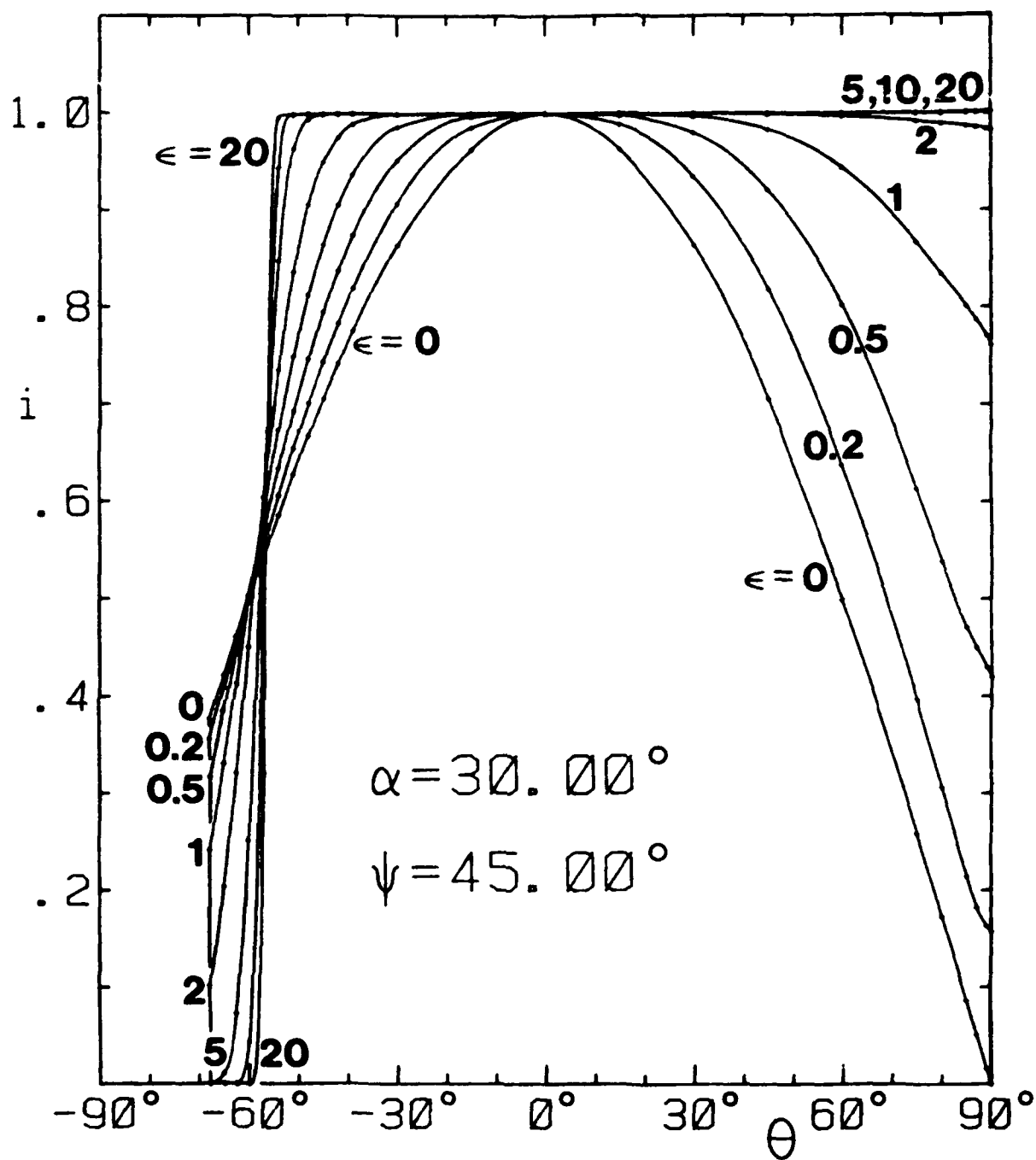


Figure 3.12. Same as Figure 3.10, except that $-eE$ is no longer in the same plane as the surface normal and the magnetic field vector (ψ is nonzero).

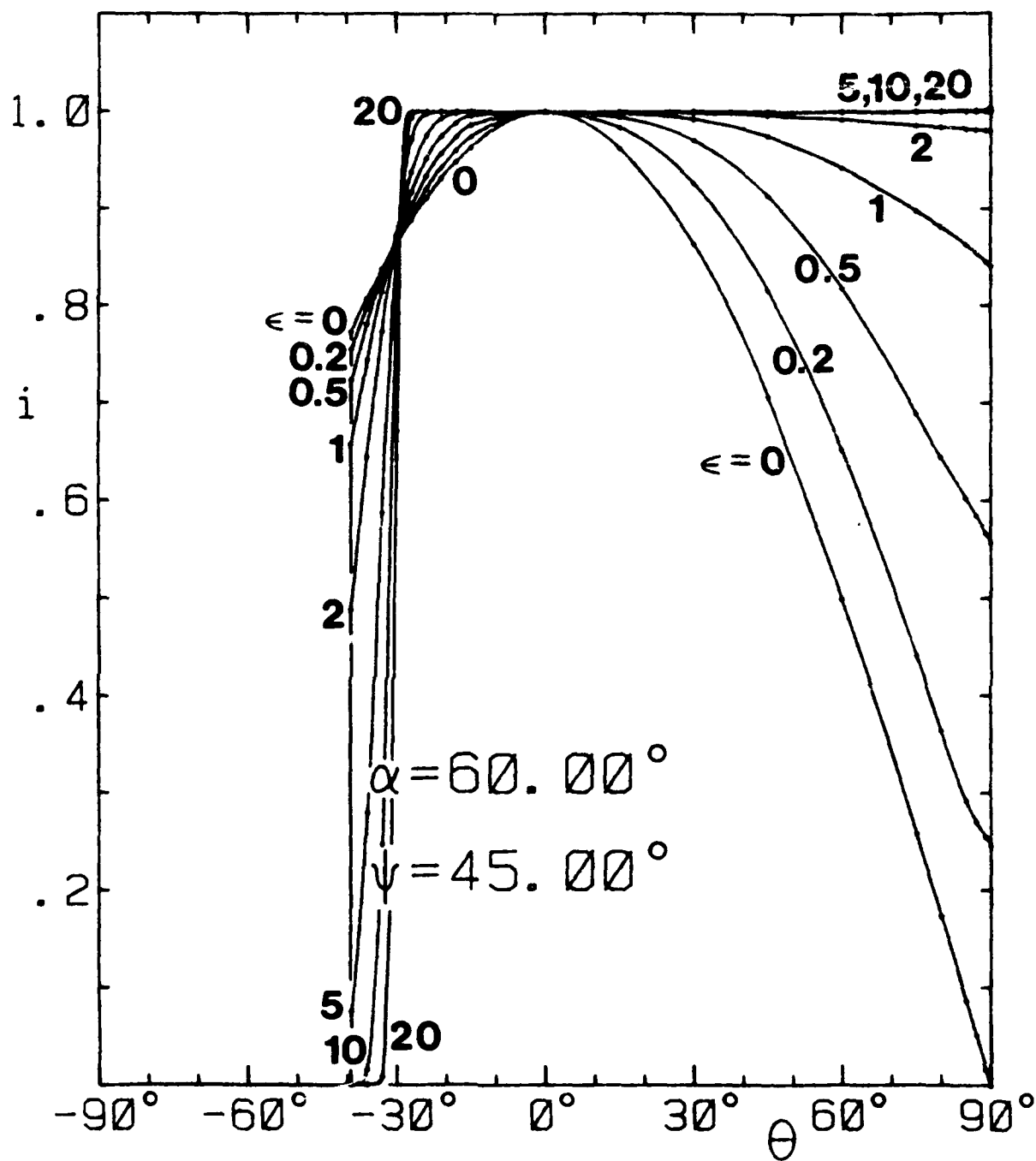


Figure 3.13. Same as Figure 3.12, except that $-eE$ is tilted further away from the surface normal.

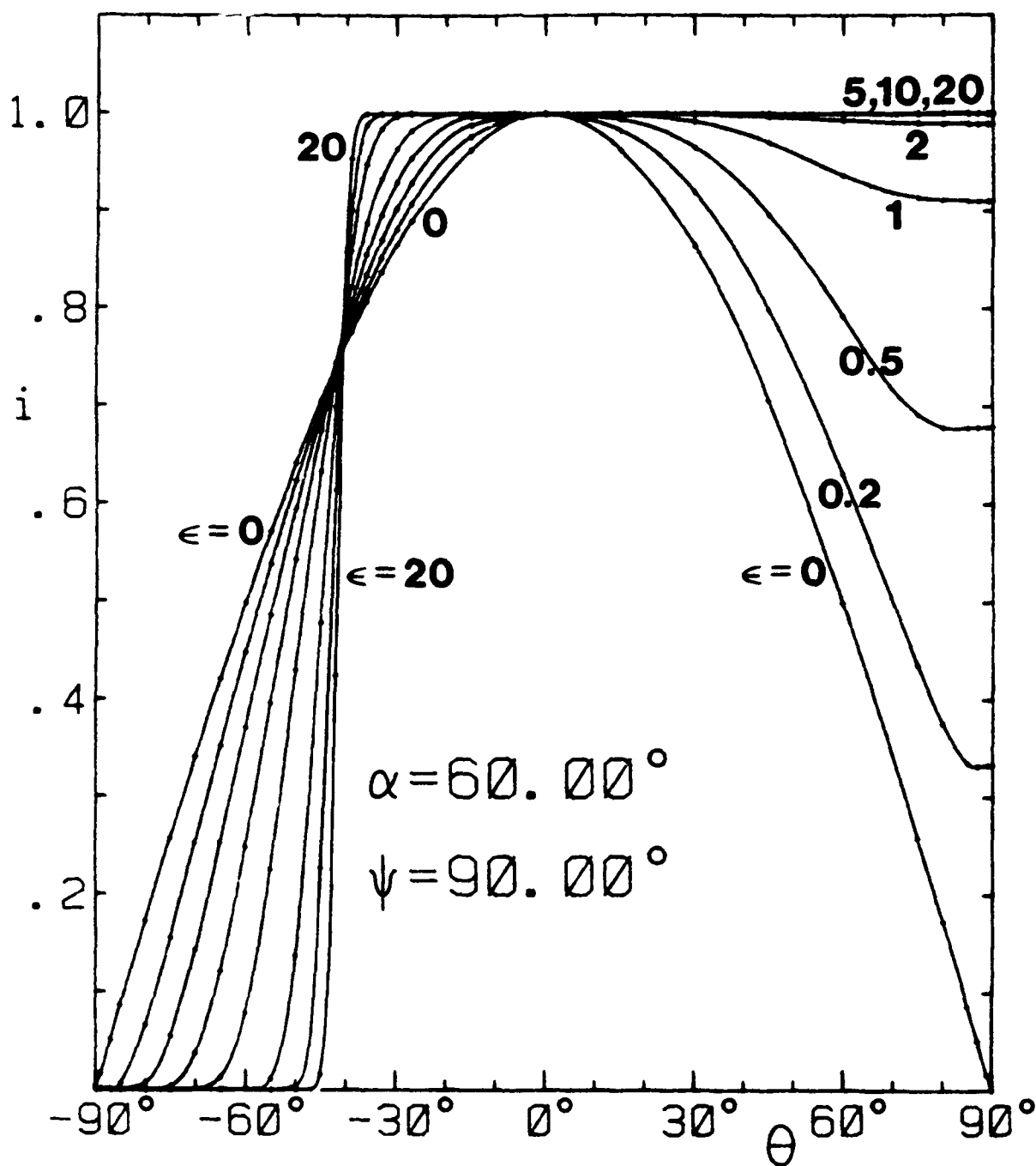


Figure 3.15. Same as Figure 3.14, except that $-eE$ is tilted further away from the surface normal.

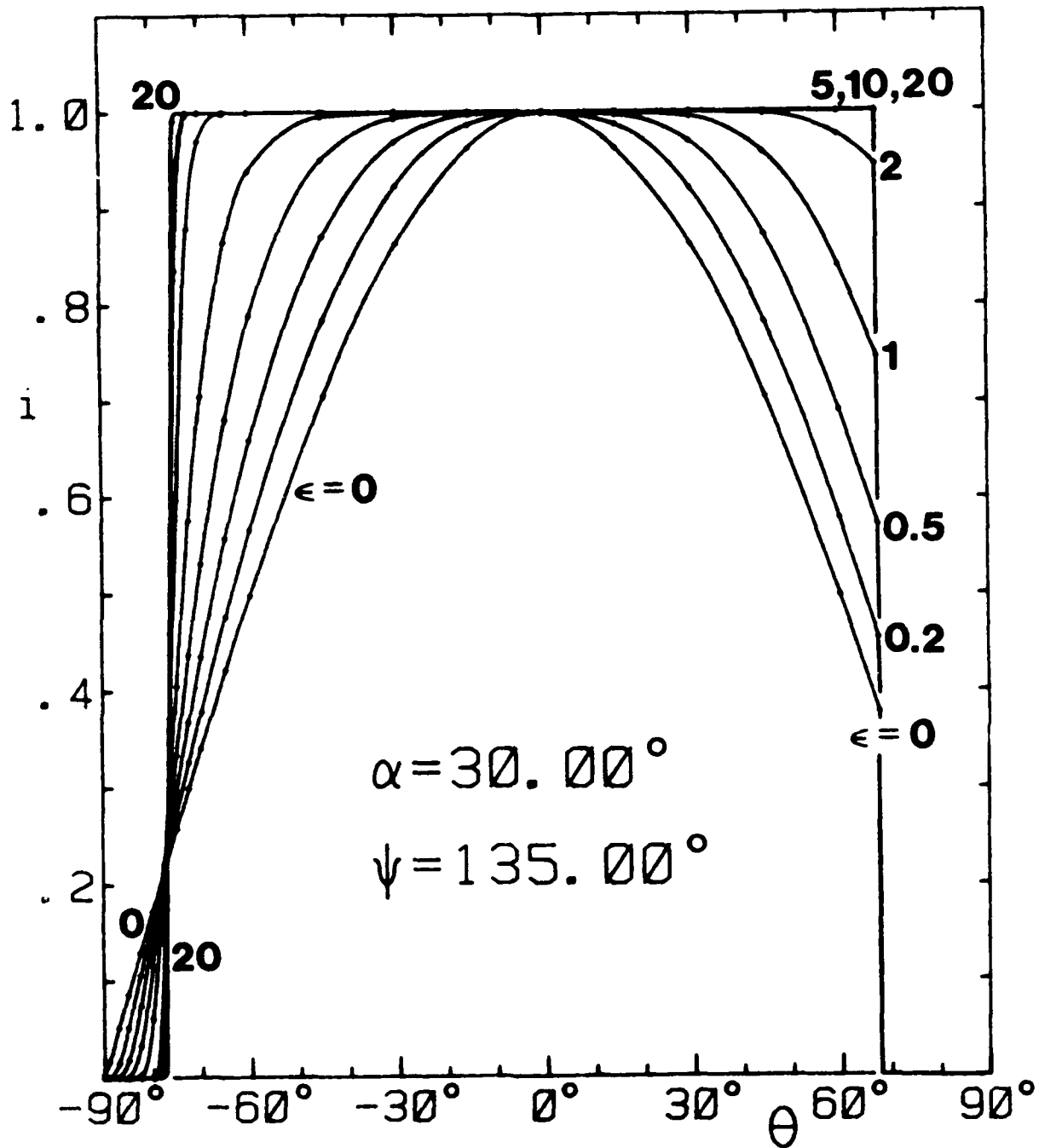


Figure 3.16. Same as Figures 3.10, 3.12, and 3.14, except that $\psi = 135^\circ$.

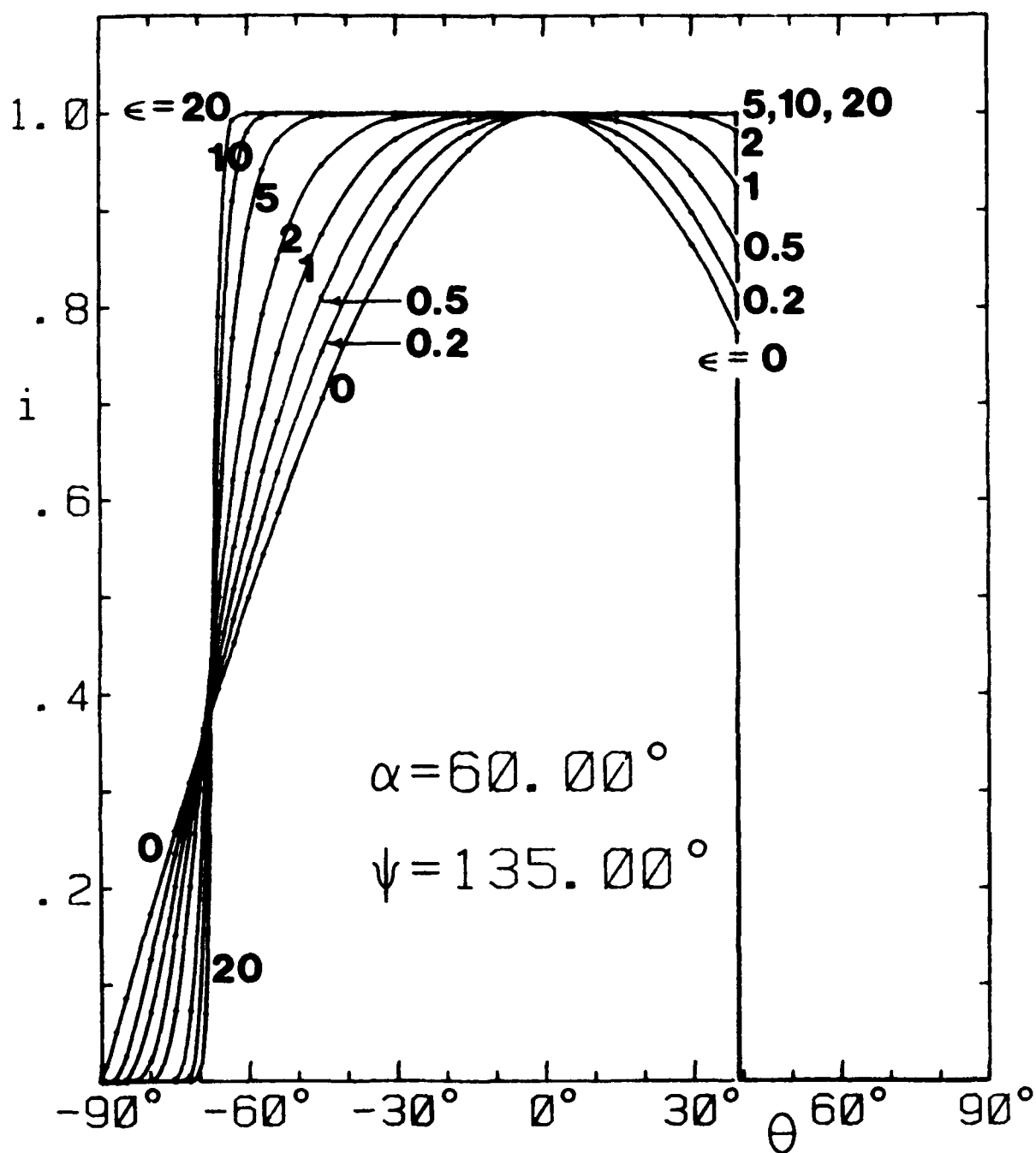


Figure 3.17. Same as Figure 3.16, except that $-eE$ is tilted further away from the surface normal.

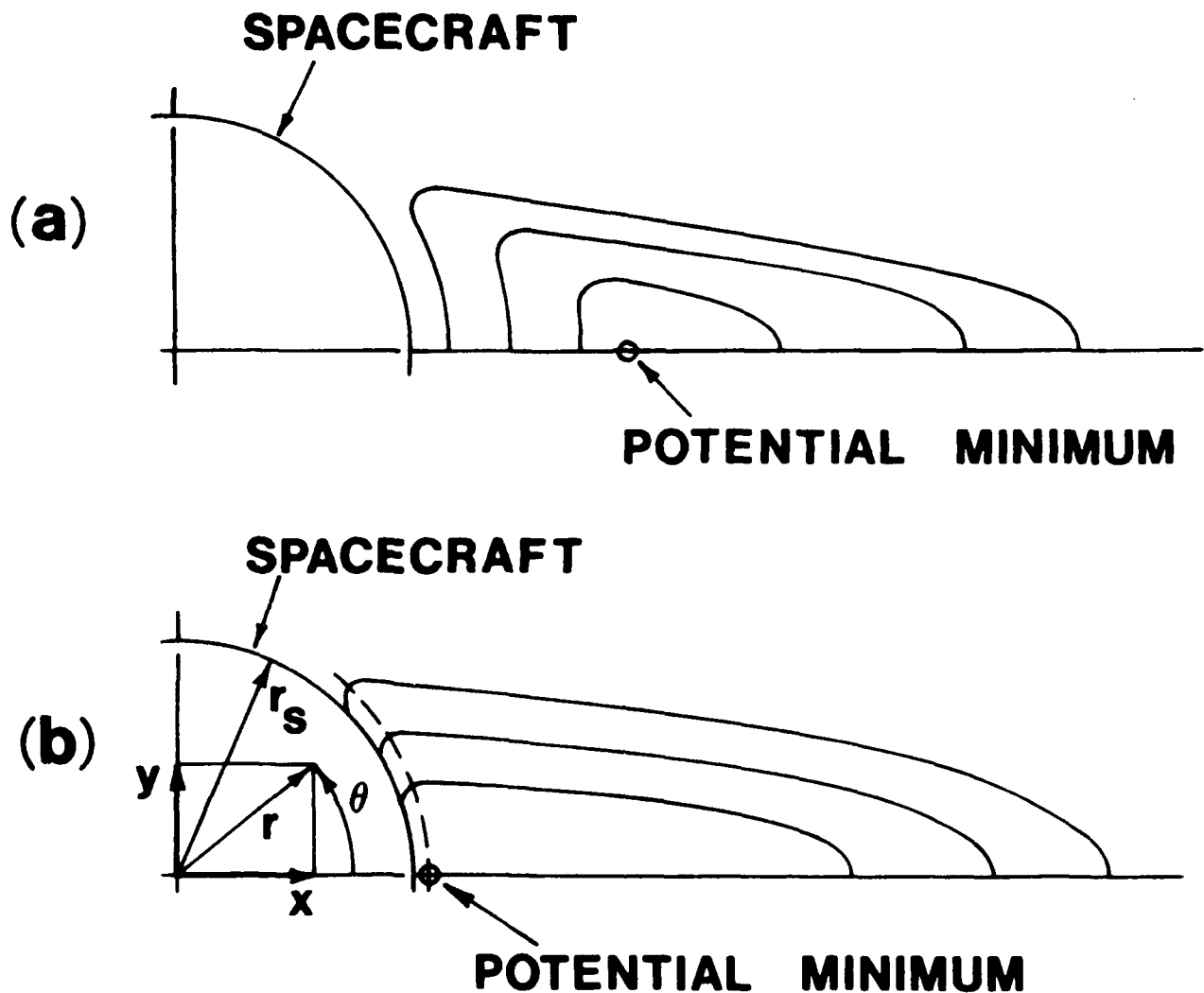


Figure 4.1.(a) General appearance of equipotentials in the near-wake region downstream of a conductive cylinder in a collisionless plasma crossflow with a large ion speed ratio S_1 and a large ratio of cylinder radius to Debye length.

(b) Same situation except that the cylinder is dielectric and emits secondary electrons and/or photoelectrons. In (b) the dotted curve is the locus of most-negative potentials along surface normals (the negative "ridge" mentioned in Sec. 4.2).

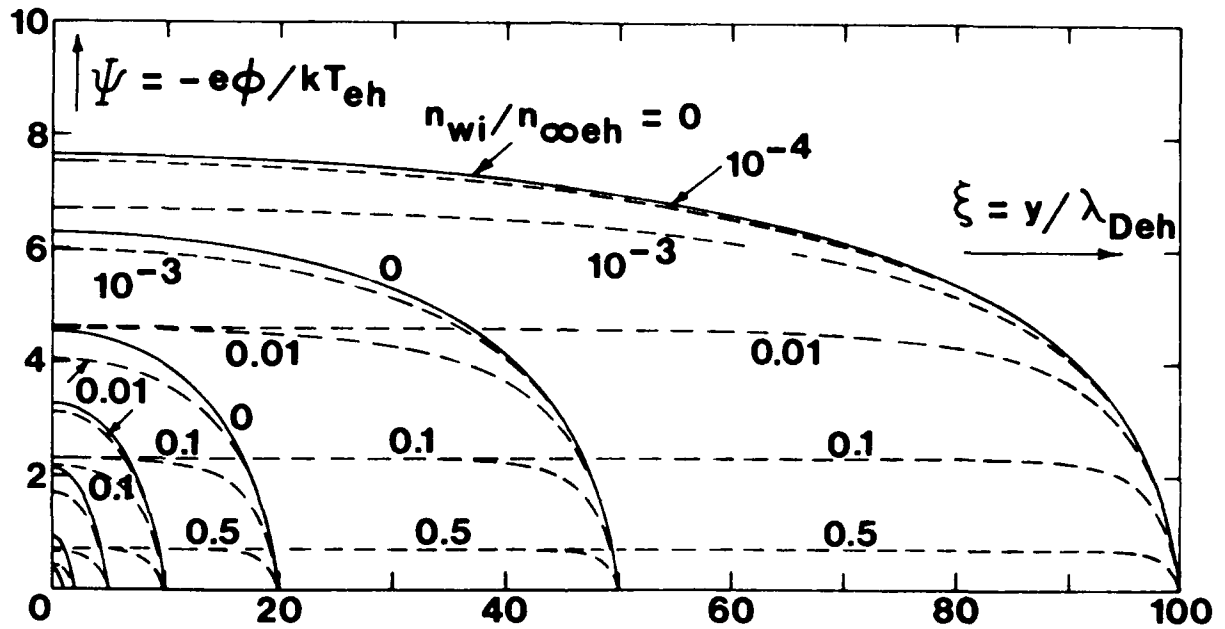


Figure 4.2. Normalized wake potential $\Psi = -e\phi/kT_{eh}$ vs normalized distance $\xi = y/\lambda_{Deh}$ from the wake centerline, as given by solutions of Eqs. (4.5) and (4.13) for various values of the normalized wake half-width ξ_{max} given by the intercepts of these curves with the ξ axis. The solid curves are for normalized wake ion density $n_{wi}/n_{\infty eh}$ equal to zero. The dotted curves are for nonzero values of this quantity as shown.

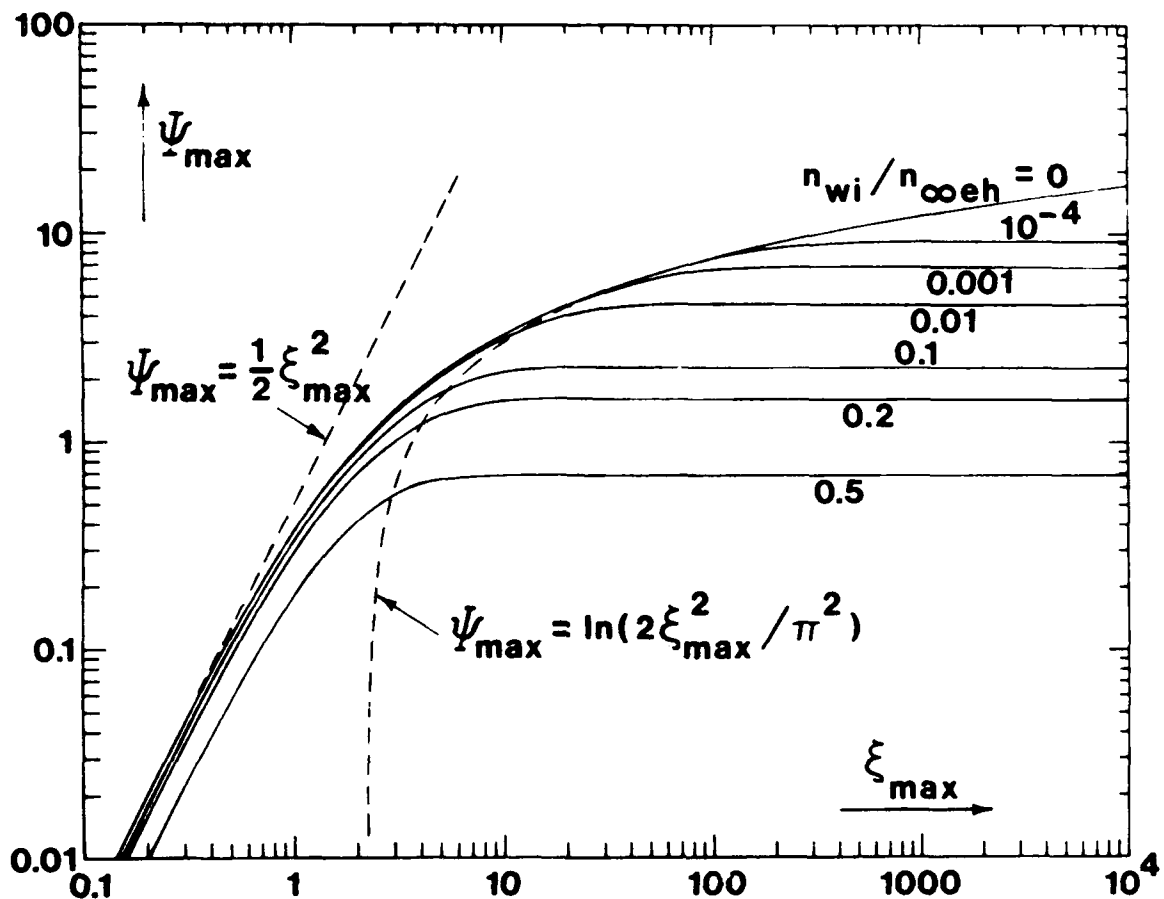


Figure 4.3. Normalized wake potential well depth $\Psi_{\max} = -e\phi_{\max}/kT_{eh}$ vs normalized wake half-width $\xi_{\max} = y_{\max}/\lambda_{Deh}$, as given by Eq. (4.9) for normalized wake ion density $n_{wi}/n_{\infty eh}$ equal to zero, and by numerical solutions of Eq. (4.13) for nonzero values of this quantity. Dotted curves show limiting forms of Eq. (4.9) given by Eqs. (4.10) and (4.11).

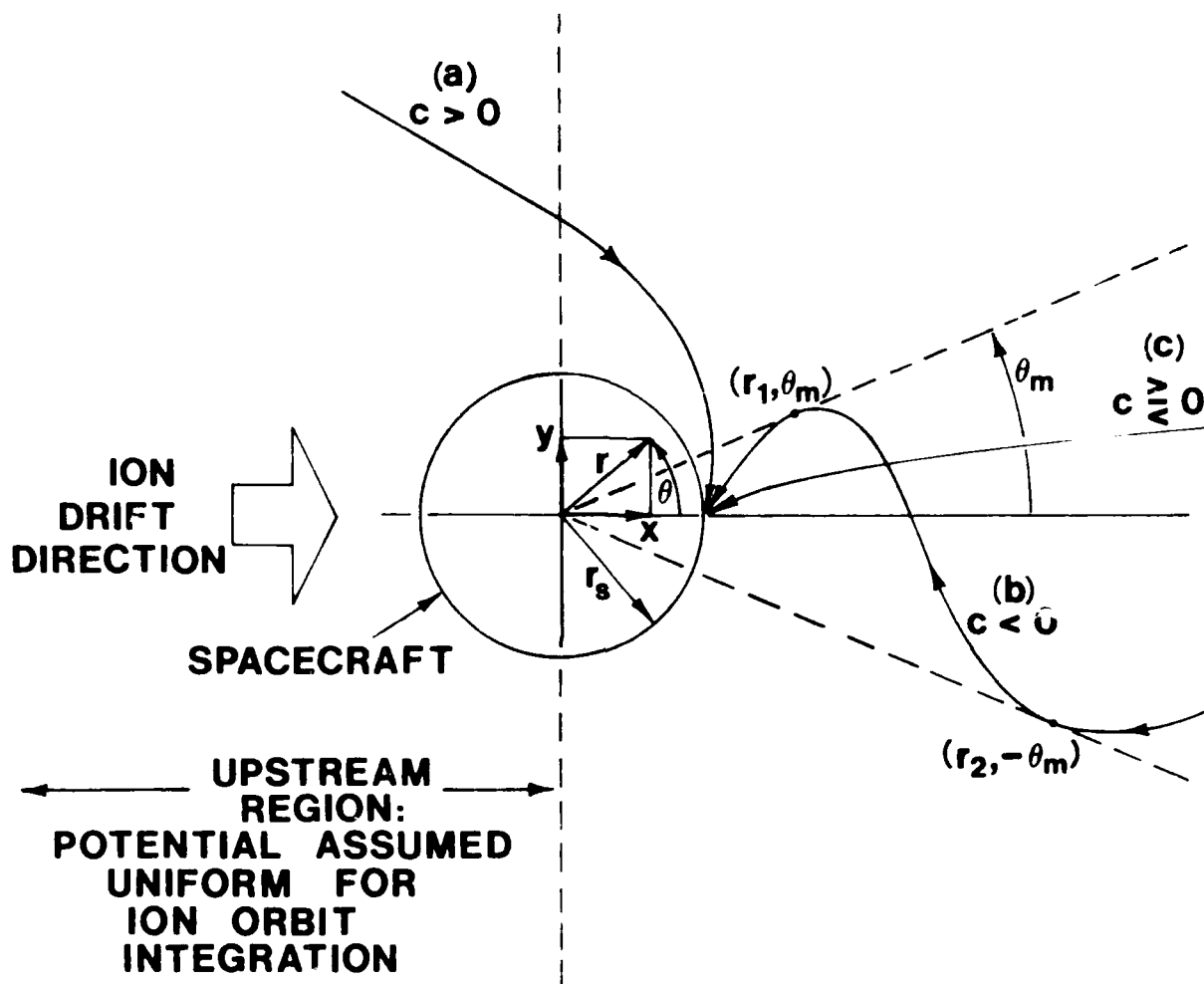


Figure 4.4. General appearance of three types of ion orbits impacting the downstream point ($r = r_s$, $\theta = 0$) in the presence of an assumed wake potential distribution given by Eqs. (4.18) and (4.19).

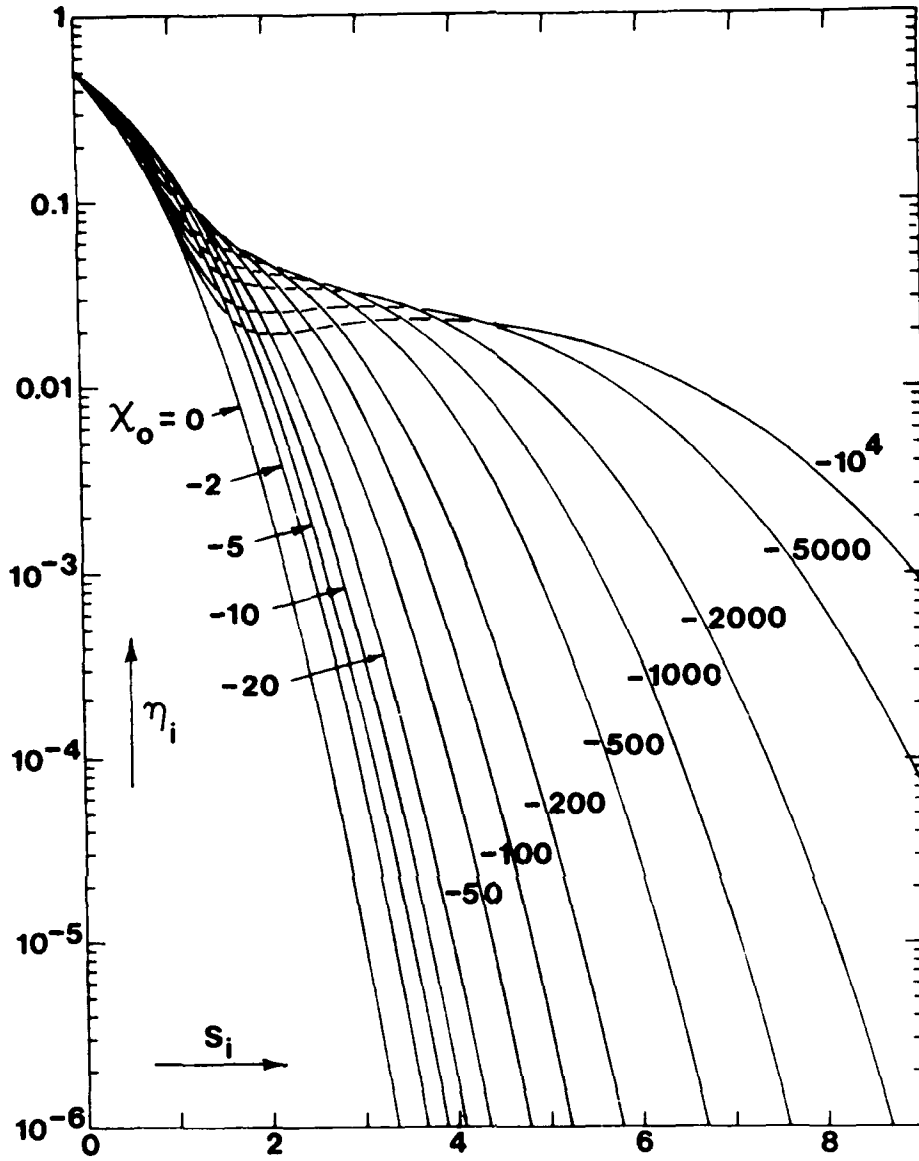


Figure 4.5. Normalized ion density $\eta_i = n_i/n_{i\infty}$ at the downstream surface point ($r = r_s$, $\theta = 0$) in the presence of the potential distribution given by Eqs. (4.18) and (4.19), as a function of the ion speed ratio $S_i = U/(2kT_i/m_i)^{1/2}$, for various values of the normalized downstream-point surface potential $\chi_o = e\phi_o/kT_i$. Values of η_i for $\chi_o = 0$ are given by Eq. (4.17). For $\chi_o < 0$, values of η_i are given by Eq. (C17) with \tilde{f} evaluated as described in Appendix C and using the computer program listed in Appendix D.

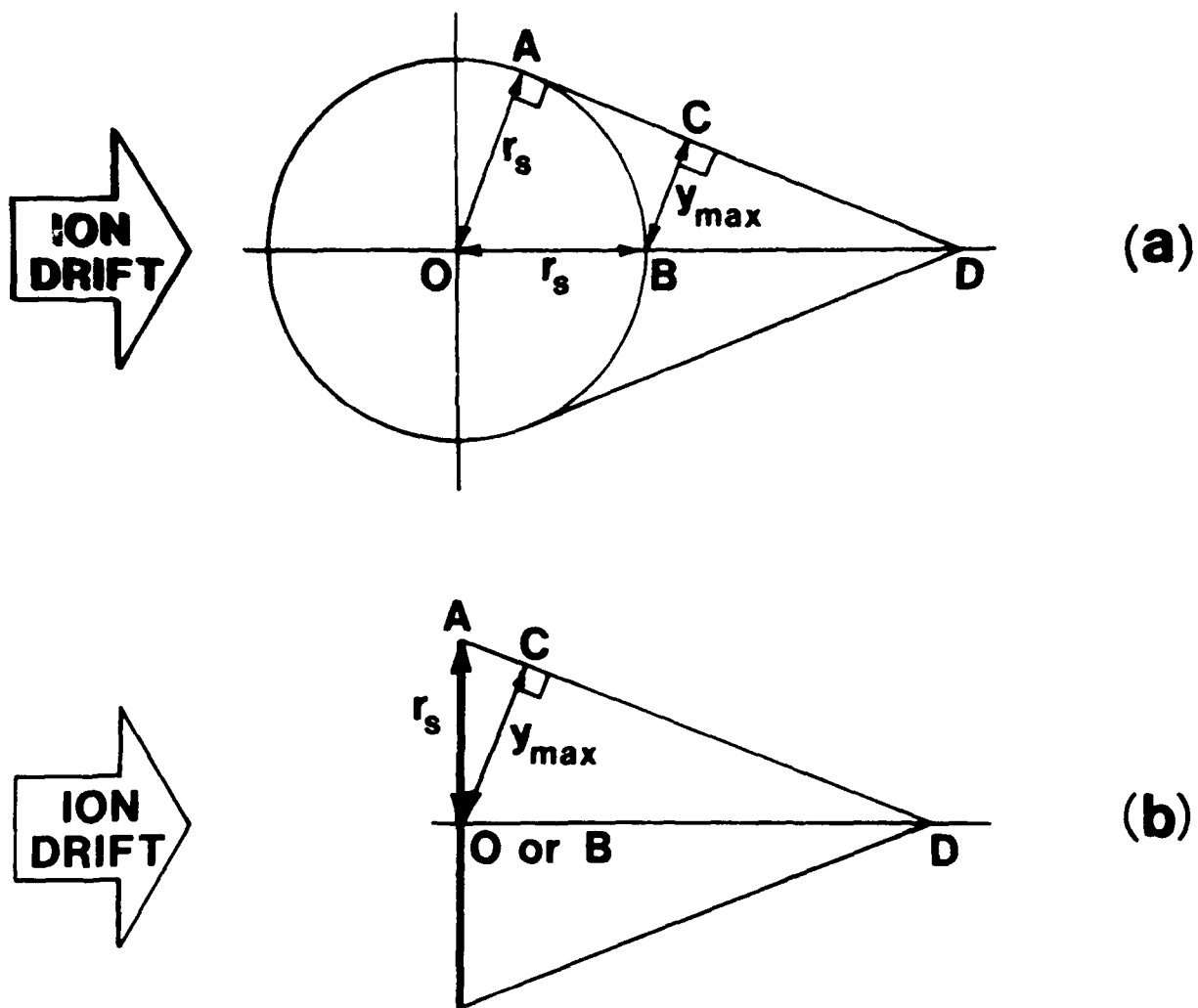


Figure 4.6. Geometry for "improved" calculation of wake half-width, for: (a) cylinder or sphere (b) thin disk or plate normal to ion drift.

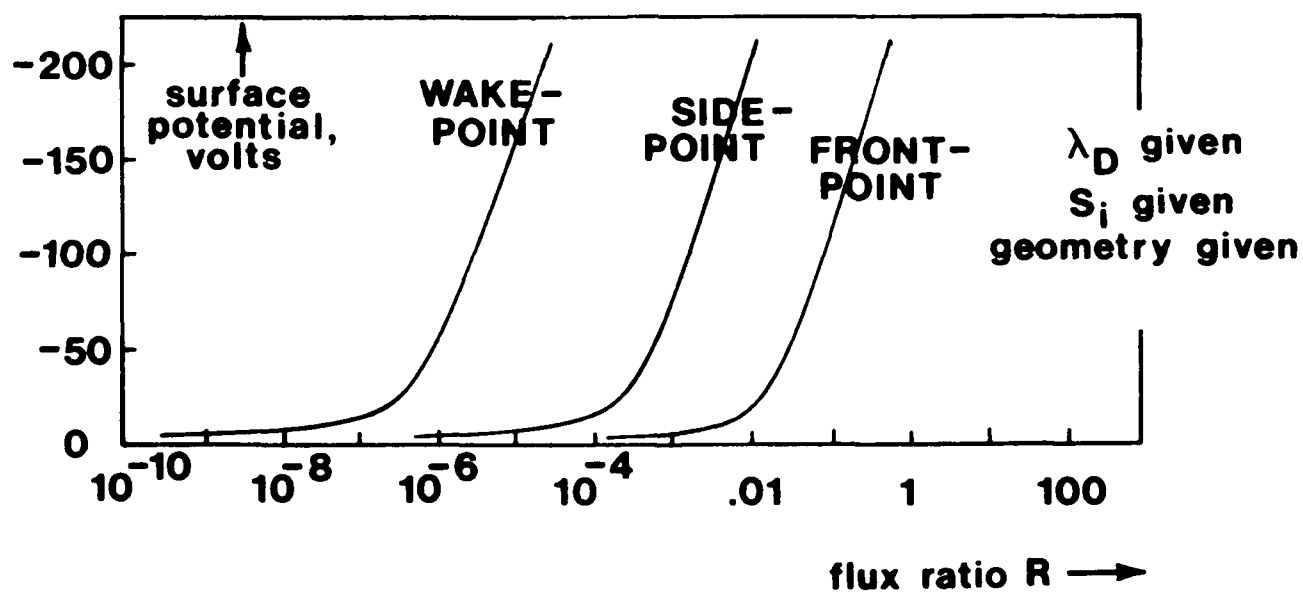


Figure 5.1. Expected general appearance of graphs of spacecraft surface potential as functions of ambient hot electron to total ion flux ratio R .

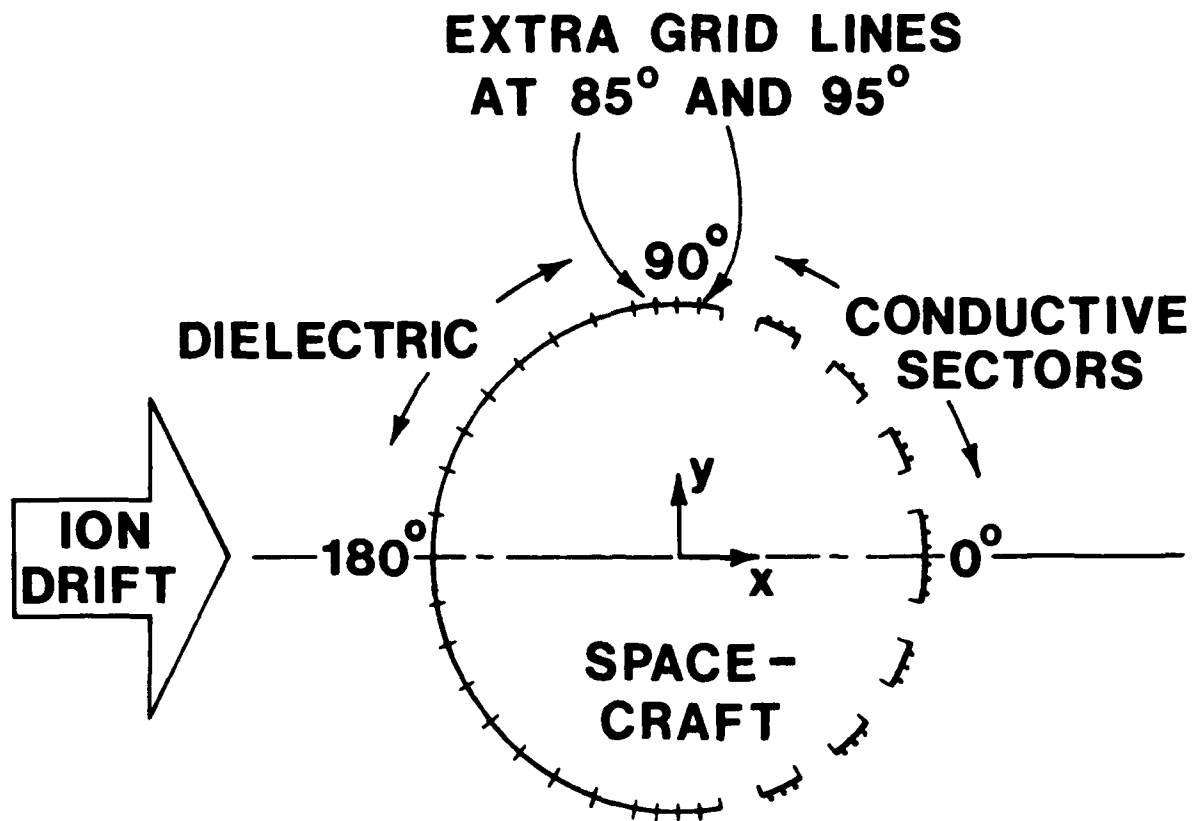


Figure 5.2. Geometry of simulated spacecraft used for computational purposes. The outer boundary of the computational domain is a square whose sides are at $x = \pm 5r_s$, $y = \pm 5r_s$, where r_s is the spacecraft radius. The domain is covered by the finite-element grid shown in Fig. 5.3. Within the gaps between the conductive sectors, the potential is assumed to vary linearly with surface position on the cylinder. The dots on the conductive sectors indicate locations on them where ion currents are calculated.

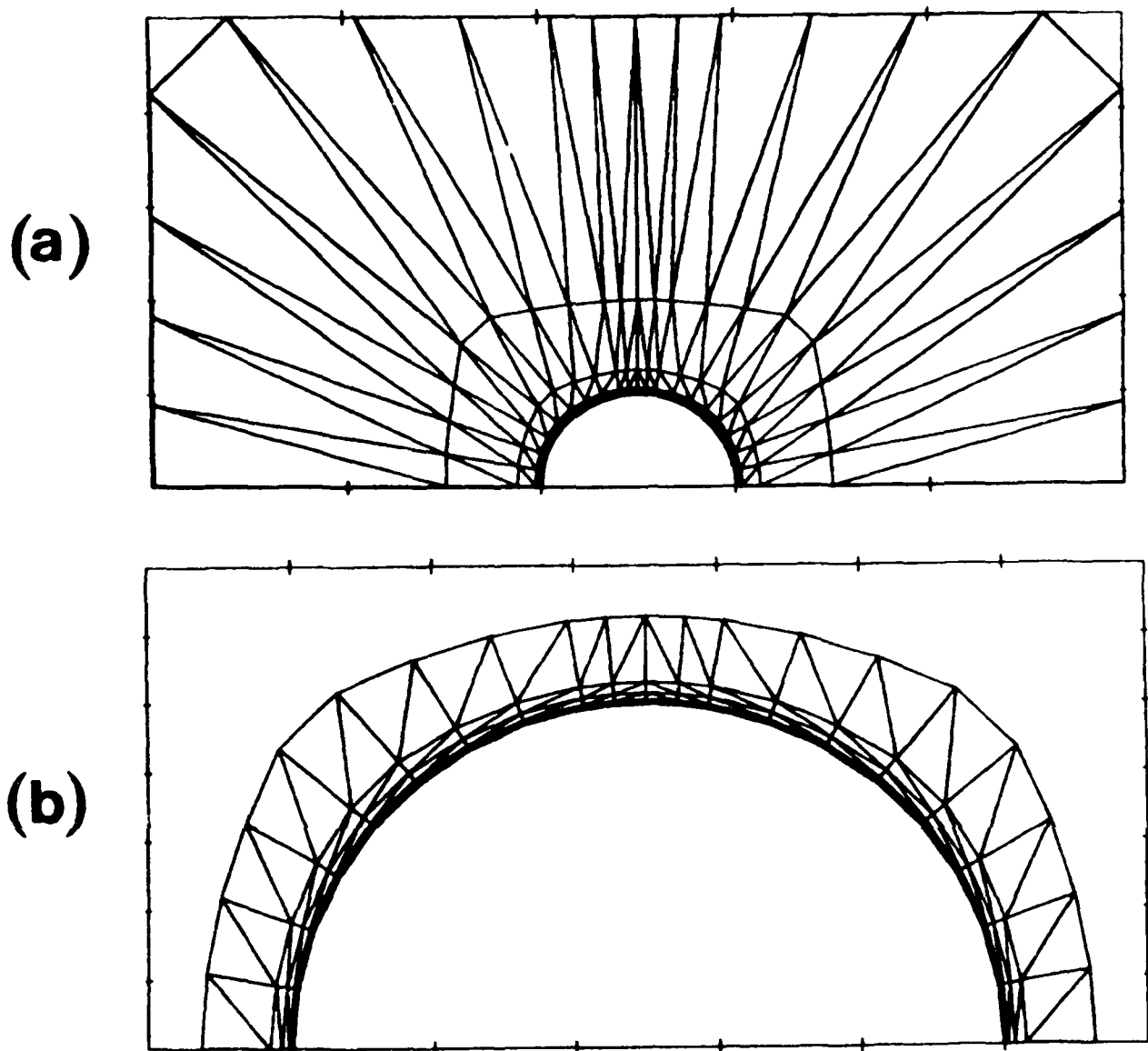


Figure 5.3. (a) Upper half of finite-element grid used for computations. The circular cross-section of the simulated spacecraft is at the center of the grid. Angular intervals in the grid are 10° except for $80^\circ \leq \theta \leq 100^\circ$, where they are 5° . The radial intervals along the 0° , 90° , and 180° rays are, in order of increasing radial distance: 0.0004, 0.0016, 0.0020, 0.0040, 0.0080, 0.0160, 0.0320, 0.1920, 0.7440, and 3.0. The seven radial intervals nearest to the spacecraft surface are unresolved in (a).

(b) Innermost portion of grid shown in (a). The first through fifth radial intervals nearest to the spacecraft surface are still unresolved in (b).

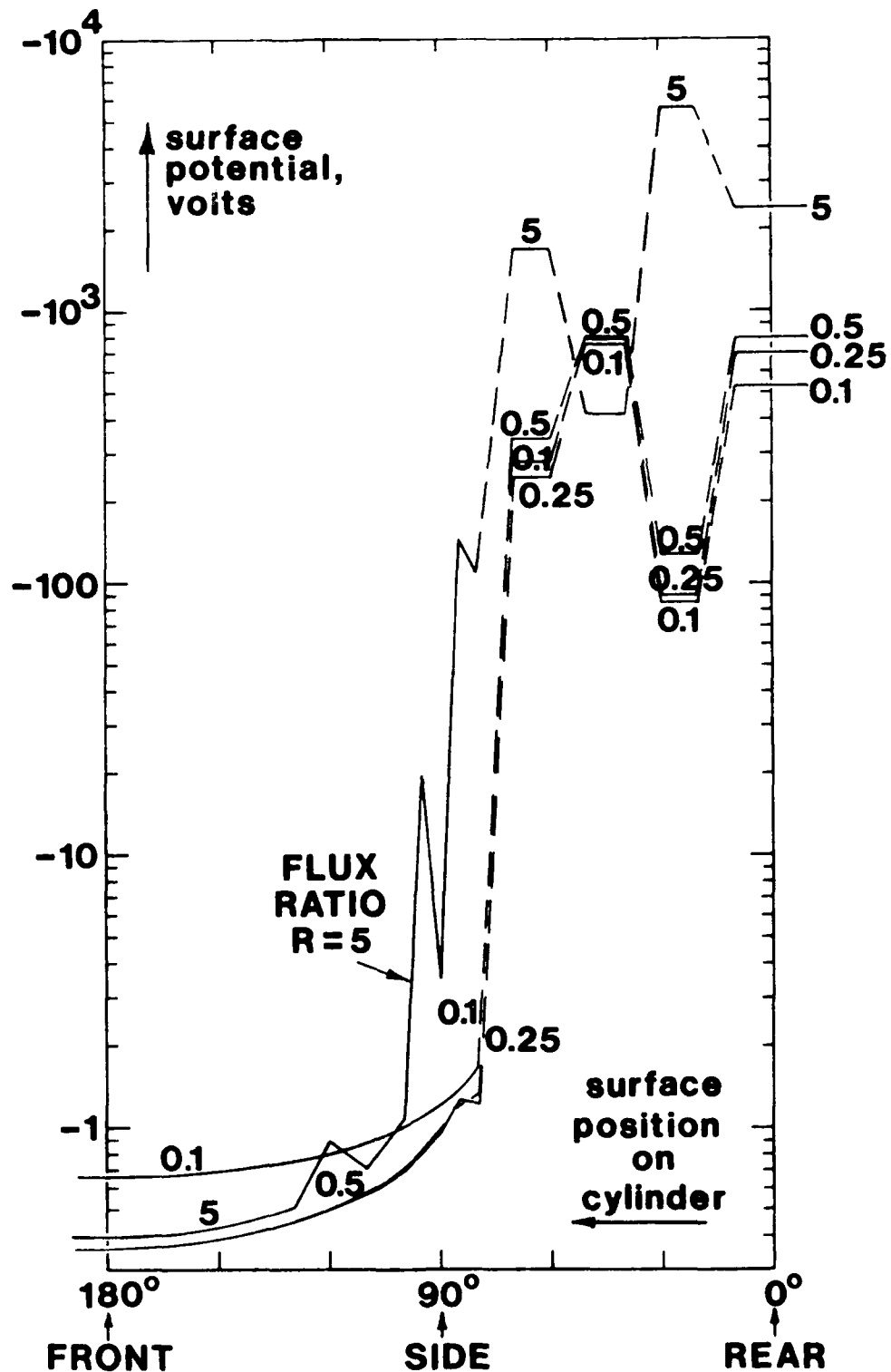


Figure 5.4. Surface potentials as functions of position for the spacecraft geometry shown in Fig. 5.2, for ratios R of hot electron to total ion ambient flux as shown.

APPENDIX C: DETAILS OF MODEL CALCULATION OF DOWNSTREAM-POINT ION DENSITY DESCRIBED IN SECTION 4.3

Equation (4.20) implies that:

$$v_{\theta} = \pm \frac{1}{mr} \{2[C - mq g(\theta)]\}^{\frac{1}{2}} \quad (C1)$$

We substitute this into the equation of conservation of total ion energy E:

$$E = \frac{1}{2} mv^2 + q\phi(r, \theta) = \frac{1}{2} m(v_r^2 + v_{\theta}^2) + q g(\theta)/r^2 \quad (C2)$$

to obtain:

$$v_r = \pm \left[\frac{2}{m} \left(E - \frac{C}{mr^2} \right) \right]^{\frac{1}{2}} \quad (C3)$$

We introduce dimensionless variables as follows:

$$\begin{aligned} l &= L / \left[(2mkT_i)^{\frac{1}{2}} r_s \right]; \quad c = C / [mkT_i r_s^2] \\ u &= v(m/2kT_i)^{\frac{1}{2}}; \quad \epsilon = E/kT_i; \quad \chi = q\phi/kT_i \\ \tilde{g} &= q g(\theta)/(kT_i r_s^2); \quad \tilde{r} = r/r_s \\ \hat{f} &= (\hat{f}/n_{\infty})(2kT_i/m) \end{aligned} \quad (C4)$$

where $\hat{f} \equiv \hat{f}(v_x, v_y)$ is the two-dimensional velocity distribution function given by:

$$\hat{f} = d^2n/dv_x dv_y = \int_{-\infty}^{\infty} f dv_z \quad (C5)$$

Equations (C1) and (C3) then become:

$$u_r = \pm (\epsilon - c/\tilde{r}^2)^{1/2} ; u_\theta = \pm [c - \tilde{g}(\theta)]^{1/2}/\tilde{r} \quad (C6)$$

The relation $r d\theta/dr = v_\theta/v_r$ then leads to:

$$\pm \int_0^\theta \frac{d\theta'}{[c - \tilde{g}(\theta')]^{1/2}} = \int_1^{\tilde{r}} \frac{d\tilde{r}'}{[\tilde{r}'(\epsilon \tilde{r}'^2 - c)]^{1/2}} \quad (C7)$$

With $g(\theta)$ given by Eq. (4.19), both of these integrals can be evaluated analytically in closed form. Equations (4.19), (C4), and (C6) imply that:

$$\begin{aligned} \tilde{g}(\theta) &= \chi_0 (1 - 4\theta^2/\pi^2) < 0 \text{ for } |\theta| < \pi/2 \\ c &= u_{\theta 0}^2 + \chi_0 \\ \epsilon &= u_0^2 + \chi_0 = u_{r0}^2 + c \geq c \end{aligned} \quad (C8)$$

From conservation of energy, we also have $\epsilon = u_\infty^2$, where u_∞ is the dimensionless ion speed at infinite radius, and therefore $\epsilon > 0$ since all ions come from this radius. Since $\tilde{r} \geq 1$, Eq. (C6a) then indicates that $|u_r|$ is an increasing function of r , so no turning-points of radial motion can occur outside the spacecraft, for those ions which reach the downstream point $(\tilde{r}, \theta) = (1, 0)$. However, in the downstream region, $\tilde{g}(\theta)$ increases from $\chi_0 < 0$ to 0 as $|\theta|$ increases from 0 to $\pi/2$ (Eq. C8).

Therefore, if $c < 0$, u_θ as given by Eq. (C6b) will become imaginary before $|\theta|$ reaches $\pi/2$. In this case, there will exist turning-points of circumferential motion, at angular positions $\theta = \pm \theta_m$ (Fig. 4.4) given by $c - \tilde{g}(\theta_m) = 0$, i.e.:

$$\theta_m = \frac{1}{2} \pi u_{\theta 0} / \sqrt{-\chi_0} \quad (C9)$$

A reversed ion orbit having $c < 0$ may or may not reach such a turning-point before reaching infinite radius. Figure 4.4 shows typical ion orbits for $c > 0$ and $c < 0$. A numerical example of ion orbits having angular turning-points, in the neighborhood of a circular disk probe coplanar with a spacecraft surface, has been given by Parker and Whipple (1970, Fig. 5). Far from the spacecraft, we assume that the ion velocity distribution is a drifting Maxwellian given by:

$$\begin{aligned} \tilde{f} &= (1/\pi) \exp [-(\mathbf{u} - \mathbf{S}_i)^2] \\ &= (1/\pi) \exp (-u_x^2 - u_y^2 + 2u_x S_{i1} - S_{i1}^2) \\ &= (1/\pi) \exp (-\epsilon + 2u_x S_{i1} - S_{i1}^2) \end{aligned} \quad (C10)$$

Liouville's theorem for one particle implies that \tilde{f} is constant along each collisionless ion orbit (Bernstein and Rabinowitz, 1959), so we can use (C10) to find \tilde{f} for any such orbit, specified by given values of the impact velocity components u_{r0} and $u_{\theta 0}$ at the downstream axial surface point, if we can find the corresponding values of u_x and u_y far from the spacecraft. For each orbit, (C8)

can be used to find ϵ and c . For an ion orbit having $c > 0$, \tilde{r} can be found by first using the integrated form of (C7) to find the radius \tilde{r} at which the orbit intersects the line $\theta = \pi/2$ (the y-axis), then using (C6b) to find $u_x = -u_\theta$, then substituting this into (C10). For $c < 0$, the procedure is more complicated.

For both $c < 0$ and $c > 0$, we define:

$$\begin{aligned} G(\theta) &= \int_0^\theta d\theta' / [c - \tilde{g}(\theta')]^{\frac{1}{2}} \\ &= \int_0^\theta d\theta' / [u_{\theta_0}^2 + 4\chi_0 \theta'^2 / \pi^2]^{\frac{1}{2}} \\ &= \frac{\pi}{2\sqrt{-\chi_0}} \sin^{-1} \left[\frac{2\sqrt{-\chi_0} \theta}{\pi u_{\theta_0}} \right] \end{aligned} \quad (C11)$$

for $|\theta| \leq$ the lesser of θ_m or $\pi/2$. We also define:

$$H(\tilde{r}) = \int_1^{\tilde{r}} d\tilde{r}' / [\tilde{r}'(\epsilon \tilde{r}'^2 - c)^{\frac{1}{2}}]$$

For $c > 0$, we obtain:

$$H(\tilde{r}) = (1/\sqrt{c}) \left[\sin^{-1} \sqrt{c/\epsilon} - \sin^{-1} \sqrt{c/(\epsilon \tilde{r}^2)} \right] \quad (C12)$$

and for $c < 0$:

$$H(\tilde{r}) = \frac{1}{\sqrt{-c}} \ln \left(\frac{\sqrt{\epsilon - c} + \sqrt{-c}}{\sqrt{\epsilon - c/\tilde{r}^2} + \sqrt{-c/\tilde{r}^2}} \right) \quad (C13)$$

For $c < 0$, the procedure for finding \tilde{f} is now as follows. We first calculate \tilde{r}_1 , the normalized radius of the first angular turning-point on the reversed ion orbit (Fig.4.4). To do this, we equate $H(\tilde{r}_1)$, from Eq. (C13), to $G(\theta_m) = \pi^2/(4\sqrt{-\chi_0})$, from Eq. (C11), and solve for \tilde{r}_1 . We next divide $H(\infty) - H(\tilde{r}_1)$ by $G(\theta_m) - G(-\theta_m) = \pi^2/(2\sqrt{-\chi_0})$. The integral part of this quotient is the number K of complete continuous traverses by the ion orbit between $-\theta_m$ and θ_m in either direction. If K is even, the last angular turning point is at θ_m . If K is odd, it is at $-\theta_m$. In either case, we next calculate $H(\tilde{r}_{k+1}) = H(\tilde{r}_1) + 2KG(\theta_m)$. If K is even, the "final" direction θ_f , at infinity, of the reversed ion orbit is now given by $G(\theta_m) - G(\theta_f) = H(\infty) - H(\tilde{r}_{k+1})$. If K is odd, θ_f is given by $G(\theta_f) - G(-\theta_m) = H(\infty) - H(\tilde{r}_{k+1})$. Solving yields:

$$\theta_f = \pm \frac{\pi u \theta_0}{2\sqrt{-\chi_0}} \cos \left(\frac{2P}{\pi\sqrt{-\chi_0}} \right) \quad (C14)$$

for K even or odd, respectively, where:

$$P = \frac{1}{\sqrt{-c}} \ln (\sqrt{1-c/\epsilon} + \sqrt{-c/\epsilon}) - H(\tilde{r}_{k+1}) \quad (C15)$$

We then have, at infinite radius:

$$\begin{aligned} u_r &= -\sqrt{\epsilon} \\ u_x &= u_r \cos \theta_f \\ u_y &= u_r \sin \theta_f \end{aligned} \tag{C16}$$

for substitution into Eq. (C10).

In terms of the velocity-space polar coordinates $u_o = (u_{ro}^2 + u_{\theta o}^2)^{1/2}$, $\alpha = \tan^{-1} (u_{\theta o}/u_{ro})$, and making use of the symmetry of \tilde{f} with respect to α , the ion number density at the downstream axial surface point is now given by:

$$\begin{aligned} \eta_i \equiv n_i/n_{i\infty} &= 2 \int_{(-\chi_o)^{1/2}}^{\infty} u_o du_o \int_0^{\pi/2} \tilde{f}(u_o, \alpha, \chi_o, S_i) d\alpha \\ &\equiv \eta_i(\chi_o, S_i) \end{aligned} \tag{C17}$$

and, with \tilde{f} evaluated as described in Eqs. (C1) - (C16), this gives an "improved" approximation [compared with Eq. (4.17)] for values of n_{wi} to be substituted into Eq. (4.13) or (4.14). The absence of turning-points of ion radial motion for $\epsilon > 0$, which we noted following Eq. (C8), implies that all of the ion orbits involved in the integration of (C17) "connect back to infinity" and none of them have originated elsewhere on the spacecraft. Although a general proof appears difficult to formulate, this probably means that Eq. (C17) overestimates η_i at

$(\tilde{r}, \theta) = (1, 0)$, whereas Eq. (4.17) underestimates it. In the applications treated in Sec. 4.4, the spacecraft geometry is closer to that of Fig. 4.6b than Fig. 4.6a, and this probably implies an even smaller ion density near surfaces in the central wake region.

We have evaluated (C17) numerically using standard methods. The resulting values of η_i appear in Fig. 4.5. These values have been computed to a relative numerical accuracy of about 0.003 or better. The computer program used for doing this is listed in Appendix D.